

Study on O₂ band Cloud Top Pressure retrieval with METimage

Final report

by

HYGEOS



Laboratoire d'Optique
Atmosphérique, Université de
Lille/Sciences et technologies



for

EUMETSAT



EUMETSAT REFERENCE : EUM/CO/14/4600001448/PDW

THIS PAGE IS INTENTIONALLY LEFT BLANK

Project Team

Philippe Dubuisson LOA
 Jérôme Riedi LOA
 Laurent Labonnote LOA
 Nicolas Ferlay LOA
 Didier Ramon HYGEOS
 Mathieu Compiègne HYGEOS

Document change record

Version	Date	Reasons for evolution
0.1	18/05/2015	Initial version for Phase I
0.5	01/06/2015	Account for comments/corrections after the Mid-Term meeting for Phase I
0.9	20/10/2015	Start modifications after Phase II
1.0	15/12/2015	Final modifications following Final Review

Document Distribution

Philip Watts EUMETSAT
 Loredana Spezzi EUMETSAT
 Philippe Dubuisson LOA
 Jérôme Riedi LOA
 Laurent Labonnote LOA
 Nicolas Ferlay LOA
 Didier Ramon HYGEOS
 Mathieu Compiègne HYGEOS

Document Editor

Mathieu Compiègne HYGEOS

Visa:

Document Reference

HYGEOS/METimCTP/FR

Table of Contents

1 PURPOSE AND SCOPE OF THE STUDY.....	13
2 LITERATURE SURVEY ON RETRIEVAL METHODS.....	15
2.1 Theoretical studies on O ₂ CTP retrieval.....	16
2.2 PARASOL/POLDER CTP retrieval.....	19
2.2.1 Operational retrieval algorithm.....	19
2.2.2 Improved algorithm.....	20
2.3 MERIS CTP retrieval.....	22
2.3.1 Operational retrieval algorithm.....	22
2.3.2 Other MERIS based CTP algorithm.....	24
2.4 Other missions.....	25
2.5 Conclusion regarding the METimage algorithm.....	26
3 RADIATIVE TRANSFER MODEL CANDIDATES.....	27
3.1 MOMO.....	28
3.2 SCIATRAN.....	28
3.3 LibRadtran.....	28
3.4 ARTDECO (including GAME).....	28
4 SENSITIVITY STUDY.....	32
4.1 General approach.....	32
4.2 Sensitivity of the signal ratio and impact on CTP retrieval.....	35
4.2.1 Instrument noise.....	35
4.2.2 Cloud optical thickness.....	36
4.2.3 Cloud geometrical thickness.....	37
4.2.4 Cloud vertical profile.....	38
4.2.5 Ice particle model.....	39
4.2.6 Particle effective radius.....	40
4.2.7 Presence of aerosols.....	41
4.2.7.a Continental average.....	41
4.2.7.b Maritime clean.....	42
4.2.8 Surface pressure.....	43
4.2.9 ISRF wings.....	44
4.2.10 Surface directionality.....	45
4.2.10.a Water surface.....	47
4.2.10.b Land surface.....	48
4.3 Sensitivity of window channel reflectance and impact on the COT and CTP retrieval.....	49
4.3.1 Ozone.....	50
4.3.2 Ice particle model.....	51
4.3.3 Effective radius.....	52
4.3.4 Aerosols.....	53
4.3.4.a Continental average.....	53
4.3.4.b Maritime clean.....	54
4.3.5 Surface directionality.....	55
4.3.5.a Water surface.....	56
4.3.5.b Land surface.....	57
4.4 Conclusion on sensitivity study.....	57
5 DAY 1 ALGORITHM AND LOOK-UP TABLES.....	59
5.1 General description.....	59
5.2 Specifics about the CTP-Psurf space in LUT.....	61
5.3 Specifics about optimal estimate.....	61
5.4 Input level 1b data and ancillary data.....	63
5.5 Output data.....	63

5.6 LUT built in the present study.....	64
5.7 Algorithm implementation for the present study.....	66
6 DAY-1 ALGORITHM TESTING.....	69
6.1 4MSDS synthetic data.....	69
6.1.1 Data description.....	69
6.1.2 LUT sampling/interpolation errors.....	72
6.1.2.a High resolution LUTs.....	72
6.1.2.b Medium resolution LUTs.....	75
6.1.3 COT, CTP retrieval.....	76
6.1.3.a High resolution LUTs.....	77
6.1.3.b High resolution LUTs with noisy and biased data.....	80
6.1.3.c Medium resolution LUTs.....	82
6.1.3.d Medium resolution with climatological cloud vertical structure LUTs.....	83
6.2 MERIS data.....	85
6.2.1 Data description.....	85
6.2.2 Results for OE COT, CTP retrievals.....	88
7 CONCLUSION AND PERSPECTIVES.....	99
7.1 Summary/conclusion on the present study.....	99
7.2 Caveats and short term possible evolutions.....	100
7.3 Further evolution of the algorithm and LUTs.....	101
8 ANNEX.....	103
8.1 Sensitivity normalized by instrument noise.....	103
8.1.1 Sensitivity of the signal ratio.....	103
8.1.2 Sensitivity of window channel reflectance.....	107
8.2 References.....	110

List of figures

Figure 2.1: (Left) Schematic representation of the variety of possible photon path in cloudy atmosphere. (Right) AFGL Tropical atmosphere transmittance spectrum around A-band O₂ band for an airmass of 1. METimage filters VII-4 and VII-5 are over-plotted in blue and red respectively. The ISRF are modelled as a rectangle function on the present graph.....15

Figure 2.1.1 Effective single_layer clout top pressure, depending on distribution of optical thickness for two layered cloud with combined optical thickness of 50. The lower layer top is at 750hPa while the upper layer top is at 230hPa. Note: curves are identical for surface albedo of 0.1 and 0.6. Source: Preusker and Lindstrot [2009].....16

Figure 2.1.2 (left) Temperature profiles [McClatchey et al. 1972], (middle) relative change of MERIS 11/10 channel (see figure 2.3.1) ratio depending on cloud height and temperature profile as compared with a U.S. standard profile, and (right) equivalent change in hPa. Source: Preusker and Lindstrot [2009].....17

Figure 2.2.1: (Left) Atmospheric transmission around the O₂ A-band together with the two POLDER channels at 763 and 765 nm. (Right) Principal of multi-view angle observation. The wide angle camera allows one to take successive pictures of the same target with different view geometries as the platform goes on its orbit.....19

Figure 2.2.2: (Left) Equivalent vertical penetration $\langle Z \rangle$ within cloud layers of various optical and geometrical thickness for the case of liquid clouds with overhead sun at zenith. Cloud base is fixed at 1-km altitude. The definition of $\langle Z \rangle$ and the asymptotic expression derived from van de Hulst [1980] are over-plotted as a reference. (Right) Variation of retrieved PO₂ with the viewing zenith angles θ_v in the solar plane (φ is the measurement's relative azimuth) for simulated TOA radiance. Characteristics of the case study are indicated in the title. Horizontal lines indicate the level of cloud top, middle, and base pressures (denoted respectively by CTP, CMP, and CBP). The angularly averaged PO₂ is 667hPa and σ_{PO_2} is 11hPa. Discontinuities of the directional cloud oxygen pressure at -60° and -20° are signatures of cloud scattering phase function.....21

Figure 2.3.1: MERIS channel 10 (red) and 11 (blue) transmission overplotted on atmospheric oxygen transmission. source: Lindstrot [2009].....22

Figure 2.3.2: Average cloud vertical extinction profiles for nine cloud types (solid line) and standard deviation from the mean (dotted line), as well as standard deviation of the CTP (error bar on top). Source: Carbajal Henken et al. [2014].....24

Figure 3.4.1: Transmission as computed with ARTDECO for US62 atmosphere with GAME and Kato et al. [1999] k-distribution binning. Note that for Kato, the bins width is representative while the bin range limits are not strictly reproduced on the plot.....30

Figure 4.1.1: Modelled ISRF shape for the VII-5 channel. FWHM = 10 nm.....32

Figure 4.1.2: Error on VII-5 channel gas transmission obtained for a correlated k-distribution for various numbers of k-interval and various airmass. The error is obtained by comparison to the line-by-line computation.....33

Figure 4.1.3: METimage 763/752 nm reflectance ratio as a function of the optical thickness and CTP for ice (right) and liquid clouds (left). Computation are done for a Lambertian surface of albedo 0.0 (higher panels), 0.1 (middle panels) and 0.6 (lower panels). The sun zenith angle is 30° and the observation is at nadir.....34

Figure 4.2.1 (Left) Variation of the 763/752 nm reflectance ratio corresponding to expected METimage noise level. (Right) Equivalent variation of CTP.....35

Figure 4.2.2 (Left) Variation of the 763/752 nm reflectance ratio due to a change of COT by $\pm 10\%$. (Right) Equivalent variation of CTP.....36

Figure 4.2.3 (Left) Variation of the 763/752 nm reflectance ratio due to a change of the CGT by $\pm 10\%$. (Right) Equivalent variation of CTP.....37

Figure 4.2.4 (Left) Variation of the 763/752 nm reflectance ratio due a change between a CPR profile (Cirrostratus and Stratocumulus) to a homogeneous profile. (Right) Equivalent variation of CTP.....38

Figure 4.2.5 Phase function for General Habit Mixture model from Baum et al. [2014] and Rough Hexagonal Mono-crystal (POLDER/PARASOL like model). The effective radius is 25 microns.....39

Figure 4.2.6 (Left) Variation of the 763/752 nm reflectance ratio due a change of ice particle model (see

figure 4.2.5).(Right) Equivalent variation of CTP.....39

Figure 4.2.7 (Left) Variation of the 763/752 nm reflectance ratio due a change of particle effective radius between 5 and 30 (60) microns for Liquid (ice) cloud.(Right) Equivalent variation of CTP. White areas are produced where CTP corresponding to a given R is out of the modelled domain.....40

Figure 4.2.8 (Left) Variation of the 763/752 nm reflectance ratio due to the presence of a continental average aerosol (H=8km, $\tau=0.1$). (Right) Equivalent variation of CTP.....41

Figure 4.2.9 (Left) Variation of the 763/752 nm reflectance ratio due to the presence of a maritime clean aerosol (H=1km, $\tau=0.1$).(Right) Equivalent variation of CTP.....42

Figure 4.2.10 (Left) Variation of the 763/752 nm reflectance ratio due to a change of $\pm 10\%$ of the surface pressure (Right) Equivalent variation of CTP. The value $>200\text{hPa}$ are out of the domain (white areas).....43

Figure 4.2.11 (Left) Variation of the 763/752 nm reflectance ratio due to a variation of energy in the 763 nm ISRF wings from 1% to 5%. (Right) Equivalent variation of CTP.....44

Figure 4.2.12: (left) 865nm reflectance at TOA for the ocean with various wind speed as a function of the view zenith angle in the solar plane. (right) 670 nm reflectance at TOA for various land surface type model with a Li-Ross model with hot-spot following the parametrisation of Bacour and Bréon [2005]. k_0 is set to 0.1. For both the land and ocean cases, the sun zenith angle is 30.0o.....46

Figure 4.2.13 (Left) Variation of the 763/752 nm reflectance ratio over the ocean due to a variation of the wind speed of $\pm 10\%$ regarding 5m/s. (Right) Equivalent variation of CTP. The sun zenith angle is 30o. The observation is done in the principal plane.....47

Figure 4.2.14 (Left) Variation of the 763/752 nm reflectance ratio due to changing from a desert BRDF to a broad-leaf forest BRDF. (Right) Equivalent variation of CTP. The sun zenith angle is 30o. The observation is done in the principal plane.....48

Figure 4.3.1 670 nm reflectance for a ice cloud (left) and liquid cloud (right) over a Lambertian surface with an albedo of 0.1.....49

Figure 4.3.2 (Upper left) Relative variation of reflectance due to a variation of the Ozone column by $\pm 10\%$. (lower left) Equivalent relative variation of COT. (Right) Propagation of the COT variability to equivalent CTP variation.....50

Figure 4.3.3 (Upper left) Relative variation of reflectance due a change of ice particle model (see figure 4.2.5) (lower left) Equivalent relative variation of COT. (Right) Propagation of the COT variability to equivalent CTP variation.....51

Figure 4.3.4 (Upper left) Relative variation of reflectance due to a change of particle effective radius between 5 and 30 (60) microns for Liquid (ice) cloud. (lower left) Equivalent relative variation of COT. (Right) Propagation of the COT variability to equivalent CTP variation.....52

Figure 4.3.5 (Upper left) Relative variation of reflectance due to the presence of a continental average aerosol (H=8km, $\tau=0.1$). (lower left) Equivalent relative variation of COT. (Right) Propagation of the COT variability to equivalent CTP variation.....53

Figure 4.3.6 (Upper left) Relative variation of reflectance due to the presence of a maritime clean aerosol (H=1km, $\tau=0.1$). (lower left) Equivalent relative variation of COT. (Right) Propagation of the COT variability to equivalent CTP variation.....54

Figure 4.3.7 (left) 865nm reflectance as a function of COT and view zenith angle in the principal plane for a wind speed of 5m/s (right) 670nm reflectance as a function COT and view zenith angle in the principal plane for a needle-leaf forest BRDF. The sun zenith angle is 30o for both cases. The cloud properties are for ice cloud.....55

Figure 4.3.8 (Left) Relative variation of reflectance as a function of COT and view zenith angle in the principal plane due to a variation of the wind speed of $\pm 10\%$ regarding 5m/s. (middle) Equivalent relative variation of COT. (Right) Propagation of the COT variability to equivalent CTP variation. The sun zenith angle is 30o for both cases.....56

Figure 4.3.9 (Left) Relative variation of reflectance as a function of COT and view zenith angle in the principal plane due to change of BRDF from a desert to a broad-leaf forest. (middle) Equivalent relative variation of COT. (Right) Propagation of the COT variability to equivalent CTP variation. The sun zenith angle is 30o for both cases.....57

Figure 5.1.1 Climatology of Cloud Geometrical Thickness (CGT) per class of Cloud Optical Thickness and

varying Cloud Top Pressure (CTP). (Upper left panel) ice cloud over ocean, (Upper right panel) ice cloud over land, (lower left panel) liquid cloud over ocean and (lower right panel) liquid cloud over land. Statistics are obtained from one year of CloudSat/Calipso measurements (product : 2B_GEOPROF_LIDAR, year : 2008, effective of population : 1096505 (liquid clouds) , 586170 (ice clouds)).....60

Figure 5.2.1 Representation of the CTP and Psurf dimensions of LUTs. Red grid represents the LUT sampling. Hatched area shows the space for which no LUT entry can be computed since CTP > Psurf. The green axis shows $R=f(CTP)$ for an interpolated value of Psurf. Filled circles represent computed LUT entries while void circles represent non-physical “ghost” values computed by extrapolation of values defined in the LUT (see the text)..... 61

Figure 6.1.1 Synthetic data set for METimage VII-4 (752 nm) created with ARTDECO RT package as part of the EUMETSAT project “Test Data for the EPS-SG instruments METimage and 3MI”. Both panels represents ~20min data acquisition.....69

Figure 6.1.2 AVHRR (dcomp algorithm) Cloud Optical Thickness used for the SDS.....70

Figure 6.1.3 AVHRR (acha algorithm) CTP used for the SDS.....71

Figure 6.1.4 Maps (upper panels) and histograms (lower panels) of the relative differences (ILUT –Ion-the-fly)/Ion-the-fly (left panel) and (RLUT –Ron-the-fly)/Ron-the-fly (right panel) for the Atlantic scene. ILUT and RLUT were obtained with “high” resolution LUTs (see Table 3).....73

Figure 6.1.5 Maps (upper panels) and histograms (lower panels) of the relative differences (ILUT –Ion-the-fly)/Ion-the-fly (left panel) and (RLUT –Ron-the-fly)/Ron-the-fly (right panel) for the Europe/Africa scene. ILUT and RLUT were obtained with “high” resolution LUTs (see Table 3).....74

Figure 6.1.6 Histograms of the relative differences (ILUT –Ion-the-fly)/Ion-the-fly (left panels) and (RLUT –Ron-the-fly)/Ron-the-fly (right panels) for the Atlantic (upper panel) and Europe/Africa (lower panel) scene. This are obtained by restricting to COT>10. ILUT and RLUT were obtained with “high” resolution LUTs (see Table 3)..... 75

Figure 6.1.7 Histograms of the relative differences (ILUT –Ion-the-fly)/Ion-the-fly (left panels) and (RLUT –Ron-the-fly)/Ron-the-fly (right panels) for the Atlantic (upper panel) and Europe/Africa (lower panel) scenes. ILUT and RLUT were obtained with “medium” resolution LUTs (see Table 3).....76

Figure 6.1.8 Maps (upper panels) and histograms (lower panels) of the relative difference (COTOE –COTAVHRR)/ COTAVHRR (left panel) and absolute difference CTPOE –CTPAVHRR (right panel) for the Atlantic scene. Retrieval was perform using the “high” resolution LUTs (see Table 3).....77

Figure 6.1.9 Maps (upper panels) and histograms (lower panels) of the relative difference (COTOE –COTAVHRR)/ COTAVHRR (left panel) and absolute difference CTPOE –CTPAVHRR (right panel) for the Europe/Africa scene. Retrieval was perform using the “high” resolution LUTs (see Table 3).....78

Figure 6.1.10 Histogram of the error on the OE retrieval COTOE –COTAVHRR (left panel) and CTPOE –CTPAVHRR (right panels) normalized by the OE estimated uncertainties (and) for the Atlantic scene (upper panels) and Europe/Africa scene (lower panel)..... 79

Figure 6.1.11 Histograms of the relative difference (COTOE –COTAVHRR)/ COTAVHRR (left panel) and absolute difference CTPOE –CTPAVHRR (right panel) for the Atlantic scene (upper panels) and Europe/Africa scene (lower panels). Retrieval was perform using the “high” resolution LUTs (see Table 3) on SDS data in which noise and biases were added.....80

Figure 6.1.12 Histograms of the relative difference (COTOE –COTAVHRR)/ COTAVHRR (left panel) and absolute difference CTPOE –CTPAVHRR (right panel) for the Atlantic scene (upper panels) and Europe/Africa scene (lower panels). Retrieval was perform using the “medium” resolution LUTs (see Table 3).....82

Figure 6.1.13 Map of CTPOE –CTPAVHRR and histograms of the relative difference (COTOE –COTAVHRR)/ COTAVHRR and absolute difference CTPOE –CTPAVHRR for the Atlantic scene. Retrieval was perform using the “medium” resolution LUTs (see Table 3) with a climatological cloud vertical structure.....83

Figure 6.2.1 RGB representation for MERIS orbits that were used for testing of the Day-1 algorithm. In order for it to fit the page, these RGB pictures were squeezed in the vertical direction (The original data are ~1100 x 15000 pixels).....87

Figure 6.2.2 Scatter plots and relative difference histograms of OE COT versus MERIS l2 COT product for

the whole August 2003 orbits. Upper panel is for orbit on 24th and lower panel is for the orbit on the 15th..89

Figure 6.2.3 Scatter plots and relative difference histograms of OE COT versus MERIS L2 COT product for the whole February 2003 orbits. Upper panel is for orbit on 15th and lower panel is for the orbit on the 5th.90

Figure 6.2.4 Scatter plots of OE CTP versus MERIS L2 CTP product for the August 2003 orbits. Upper panels is for orbit on 24th and lower panels is for the orbit on the 15th. The left panels are for the all pixels while the right panels are for pixels that match the MERIS-11 channel central wavelengths used in our LUT building (761.875nm) to ± 0.01 nm.....91

Figure 6.2.5 Scatter plots of OE CTP versus MERIS L2 CTP product for the February 2003 orbits. Upper panels is for orbit on 15th and lower panels is for the orbit on the 5th. The left panels are for the all pixels while the right panels are for pixels that match the MERIS-11 channel central wavelengths used in our LUT building (761.875nm) to ± 0.01 nm.....92

Figure 6.2.6 Number of iterations, a posteriori cost function, residual for the reflectance and residual for the signal ratio for pixels of the orbit of February 5th that match the MERIS-11 channel central wavelengths used in our LUT building (761.875nm) to ± 0.01 nm.....93

Figure 6.2.7 COT (upper panels) and CTP (lower panels) maps for Stratocumulus in the Southern Atlantic on the orbit of August 24th. Left panels are for MERIS L2 products and right panels are for OE retrieval. On CTPOE, red dashes at the bottom of the image shows the pixel columns corresponding to wavelengths of our LUT building (761.875nm) to ± 0.01 nm.....94

Figure 6.2.8 COT (upper panels) and CTP (lower panels) maps for a depression in southern Atlantic in the orbit of February 5th. Left panels are for MERIS L2 products and right panels are for OE retrieval. On CTPOE, red dashes at the bottom of the image shows the pixel columns corresponding to wavelengths of our LUT building (761.875nm) to ± 0.01 nm.....95

Figure 6.2.9 COT (upper panels) and CTP (lower panels) maps for stormy conditions over Africa in the orbit of August 24th. Left panels are for MERIS L2 products and right panels are for OE retrieval. On CTPOE, red dashes at the bottom of the image shows the pixel columns corresponding to wavelengths of our LUT building (761.875nm) to ± 0.01 nm.....96

Figure 6.2.10 Land/water mask and CTPOE, for two different scene (part of Aug 24th for left panel and part of Feb 5th for right panel).....97

Figure 8.1.1 Variation of CTP equivalent to a change of COT by $\pm 10\%$ for the ratio 752/763nm normalized by the limit of detection.....103

Figure 8.1.2 Variation of CTP equivalent to a change of CGT by $\pm 10\%$ for the ratio 752/763nm normalized by the limit of detection.....104

Figure 8.1.3 Variation of CTP equivalent to a change between a CPR profile (Cirrostratus and Stratocumulus) to a homogeneous profile for the ratio 752/763nm normalized by the limit of detection.....104

Figure 8.1.4 Variation of CTP equivalent to a change of ice particle model (see figure 4.2.5) for the ratio 752/763nm normalized by the limit of detection.....104

Figure 8.1.5 Variation of CTP equivalent to a change of particle effective radius between 5 and 30 (60) microns for Liquid (ice) cloud for the ratio 752/763nm normalized by the limit of detection.....105

Figure 8.1.6 Variation of CTP equivalent to the presence of a continental average aerosol (H=8km, $\tau=0.1$) for the ratio 752/763nm normalized by the limit of detection.....105

Figure 8.1.7 Variation of CTP equivalent to the presence of a maritime clean aerosol (H=1km, $\tau=0.1$) for the ratio 752/763nm normalized by the limit of detection.....106

Figure 8.1.8 Variation of CTP equivalent to to a change of $\pm 10\%$ of the surface pressure for the ratio 752/763nm normalized by the limit of detection.....106

Figure 8.1.9 Variation of CTP equivalent to a variation of energy in the 763 nm ISRF wings from 1% to 5% for the ratio 752/763nm normalized by the limit of detection.....107

Figure 8.1.10 equivalent todue to a variation of the Ozone column by $\pm 10\%$ normalized by the limit of detection.....107

Figure 8.1.11 equivalent todue to a change of ice particle model (see figure 4.2.5) normalized by the limit of detection.....108

Figure 8.1.12 equivalent todue to a change of particle effective radius between 5 and 30 (60) microns for Liquid (ice) cloud normalized by the limit of detection.....108

Figure 8.1.13 equivalent to the presence of a continental average aerosol (H=8km, $\tau=0.1$) normalized by the limit of detection.....	109
Figure 8.1.14 equivalent to the presence of a maritime clean aerosol (H=1km, $\tau=0.1$) normalized by the limit of detection.....	109

Index of Tables

Table 1: Position, width and primary use for visible and short-wave infrared METimage channels.....	13
Table 2: 670 nm Li-Ross model directional parameters for various biomes as derived by Bacour and Bréon [2005]. Note that k_0 , k_1 , and k_2 , are usually referred to as isotropic, geometric and volumetric terms. The mean k_0 was obtained over the pixels used to derived the parametrization for each biome (several hundreds). It shows the typical level of reflectance expected for a given biome.....	45
Table 3: Characteristics of the LUT sampling. Note: in the LUT building process, k_0 (isotropic BRDF parameter) is actually sampled between 0.0 and 0.45. The WSA is then obtained for each biomes separately.	65

Acronyms

ANN	Artificial Neural Network
BASE	Bidirectional Anisotropy Standard shape
BPDF	Bidirectional Polarized Distribution Function
BRDF	Bidirectional Reflectance Distribution Function
CALIOP	Cloud Aerosol Lidar with Orthogonal Polarization (on board CALIPSO)
CBP	Cloud Bottom Pressure
CGT	Cloud Geometrical Thickness
CMP	Cloud Middle Pressure
COT	Cloud Optical Thickness
CPR	Cloud Profile Radar (on board CloudSat)
CTP	Cloud Top Pressure
DEM	Digital Elevation Model
EPS-SG	EUMETSAT Polar System Second Generation
IGBP	International Geosphere-Biosphere Programme
ISRF	Instrumental Spectral Response Function
I/O	Input / Output
IGBP	International Geosphere Biosphere Programme
LOA	Laboratoire d'Optique Atmosphérique
LUT	Look-Up Table
NWC	Nowcasting
NWP	Numerical Weather Prediction
RTM	Radiative Transfer Model
SDS	Synthetic dataset
SOW	Statement Of Work
SWIR	Short Wave InfraRed
TOA	Top Of Atmosphere
WSA	Wight Sky Albedo

1 PURPOSE AND SCOPE OF THE STUDY

Channel	Position (μm)	FWHM (μm)	Primary use
VII-1	0.443	0.03	Aerosol, ‘true colour imagery’ (blue channel), vegetation
VII-2	0.555	0.02	Clouds, vegetation, ‘true colour imagery’ (green channel)
VII-3	0.670	0.02	Clouds, vegetation, ‘true colour imagery’ (red channel)
VII-4	0.752	0.01	Atmospheric corrections (aerosol), vegetation
VII-5	0.763	0.01	Optical cloud top height assignment
VII-6	0.865	0.02	Vegetation, aerosol, clouds, surface features
VII-7	0.914	0.02	Water vapour imagery, water vapour total column
VII-8	1.240	0.02	Vegetation, aerosol
VII-9	1.375	0.04	High level aerosol, cirrus clouds, water vapour imagery
VII-10	1.630	0.02	Cloud phase, snow, vegetation, aerosol, fire
VII-11	2.250	0.05	Cloud micro-physics at cloud top, vegetation, aerosol over land, fire (effects)

Table 1: Position, width and primary use for visible and short-wave infrared METimage channels

METimage is intended to provide high quality imagery data for global and regional NWP and NWC, and to support the sounding instruments on EPS-SG. Taking advantage of its large spectral range (0.44-13.5 μm), METimage will provide, among others, CTP products based on the use of visible imaging in the oxygen A-band. The goal of the present study “O₂ band Cloud Top Pressure for METimage” is to establish and demonstrate an appropriate CTP-O₂ retrieval scheme based on METimage observations. The objectives are as follows:

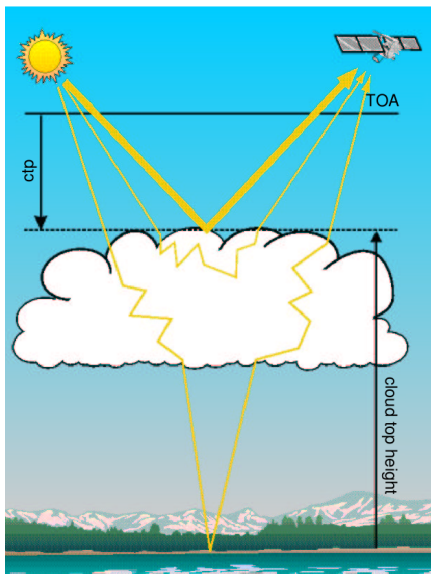
- To consolidate the CTP-O₂ retrieval scheme proposed for METimage through a literature survey on state-of-the art methods. LUT based methodologies are currently the preferred option for EUMETSAT and the review should concentrate on application of these. The review should however detail alternative methods where advantages (in accuracy, maintainability, performance etc) are clearly documented. Attention should be given to the definition of the LUT structure, that is, in content, parameter resolution, computational access and interpolation efficiency.
- To identify and characterise candidate radiative transfer models (RTMs). The requirements on RTMs suitable for CTP-O₂ retrieval should be identified and documented and a list of candidate models established. The capabilities, characteristics and inputs to these RTMs will be established and documented (as detailed in Sect. 2.1.2 and 2.1.3 of the SOW).
- To establish a source of proxy data suitable for testing the simulated LUTs and the overall METimage CTP-O₂ retrieval scheme (as detailed in Sect. 2.1.4 of the SOW).
- To generate test LUTs following the prescriptions of Sect. 2.2.1 of the SOW.
- To develop demonstration code for CTP-O₂ retrieval and demonstrate it using the proxy data and LUTs (as detailed in Sect. 2.2.2 of the SOW).
- Evaluate the performance and limitations of the METimage CTP-O₂ retrieval scheme and identify possible open issues and future developments (as detailed in Sect. 2.2.3 of the SOW).

Some fundamentals for the retrieval scheme were already stated by EUMETSAT:

- The optimal estimate method must be used.
- A Levenberg-Marquardt iteration process must be used.
- As already mentioned, the direct model must be represented by a Look-Up Table

These are used as a guide line during the study.

2 LITERATURE SURVEY ON RETRIEVAL METHODS



(source: Fischer et al. [2003])

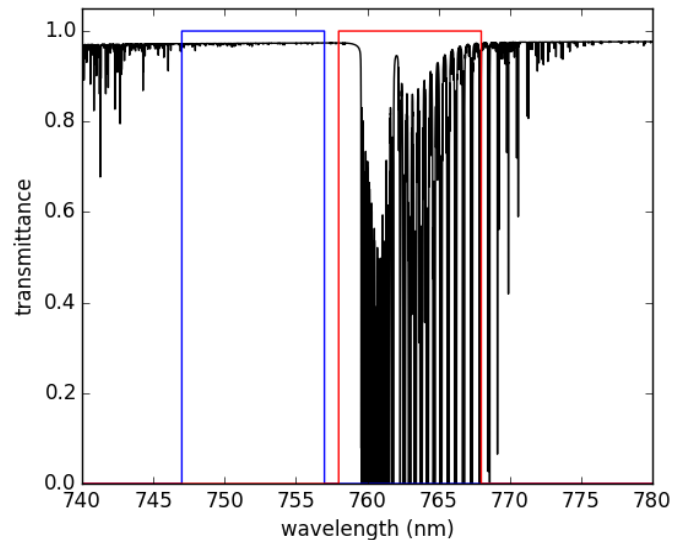


Figure 2.1: **(Left)** Schematic representation of the variety of possible photon path in cloudy atmosphere. **(Right)** AFGL Tropical atmosphere transmittance spectrum around A-band O₂ band for an airmass of 1. METimage filters VII-4 and VII-5 are over-plotted in blue and red respectively. The ISRF are modelled as a rectangle function on the present graph.

Several bibliographic study on the topic of cloud top position retrieval and especially using O₂ A-band were already performed. To write an other one without plagiarising those is a hard task. PhD thesis of Marine Desmons [Desmons 2014] and Rasmus Lindstrot [Lindstrot 2009] as well as the report Fischer et al. [2003] were particularly inspiring and used as starting point.

Either active or passive sensors can be used. Due to their better accuracy, active sensors are generally used as references to validate method based on passive sensors. However they have a poor spatial coverage due to their very narrow swath. The CALIOP lidar is reported to have an accuracy of 30 to 60 m [Winker et al. 2007]. Using passive sensors, the measurement of the temperature brightness in thermal infrared window is one of the most common method. This method is best adapted to high altitude and high opacity clouds but can lead to high uncertainties (up to 200hPa) in case of temperature inversion in the profile [Menzel et al. 2008]. Stereoscopy techniques can also be used that present the advantage not to rely on any ancillary data [Moroney et al. 2002]. Polarization by the Rayleigh scattering from above the cloud gives a proxy to the cloud top [Knibbe et al. 2000]. However, it does no work for geometry close to the rainbow, back-scattering or in the glitter. The used of differential gas absorption to retrieve the cloud top altitude was first mentioned by Hanel [1961]. The CO₂ slicing [Wielicki & Coakley 1981] method is based on the measurement of the radiance in the CO₂ absorption band between 13.3 and 15 microns. This was first introduced by McCleese and Wilson [1976]. The method is best adapted for middle to high altitude clouds [Menzel et al. 2008]. The method is expected to provide an accuracy of 25hPa in the best conditions.

The specific use of O₂ absorption was first mentioned by Yamamoto and Wark [1961]. To compare TOA

radiance measured at a wavelength falling into the oxygen A-band with an other one sufficiently close¹ but free of absorption directly gives a transmission ratio (see Figure 2.1). This transmission is related to the mean photon path-length. This photon path-length can be further interpreted in term of cloud altitude. This method is equally sensitive to low and high clouds and is not sensitive to temperature profile inversion. The complexity of absorption/scattering coupling as a function of the atmosphere content and surface characteristics is the main source of error in doing this interpretation of the photon path-length (see Figure 2.1, left panel). Several theoretical studies were performed to report on the various parameters that impact the retrieval (e.g. Wu [1985], Fischer and Grassl [1991], Kuze and Chance [1994]). Those first theoretical studies emphasised the importance of an accurate treatment of the photon multiple scattering on either molecules and the cloud it self. The photon penetration problem makes the use of a radiative transfer computation a necessary step for the proper cloud top retrieval. The applicability of this technique was first demonstrated using aircraft measurement (Saiedy et al. [1965], Fischer et al. [1991]). From the Fischer et al. [1991] measurements, the accuracy of the cloud top retrieval was reported to 40 m above a stratocumulus deck in comparison to LIDAR measurement taken in the same flight. The method was then applied to satellite based instrument like GOME, POLDER, MERIS, MOS or SCIAMACHY. Measurements in the O₂ A-band were also used for surface pressure retrieval (Dubuisson et al. [2001], Ramon et al. [2002]) or aerosol altimetry (Dubuisson et al. [2009]).

2.1 Theoretical studies on O₂ CTP retrieval

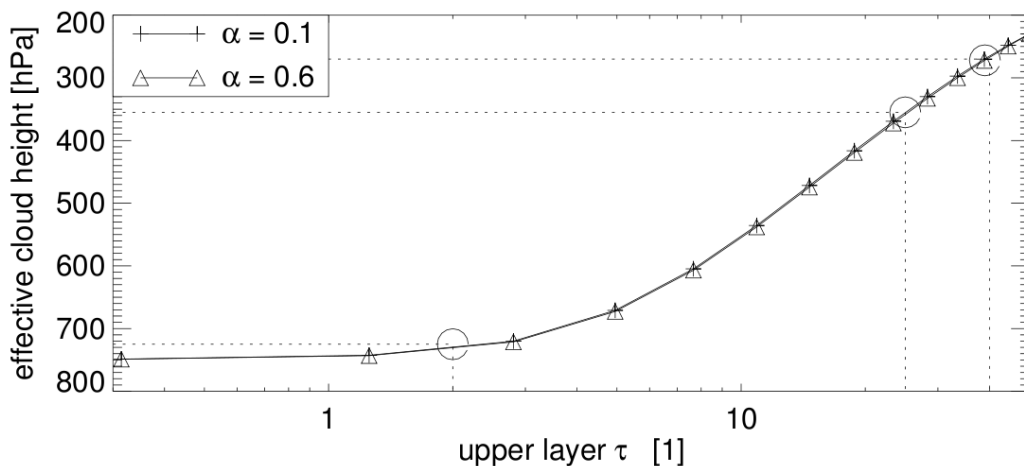


Figure 2.1.1 Effective single_layer cloud top pressure, depending on distribution of optical thickness for two layered cloud with combined optical thickness of 50. The lower layer top is at 750hPa while the upper layer top is at 230hPa. Note: curves are identical for surface albedo of 0.1 and 0.6. Source: Preusker and Lindstrot [2009]

Fischer and Grassl [1991] focused on liquid cloud in plan-parallel atmosphere and nadir observation. They used radiative transfer modelling to perform an analysis of possible perturbing parameters in cloud top detection. They conclude that:

1. The most important quantity to the radiance ratio 761/755 nm is the optical depth of the cloud that can be retrieved from 755 nm radiance.
2. The vertical structure of the cloud is also critical for this ratio, also for high opacity regime

¹ So that the scattering properties of the atmosphere for those two wavelengths are as close as possible.

3. The influence of varying the cloud droplet size distribution is minor
4. The surface albedo has to be known for clouds with opacity < 5.
5. Sun elevation impact the ratio (easily constrained).
6. The vertical temperature profile has to be considered

They reported two procedures that can be used to retrieve the cloud top altitude: (i) the first only makes use of two channels ($\Delta\lambda=1\text{nm}$) for which only the opacity and CTP can be retrieved with an accuracy of 200m at a given mean vertical liquid water content and for opacities > 5. (ii) The second procedure requires the use of 16 wavelength channels (with $\Delta\lambda=1\text{nm}$ again) to be able to retrieve the cloud height, including two cloud layers and varying liquid water path cases, with an accuracy of 50m for a radiance accuracy of 1%.

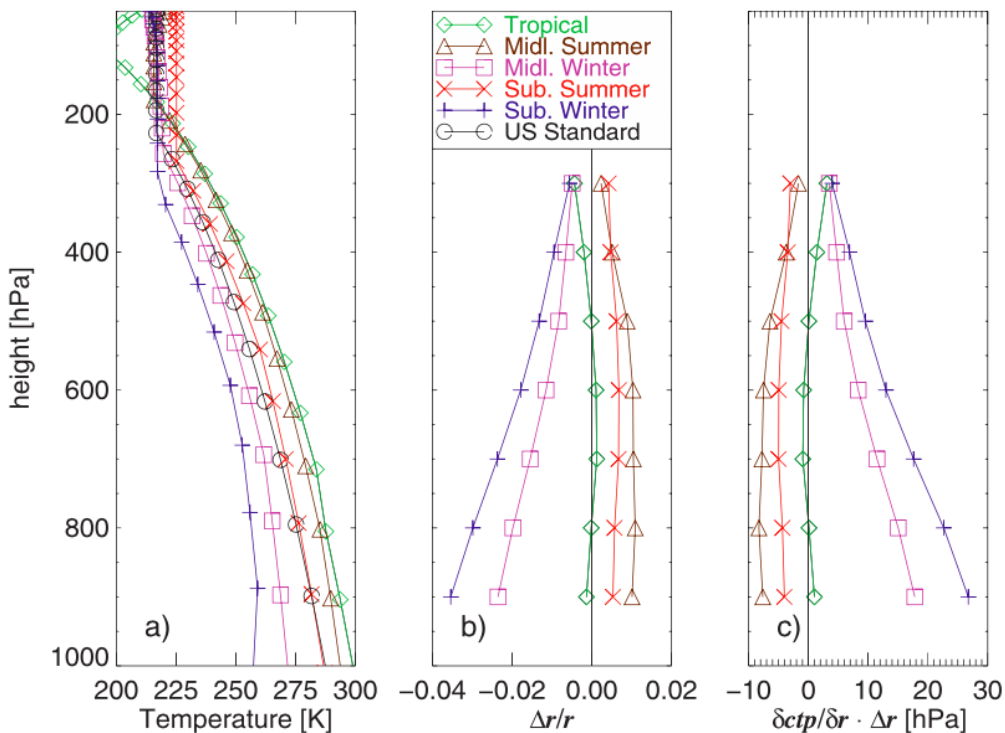


Figure 2.1.2 (left) Temperature profiles [McClatchey et al. 1972], (middle) relative change of MERIS 11/10 channel (see figure 2.3.1) ratio depending on cloud height and temperature profile as compared with a U.S. standard profile, and (right) equivalent change in hPa. Source: Preusker and Lindstrot [2009]

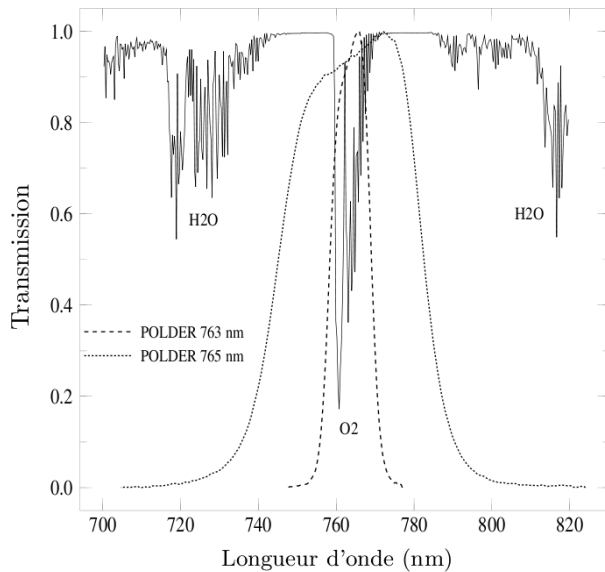
O'Brien and Mitchell [1992] found that the cloud top height over optically thick clouds can be retrieved with an accuracy of 5hPa without a priori constrains on micro-physical parameters as long as the spectral resolution of the measurement is at least 1 cm^{-1} with a signal to noise ratio better than 10000:1. They also mentioned that a good knowledge of the temperature profile and of the aerosol content is crucial. Mitchell and O'Brien [1987] stated that the temperature profile should be known to 1K in order to retrieve the surface pressure with 2hPa accuracy.

More recently, Preusker and Lindstrot [2009] performed an other sensitivity study. They also used a plan

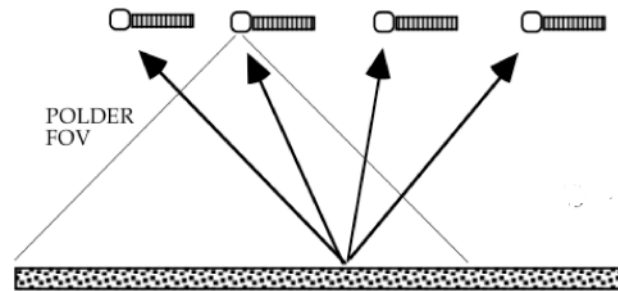
parallel RTM and worked with two channels (one in the window and one in the O₂ A-band with MERIS characteristics, see section 2.3). They concluded (as seen on Figure 2.1.1) that the biggest source of error for an algorithm based on such channels is the presence of multilayer situation since the information content is not sufficient to retrieve either the CTP and vertical distribution. Figure 2.1.1 shows the effect on the effective single layer cloud top pressure for a two layers (one at 750hPa and an other at 230hPa) situation of combined optical thickness of 50 and varying the opacity ratio between the two layers. As mentioned is their results, the impact of a moderately thin cloud above a lower cloud does not impact too much the lower cloud CTP retrieval. Contrarily, even for opacity of several tens, the upper cloud retrieval is very impacted by the lower level cloud. They also concluded that for single layer cloud of opacity > 2 , the error due to cloud micro-physics (i.e. phase function) and temperature profile does not exceed 10 and 20hPa. They reported on the importance to know the surface pressure and albedo with high precision in case of optically thin clouds. On the other hand they reported that the addition of other moderately resolving channels ($\Delta\lambda = 1.25\text{ nm}$) in the O₂ absorption band provide a limited increase of the information content about the vertical structure because of the noise cancellation effect and thanks to a slightly differing sensitivity to CTP and geometrical thickness in the R and P branch of the O₂ A-band. Finally, they state that the minimum spectral resolution required to separated CTP and the extinction profile effect that is hidden in individual spectral absorption lines is 0.1 nm.

Preusker and Lindstrot [2009] also studied the impact of the temperature profile on the CTP retrieval for various standard profile and CTP (see figure 2.1.2). They concluded that “if one disregards the subarctic winter profile because of the lack of sunlight, the maximum difference found is on the order of 20 hPa for low clouds and is much lower for high clouds. An underestimation of the temperature profile causes an underestimation of CTP and vice versa. However, the errors are small in comparison with other error sources.”

2.2 PARASOL/POLDER CTP retrieval



source: Buriez et al. [1997]



source: Bréon and Parosol team [2006]

Figure 2.2.1: **(Left)** Atmospheric transmission around the O₂ A-band together with the two POLDER channels at 763 and 765 nm. **(Right)** Principle of multi-view angle observation. The wide angle camera allows one to take successive pictures of the same target with different view geometries as the platform goes on its orbit.

The POLDER instrument (Polarization and Directionality of Earth's Reflectances, Deschamps et al. [1994]) was a multi-spectral and multi-angle polarized radiometer. There were three POLDER instruments. The two first flew on board ADEOS platforms in 1996 and 1997. The third flew on-board a CNES Myriade platform between 2004 and 2013. As seen on Figure 2.2.1, the wide angle camera allows one to take successive pictures of the same target with different view geometries (up to 14) as the platform goes on its orbit, thus providing the multi-view capability. Among the 9 different spectral bands of POLDER, two provided a measurement of the transmission through the O₂ A-band (see Figure 2.2.1). Those two channels are centred at about the same wavelength (765 and 763 nm) but one has a FWHM of 11 μm while the other has a FWHM of 38 μm . Those two channels do not measure the polarization.

2.2.1 Operational retrieval algorithm

The POLDER cloud top position retrieval was the first operational from satellite based data and was first developed by Buriez et al. [1997]. The algorithm did not directly make use of RT computation and rather rely on a parametrization that considered a perfect reflector as the cloud. It thus neglected multiple scattering within the cloud and from Rayleigh, as well as cloud/surface interactions. As summarized in Ferlay et al. [2010], the parametrization is as follows: "It is assumed that, after correction for the weak absorption of gases other than oxygen, 1) the reflectance I_{765} at 765 nm is a weighted sum of the reflectance I_{763} at 763 nm and the cloud reflectance I^* and 2) the reflectance at 763 nm is equal to I^* times the oxygen transmission T_{O_2} of the atmosphere above it. The implicit assumption is thus that the cloud albedo is equal to unity. For each viewing direction, I^* and T_{O_2} are obtained from the ratio of I_{763} and I_{765} , and from T_{O_2} -given the air mass- the cloud apparent pressure P_{app} . Cloud oxygen pressure P_{O_2} is obtained from P_{app} when the cloud spherical albedo is higher than 0.3 after correction of the surface effect over land [Vanbaucé et al. 2003]". The algorithm makes use of pre-computed T_{O_2} for various P_{O_2} , various geometrical conditions and various

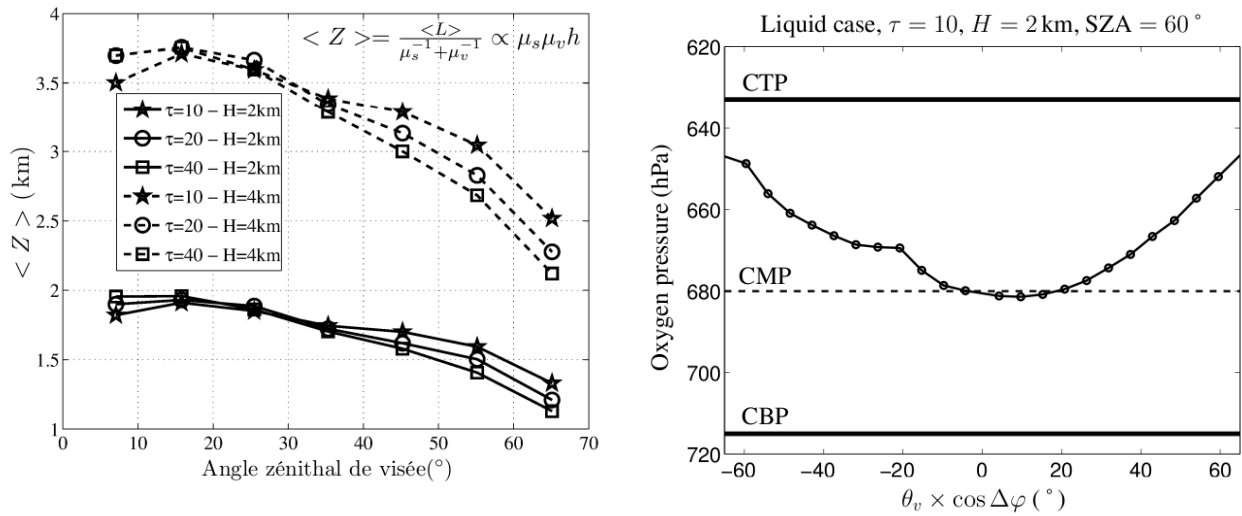
standard atmospheric profiles using a line-by-line-model and spectroscopic parameters from HITRAN 2004 [Rothman et al. 2005].

It must be noted that the correction for surface contribution (for pixel over land with cloud spherical albedo < 0.75) makes use of a LUT. The fraction of photons directly reflected by the cloud, r , is calculated using $r = R_{765}^0 / R_{765}$ where R_{765} is the reflectance measured by POLDER after correction for gaseous absorption and R_{765}^0 is the reflectance that would be observed if the surface was black. In practice, R_{765}^0 is obtained by using the cloud spherical albedo determined from POLDER measurements at 670 nm and look-up tables (LUTs) of calculated reflectance at 765 nm. On the other hand, the spherical albedo is obtained from the “cloud optical thickness” algorithm that also makes use of LUTs.

The P_{O₂} obtained for all viewing geometries are averaged and a corresponding standard deviation $\sigma_{P_{O_2}}$ is given. Because of the pure reflector assumption, P_{O₂} is systematically larger than the actual CTP. The bias essentially depends on the photon penetration into the cloud. It is lower for optically thick, geometrically thin clouds. P_{O₂} seems to be closer to the pressure of the geometric middle of the cloud [Vanbauce et al. 2003]. On the other hand, Vanbauce et al. [1998] showed a bias of 180hPa compare to infrared measurement with METEOSAT.

2.2.2 Improved algorithm

Ferlay et al. [2010] evaluated the potential of the use of multi-viewing POLDER capabilities to better characterise the true meaning of the retrieved P_{O₂} and to retrieve informations on the cloud geometrical thickness, h . Their work was restricted to liquid clouds. They used Monte-Carlo simulation to study the vertical penetration defined as $\langle Z \rangle = \langle L \rangle (1/\mu_0 + 1/\mu)^{-1}$ with $\langle L \rangle$ being the photon mean path-length, μ_0 and μ the cosines of solar and view zenith angles. They showed that $\langle Z \rangle$ and the amplitude of its angular variability is only slightly dependant on the optical thickness and micro-physical properties but strongly dependant on h (see Figure 2.2.2 left panel). This confirms the asymptotic relation from van de Hulst [1980], $\langle Z \rangle \propto \mu_0 \mu h$. Since P_{O₂} is sensitive to $\langle Z \rangle$, it is expected to vary accordingly as a function of h and the geometry. By running the P_{O₂} retrieval on simulated TOA (see for example Figure 2.2.2 right panel) Ferlay et al. [2010] illustrated the variability of P_{O₂} with respect to the viewing geometry and showed that the average P_{O₂} is close to the pressure of the middle of the cloud. They concluded that for optically thick enough clouds, P_{O₂} level (and its difference regarding the true CTP) mainly varies with h and that $\sigma_{P_{O_2}}$ is potentially highly correlated to the cloud geometrical thickness. Using a large set of POLDER data collocated with CPR and CALIOP, they confirmed (i) the small bias between the averaged P_{O₂} and the actual CMP (Cloud Middle Pressure) for mono-layer clouds and (ii) the sensitivity of $\sigma_{P_{O_2}}$ to h .



source: Ferlay et al. [2010]

Figure 2.2.2: **(Left)** Equivalent vertical penetration $\langle Z \rangle$ within cloud layers of various optical and geometrical thickness for the case of liquid clouds with overhead sun at zenith. Cloud base is fixed at 1-km altitude. The definition of $\langle Z \rangle$ and the asymptotic expression derived from van de Hulst [1980] are over-plotted as a reference. **(Right)** Variation of retrieved P_{O_2} with the viewing zenith angles θ_v in the solar plane (φ is the measurement's relative azimuth) for simulated TOA radiance. Characteristics of the case study are indicated in the title. Horizontal lines indicate the level of cloud top, middle, and base pressures (denoted respectively by CTP, CMP, and CBP). The angularly averaged P_{O_2} is 667hPa and $\sigma_{P_{O_2}}$ is 11hPa. Discontinuities of the directional cloud oxygen pressure at -60° and -20° are signatures of cloud scattering phase function.

Desmons et al. [2013] intended to use Ferlay et al. [2010] results to derive unbiased middle (CMOP) and top pressure (CTOP) products for mono-layer ice and liquid clouds. The bias on P_{O_2} regarding the actual CMP is mainly function of μ_s (solar zenith angle) and τ (cloud optical thickness). CMOP is then estimated through $P_{O_2} - f(\mu_s, \tau)$, where $f(\mu_s, \tau)$ is an empirical relationship derived by comparing POLDER P_{O_2} to the actual CMP from CPR/CALIOP for a given set of data: $P_{O_2} - \text{CMP} = f(\mu_s, \tau)$. CTOP bias regarding the actual CTP is mainly function of $\sigma_{P_{O_2}}$. CTOP is then estimated through $P_{O_2} - f(\sigma_{P_{O_2}})$, where $f(\sigma_{P_{O_2}})$ is an empirical relationship derived by comparing POLDER P_{O_2} to the actual CTP from CPR/CALIOP for a given set of data: $P_{O_2} - \text{CTP} = f(\sigma_{P_{O_2}})$. The score obtained by CTOP, defined as the confidence in the retrieval for a particular range of inferred value and for a given error, is higher than the one of MODIS collection 5 CTP estimate. The CTOP accuracy is best for clouds with high vertical extent (deep convective clouds, cirrostratus, or altostratus). For low level clouds (CTP > 680hPa), CTOP and CMOP tend to be underestimated. They used the difference between CTOP and CMOP to study the retrieval of the cloud vertical extent. They also studied the correlation between $\sigma_{P_{O_2}}$ to h (from CPR/CALIOP). They note that this correlation is not good for ice cloud probably because of a more complex micro-physics. This correlation for liquid cloud appears to be stable spatially and temporally except over land during winter month. They elaborate a (μ_s, τ) parametrization to link h to $\sigma_{P_{O_2}}$. Above the ocean for 2008 the mean difference between the actual h and the one retrieved from parametrization is 5m. The one from CTOP-CMOP is -12m. The standard deviation of the mean difference is close to 1000m for the two methods.

The POLDER algorithm does not make use of RT computation. It is an analytical formulation and is then very fast. The downside is that not to account for the photon penetration into the cloud through a RT use in POLDER retrieval introduced a large bias. The bias could be lower thanks to the multi-directionality and using climatologies to derive empirical relationship.

2.3 MERIS CTP retrieval

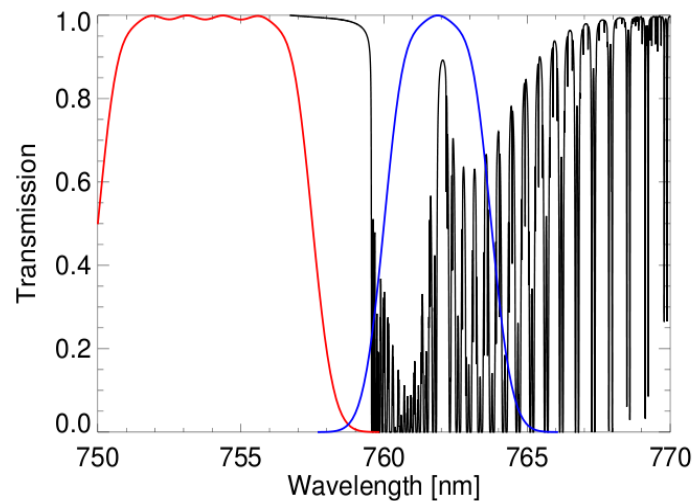


Figure 2.3.1: MERIS channel 10 (red) and 11 (blue) transmission overplotted on atmospheric oxygen transmission. source: Lindstrot [2009]

MERIS was a medium spectral-resolution imaging spectrometer [Rast et al. 1999] that was launch on board ENVISAT (Environmental Satellite) on March 1st, 2002. ENVISAT orbits is sun synchronous at an altitude of 800 km, crossing the equator at 10:30 AM local time for descending node and 98.5° inclination. MERIS consists of 5 identical push-broom imaging spectrometers arranged in a fan shape configuration which covers a total field of view of 68.5° and spans a swath width of around 1150 km. The spectral dispersion is achieved by mapping the entrance slit of a grating spectrometer onto a CCD array. The integration time, instrument optics and CCD array resolution are adjusted such that MERIS has a spatial resolution of 260 m x300 m and a spectral sampling of 1.25 nm. Not all the CCD pixel measurements are transmitted to the ground individually. Some spectral channels were defined in width and position. The spatial resolution is reduced by a factor of 4 in reduced resolution mode. Among the 15 spectral channels that were defined (between 415.5 nm and 900 nm) two are dedicated to the cloud top pressure retrieval. These are (i) the channel 10 centred at 753.75nm with a FWHM of 7.5 nm and (ii) the channel 11 centred at 761.875nm with a FWHM of 3.75 nm (see figure 2.3.1). Preusker and Lindstrot [2009] showed that for MERIS channel characteristics, the sensitivity of the band ratio L_{11}/L_{10} to an error of FWHM or position is minimal for the wavelength 761.875nm that was chosen for MERIS definition. A “spectral smile” arises in the MERIS data due to the curvature of the image of the slit formed in the focal plane array, resulting in viewing angle-dependent central wavelengths of the spectral MERIS channels. This effect was fully characterized [Delwart et al. 2007] and a spectral index corresponding to any pixel of the L1b data is provided.

2.3.1 Operational retrieval algorithm

The MERIS CTP retrieval algorithm is described in Preusker et al. [2010]. Contrarily to the POLDER algorithm, it makes use of radiative transfer computation in order to take into account the photon penetration within cloud and cloud/surface interaction. The inverse problem is handle by the mean of a Neural Network. As stated by Preusker et al. [2010], Artificial Neural Networks (ANN) are able to reduce the size of the required database (regarding a LUT) and the computation times drastically (there is no interactive process at retrieval time). Matrices derived from a supervised learning procedure using simulation results, relate a vector of input information to a vector of cloud properties of interest. They are able to account for the non-linear correlation of the multi spectral radiances, cloud properties and cloud-top pressures.

The radiative transfer model MOMO (Fischer and Grassl [1984], Fell and Fischer [2001], also see section 3.1) was used to train the ANN. The code assumes plan-parallel media and can handle any vertical inhomogeneity of the media of any optical thickness. It can work with any spectral resolution. The simulation of radiances were done with an atmosphere divided into 78 layers. The gas absorption is parametrized using a k-distribution [Bennartz & Fischer 2000] based on HITRAN database [Rothman et al. 2005]. Optical properties of clouds and aerosols are computed with Mie theory and the phase function are truncated using the δ -M method [Wiscombe 1977].

For the training, the simulations included a broad number of combinations of atmospheric parameters like temperature and humidity profiles, cloud heights and thicknesses, surface albedo values, and aerosol loads:

- Aerosols are assumed to be of continental or maritime type with an optical thickness of 0.125 at 550nm. Regarding the cloud parameter
- Cloud droplets effective radius was varied. Varying combinations of the cloud optical thickness, the vertical profile and the cloud geometrical thickness are considered. The vertical profile of the extinction coefficient is supposed to be ‘triangular’ whereas the maximum appears in the upper half of the cloud. The optical thickness varies between 1 and 350 while the geometrical thickness varies between 0.1km and 10km. In that manner, the variability of penetration depth is considered. Therefore the calculations distinguish between 11 cloud types that are specified through the effective radius and ranges of optical thickness, cloud geometrical thickness, extinction coefficients, cloud-top pressure and cloud base pressure (see table 1 of Preusker et al. [2010]). For this investigation 2000 arbitrarily chosen cases are considered.
- The results of high spectral resolution measurements of various types of surfaces were used. Different types of vegetation, soil and snow as well as an ocean surface are considered, whereby the albedo and the albedo slope cover natural occurring values. In particular over vegetation the impact of the position of the red edge on the TOA radiances is included. The reflection at the surface is assumed to be isotropic.

It is noted that as for any other ANN retrieval algorithm, the choice of training and test dataset set is of major importance to ensure reliable results. The ANN is a three layers. The input contains the TOA reflectance of the MERIS Channels 10 and 11 the sun zenith angle, the viewing zenith angle, the azimuth difference, the albedo of the underlying surface, and the central wavelength of MERIS band 11. The channel 11 is corrected for residual stray light before the inversion [Lindstrot et al. 2010]. The accuracy of the product is given to be 30hPa.

Lindstrot et al. [2006] presented a work of validation of the MERIS Cloud-Top Pressure Using Airborne Lidar Measurements. It shows the good quality of the MERIS algorithm products over low level single-layer clouds. On average, the accuracy was found to be 24 hPa with a bias of -22 hPa . Stronger deviations of the retrieved cloud-top pressure from the true cloud-top can be expected for higher clouds, due to higher variability of the unknown cloud geometrical thickness, influencing the penetration depth of the radiation into the cloud. Regarding multi-layer situation, the retrieval is biased towards a level located between the cloud layers, provided that the upper cloud layer is optically thicker than ≈ 0.5 .

2.3.2 Other MERIS based CTP algorithm

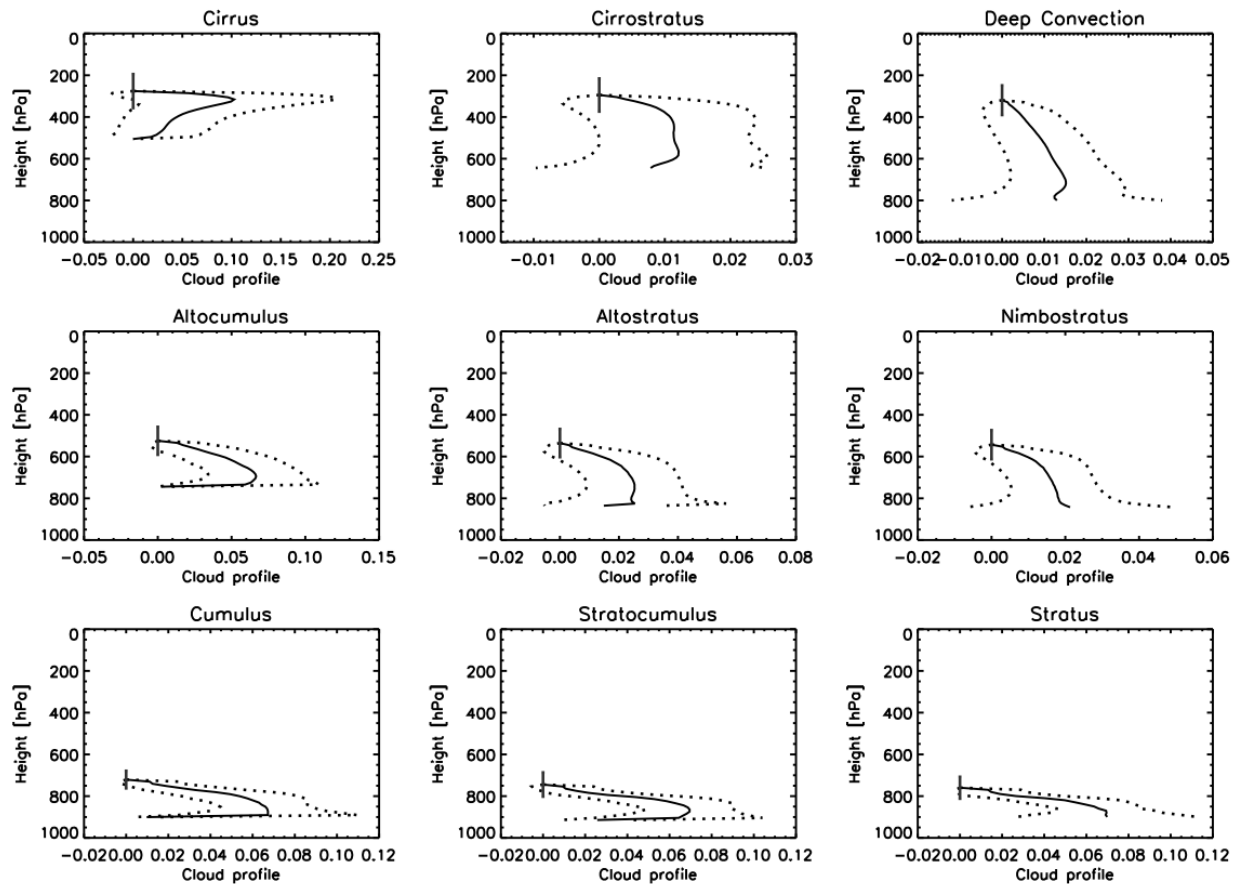


Figure 2.3.2: Average cloud vertical extinction profiles for nine cloud types (solid line) and standard deviation from the mean (dotted line), as well as standard deviation of the CTP (error bar on top). Source: Carbajal Henken et al. [2014]

FAME-C [Carbajal Henken et al. 2014] is a daytime cloud property retrieval that use AATSR and MERIS data both on-board Envisat. It is used in the frame of the ESA cloud CCI. The algorithm consists in two steps:

1. Cloud phase, cloud optical thickness, and effective radius are retrieved using AATSR near-infrared and visible channels, and subsequently cloud water path is computed. This retrieval is based on DCOMP algorithm [Walther & Heidinger 2012]. LUTs are used for top of cloud radiances without atmosphere and for black surface. Correction for Rayleigh, gas absorption as well as Lambertian contribution are done analytically. Switch between ice and liquid cloud is done based on the thermal infrared brightness temperature. See Carbajal Henken et al. [2014] for details.
2. Two cloud top height products are retrieved based on independent techniques. For cloud top temperature, measurements in the AATSR infrared channels are used, while for cloud top pressure, measurements in the MERIS oxygen A-band absorption channel are used. We focus on the MERIS retrieval.

All step 1 and 2 retrievals are done using an optimal estimate method with a Newton-Gauss iteration method. For the MERIS CTP retrieval, LUT are computed using MOMO (see section 3.1). It contains the radiance

ratio of channel 11/channel 10 as a function of cloud top pressure as well as cloud optical thickness, viewing geometry, surface pressure (varied above land but constant to 1013hPa over ocean) and the MERIS channel 11 center wavelength (to manage the spectral smile). A US standard atmospheric profile is used. The gas absorption is accounted for by mean of a k-distribution [Doppler et al. 2014] using the HITRAN database [Rothman et al. 2005]. The CTP ranges from 100 to 1000hPa in the LUT. For cloud layers below 440hPa, ice crystals are assumed with a fixed effective radius of 40 μ m; otherwise water droplets are assumed with a fixed effective radius of 10 μ m. In order to better handle the effect of photon penetration into the cloud, the vertical profile of clouds are varied as function of their COT and CTP based on a CPR/CloudSat climatology described in Carbajal-Henken et al. [2013]. The corresponding profiles are reproduced in figure 2.3.2. The profile switches from one to the other following the ISCCP classification. The total optical thickness of the cloud is adjusted following the result of the step 1 result.

The produced MERIS CTP were compared to ground-based cloud radars located at several Atmospheric Radiation Measurement (ARM) sites. It mostly shows an underestimation of cloud top heights when compared to radar observations. For mono-layer clouds, 61 targets are used. They found a bias of 0.5km and a RMSD of 2.0 km. They report that these relatively high value are essentially caused by mid-level and high level clouds. They also reported that to introduce non-homogeneous vertical profile (i) appears to eliminate the large bias obtained when assuming homogeneous profile and (ii) seems to enlarge the scatter due to the diversity of vertical profiles in real clouds. As expected, for multi-layer clouds, the bias and RMSD are greater. It is equal to -2.4km and 4.3km respectively.

Recently, Carbajal Henken et al. [2015] published a study in which they intend to exploit the difference between the FAME-C CTP retrievals (MERIS & AATSR) to infer information about the cloud vertical structure.

2.4 Other missions

MOS (Modular Optoelectronic scanner) satellite flew on board IRS3 (Indian Remote sensing Satellite 3). This instrument can be seen as a precursor for MERIS regarding the definition of the channels falling into the O₂ oxygen band and in the window channel. Preusker et al. [2007] developed an algorithm for the retrieval of the CTP using MOS data. They reported an accuracy of \sim 30hPa compared to radiosonde data for single-layer low level clouds.

GOME and SCIAMACHY are spectrometers. GOME (Global Ozone Monitoring Experiment) was a SCIAMACHY precursor. SCIAMACHY (SCanning Imaging Absorption spectroMeter for Atmosphere Chartography) flew on-board Envisat between 2002 and 2012. It measured the solar radiation reflected from the atmosphere in the wavelength range between 240 and 2380 nm with a resolution of 0.2 to 1.5 nm between 240 and 1750nm. As expected with such resolution, not only the cloud top pressure but also information about the cloud geometrical thickness can be retrieved with SCIAMACHY (e.g. Kokhanovsky et al. [2006a], Kokhanovsky et al. [2006b]). However only the cloud top height is retrieved in operational algorithms (Wang et al. [2008], Lichtenberg [2015]).

The Sentinel 5 spectrometer will fly on-board EPS-SG to provide ozone profiles, monitor various trace gases, monitor air quality and support climate monitoring by means of hyper-spectral soundings with a spectral resolution from 0.065–1 nm in the wavelength range from 0.27–2.4385 μ m, at a spatial sampling of 7 km for channels above 0.3 μ m. It is a heritage of GOME-2 and SCIAMACHY. This instrument should measure spectral radiance in the oxygen band A and B and will then bring complementary information to the

METimage measurements. This will also offer a potential for spectral calibration.

2.5 Conclusion regarding the METimage algorithm

Several parameters will impact the signal ratio VII-5/VII-4:

1. Cloud optical thickness (COT)
2. Cloud top pressure (CTP)
3. Cloud geometrical thickness and vertical profile
4. Surface properties (albedo, pressure)
5. Cloud micro-physics and primarily phase (liquid or ice)
6. Cloud fraction
7. Aerosol
8. Temperature vertical profile
9. Geometry (sun and view)

For METimage instrument characteristics, the impact of the CTP and vertical structure on the signal ratio can not be separated. As seen with the bibliographic study, an additional information content either from a multi-angular observation or from a better spectral resolution and additional channels in the O₂ absorption band is needed for that. The algorithm we propose will jointly retrieve COT and CTP. These two quantities will then be sampled in the LUT. The vertical structure can be varied but using an a priori parametrization regarding COT and CTP like in FAME-C algorithm [Carbajal Henken et al. 2014]. This will be limited to mono-layer clouds. Although it has a limited impact on the signal ratio [Preusker & Lindstrot 2009], the effective radius may also be parametrized using MODIS climatology. The impact of the effective radius will be studied in section 4. The phase can be varied based on a precomputed phase mask.

The geometry (view and sun) will be sampled in the LUT. Surface properties must vary. At least its albedo and pressure. We will study the impact of BRDF variation on the CTP retrieval in section 4. The presence of aerosols will impact the signal but the LUT approach prevents us to vary their characteristics. We will also assess the impact of aerosols in section 4. The temperature profile has a limited impact on the signal and we may fix it again because of the limiting varying parameters that can be set in the LUT.

The cloud fraction in a pixel has at noticeable impact on the signal. However, we do not intent to retrieve or even vary it in our day-1 algorithm. A more complex algorithm, making use of more METimage channels may include that in the future (see EUMETSAT [2011]).

3 RADIATIVE TRANSFER MODEL CANDIDATES

Emde et al. [2008] produced a good review on available radiative transfer tools. As stated in that review, there is a huge number of such tools that were developed since the 1950s. Their review then focuses on well-known, well-tested models and also codes that are used in the remote sensing community.

In the following section, we introduce some candidate tools. We describe in further details the ARTDECO package that will be used for the study.

In the context of the present study, the following characteristics are a pre-requisite for use as a forward model:

- Availability (code and documentation) and compatible licensing status
- Proper scattering / absorption coupling (i.e. proper RTE resolution)
- Multiple scattering accurate treatment including surface/atmosphere interaction for non Lambertian surface possibility (BRDF)
- Maintenance and spectroscopic upgrade possibility, e.g. if new gas HITRAN absorption cross sections to be used, etc
- Possibility to easily and accurately represent vary atmosphere content
 - Meteorological profile
 - Scatterer definition (user optical properties for aerosols and clouds)
 - adequate vertical resolution / layer numbers: possibility to set arbitrary vertical distribution for scatterers.

Of course a model to be used in that context must demonstrate sufficient accuracy. The gas absorption can either be treated with a line by line approach or a parametrization (e.g. k-distribution) as long as the accuracy requirement is achieved. We note that the CPU demand is secondary in LUT creation but could still be problematic because of the great number of cases to compute for the LUT. The line by line use then seems inappropriate.

The curvature (spherical atmosphere) impact depends on the view and solar zenith angle to be considered for the produce. For METImage, the view zenith angle (ground view toward the satellite) is up to $\sim 67^\circ$ and except for high latitudes (high sun zenith angles close to poles) a plan-parallel approximation is a reasonable. The performance regarding CPU demand is considered secondary because the code will not be used on-the fly during the inversion.

The 3D effects are of great importance in modelling the TOA radiances of cloudy fields [Miller et al. 2014]. However, the use of a model accounting for those effects is well beyond the scope of the present work.

The 6SV code [Vermote et al. 1997] last improvement are described in Kotchenova et al. [2006]. This code can not handle clouds and is then not appropriate for the present problem. We can note that this code is based on the successive order of scattering like the SOS code developed at LOA [Lenoble et al. 2007]. That method is not well adapted for high opacities and there is currently no released version of such a code able to account for gas absorption.

Streamer [Key & Schweiger 1998] appears to be limited in terms of versatility for the cloud vertical distribution and gas spectroscopic specifications and maintenance.

It is interesting to note the LIDORT/VLIDORT code [Spurr 2006] is available and able to accurately compute the Jacobians because it was linearised. In most other models, this is done by finite differences. However in the framework of a LUT approach, to benefit from that accurate treatment would require the creation of Jacobians LUT beside the forward model LUT. This would imply to lower the forward model LUT size so that both LUTs can fit into the RAM. We will rather use the full RAM for the forward model LUT so that it can be as accurate as possible. The Jacobians can be computed (with lower accuracy indeed) from the forward model LUT.

3.1 MOMO

MOMO (Fell and Fischer [2001], Hollstein and Fischer [2012]) has been widely used in the context of O₂ A-band cloud top pressure study and retrieval. It then demonstrated all capabilities for it. Especially, it was used as the forward model for the MERIS retrieval (see Preusker et al. [2010], Carbajal Henken et al. [2015]). MOMO was described in several papers and technical notes. The RTE solver is matrix operator based. It is especially well suited for optically thick media and operate in plan-parallel approximation. The description of cloud properties (optics, vertical distribution) is appropriately versatile. The gas absorption can be accounted for with a k-distribution parametrisation [Doppler et al. 2014]. The ocean BRDF can be accounted for but no description for land BRDF could be find. MOMO is not publicly available but was already provided to various collaborators in the past.

3.2 SCIATRAN

SCIATRAN [Rozanov et al. 2005] has all capabilities required for use in the context of O₂ A-band cloud top pressure study and retrieval. It is publicly available at <http://www.iup.uni-bremen.de/sciatran> and well documented. It was extensively used in the framework of SCIAMACHY and GOME missions. It can be run in spherical mode. The RTE can be solved with the discrete-ordinate method with a single scattering correction. The gas absorption can either be treated with a line by line approach or with a k-distribution parametrisation. Either land and ocean BRDF can be modelled. SCIATRAN can handle an arbitrary number of particles (aerosols and/clouds) with arbitrary vertical distributions. A library of optical properties is available and the user can give additional particle properties as an input.

3.3 LibRadtran

LibRadtran (library for radiative transfer, Mayer and Kylling [2005]) is a toolbox including several database and RTE solvers. It gathers all capabilities needed for O₂ A-band cloud top pressure study and retrieval and is publicly available at <http://www.libradtran.org>. The gas absorption can be handled with a line by line approach or a k distribution parametrization. Spectroscopy and k-distribution coefficients can be easily changed through input files. Cloud and aerosol properties (either optical or the vertical distribution) can be set arbitrarily through input files. The ocean and land surfaces can be represented with a BRDF. The land BRDF model is the one of Rahman et al. [1993]. The RTE solver DISORT [Stamnes et al. 1988] is used when the surface is represented with a BRDF.

3.4 ARTDECO (including GAME)

ARTDECO ('Atmospheric Radiative Transfer Database for Earth and Climate Observation') is a numerical tool that gathers models and data for the 1D (plan-parallel approximation) simulation of Earth atmosphere

radiances and radiative fluxes as observed with passive sensors in the UV to thermal IR range. It is developed and maintained at the Laboratoire d'Optique Atmosphérique and is funded by the TOSCA program of the French space agency (CNES).

In ARTDECO, users can either access libraries for the scene definition (meteorological profile, surface, aerosol and cloud description, gas absorption, ISRF, etc) or use their own description through input files. The user can choose among available models (several methods for the truncation of the phase matrix, several RTE solver) to compute radiative quantities corresponding to the scene. Technical parameters for these models are also accessible through input files.

Several libraries of aerosols and clouds optical properties are available like the OPAC library [Hess et al. 1998] or the ice model from Baum et al. [2014]. A Mie routine can be used to adapted new properties for spherical particles. Different kind of aerosols and clouds can be mixed in the atmosphere. Their vertical distribution profile can be arbitrarily specified together with the meteorological profiles. The number and thickness of layers to discretize the vertical profile with is arbitrary.

Several BRDF/BPDF models are available. For the ocean, the model used for 6SV is used [Kotchenova & Vermote 2007]. However, the glitter model was replaced by the one described in Mishchenko and Travis [1997] which also accounts for shadowing effects and follow the Cox and Munk [1954] wave slope distribution. For land surfaces BRDF, the Li-Ross model with hot spot [Maignan et al. 2004] is available. The Raman-Pinty-Verstraete model [Rahman et al. 1993] is also available. The BPDF for land is the one from Maignan et al. [2009].

The available RTE solver are:

- The version 2.0 of DISORT [Stamnes et al. 1988]. It is a scalar RTE solver based on the discrete ordinate method. It is widely used, very stable and well documented. It allows to account for thermal emission and can handle BRDF for the surface.
- A 1D Monte-Carlo code developed at the Laboratoire d'Optique Atmosphérique. It accounts for polarization and can handle BRDF/BPDF surface definition.
- An adding-doubling code developed at the Laboratoire d'Optique Atmosphérique. It is based on the de Haan et al. [1987] paper. It accounts for polarization and can handle BRDF/BPDF surface definition. That code is used for the "Radiation Budget and Clouds" inversion pipeline of PARASOL/POLDER mission.
- A single-scattering approximation code that accounts for polarization and can handle BRDF/BPDF surface definition. That code can be used for fast resolution in case of very low optical depth, to test the single scattering approximation against other RTE solvers. However, its main usage in ARTDECO is to apply the single scattering correction (TMS, see below).

The user have access to three different methods for the phase matrix truncation: (i) δ -M from Wiscombe [1977], (ii) the delta function approximation from Potter [1970] and the (iii) the δ -fit from Hu et al. [2000]. The radiance can be corrected for the first order scattering using the TMS method [Nakajima & Tanaka 1988].

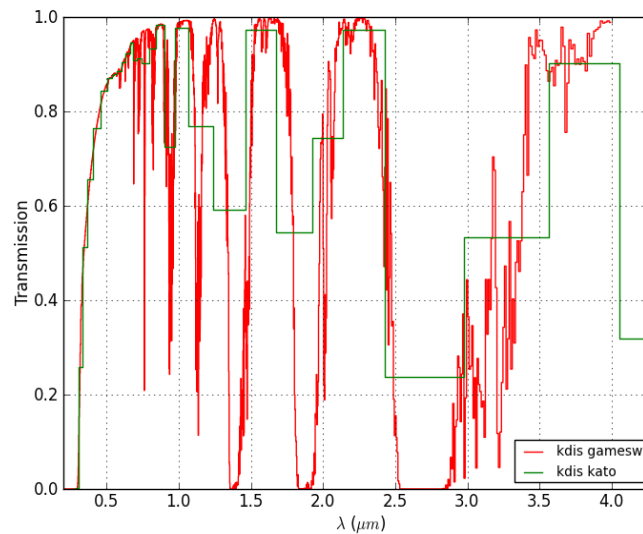


Figure 3.4.1: Transmission as computed with ARTDECO for US62 atmosphere with GAME and Kato et al. [1999] k-distribution binning. Note that for Kato, the bins width is representative while the bin range limits are not strictly reproduced on the plot.

The gas absorption can be accounted for with the correlated k-distribution technique [Lacis & Oinas 1991] from line-by-line reference calculations, and with the CKD parametrization [Clough et al. 1989] for absorption continua. The so called GAME k-distribution coefficients following Dubuisson et al. [1996], Dubuisson et al. [2004] and Dubuisson et al. [2005] is available in ARTDECO. It is defined for the spectral range from 0.2 to 50 μm for H₂O, CO₂, O₃, O₂, N₂O, CO, CH₄, N₂, NO₂, SO₂. An other k-distribution from Kato et al. [1999] that is well adapted for computation of integrated flux over the solar spectral range is available. Figure 3.4.1 shows transmission spectrum for those two k-distributions in the solar spectral range. Specific coefficient for large band instrument can be computed from spectroscopic database (e.g. HITRAN 2012) accounting for a given arbitrary ISRF. This was already done for a set of captor : 3MI, METImage, PARASOL, POLDER, MODIS, MERIS. The user can use its own correlated k-distribution coefficients.

The ARTDECO RT package was validated against several benchmark (e.g. Kokhanovsky et al. [2010]) and other RT tools (e.g. original GAME code of Dubuisson et al. [1996], CNES OS code of Lenoble et al. [2007]). It was used to perform a study on the impact of the phase matrix truncation on the polarized reflectance modelling [Compiegne et al. 2013]. It will soon become publicly available through the ICARE data centre (<http://www.icare.univ-lille1.fr>). It is documented through a wiki web page.

ARTDECO original code is fully written in Fortran. Lately, a python shell was developed that can substitute the Fortran code for I/O access, variable initialisation and calling sequence of the different Fortran routines. It improves the performance of ARTDECO in case of recursive calls and the flexibility for Input/Output (e.g. easy quick plot look, easy HDF5 files handling). The python shell also serve as an interface for parallel computation on a cluster of computer (using tools like HTCondor or Qsub/SGE). It is intended to allow the evolution toward a line-by-line treatment of the gas absorption.

ARTDECO was used for the METImage and 3MI radiance simulator in the context of the EUMETSAT

project “Test Data for the EPS-SG instruments METimage and 3MI”. Although the simulator was used only for the visible/SWIR range in that project, it was also set and validated for the thermal infrared part. In that regard, the ARTDECO tool then already demonstrated the flexibility necessary to reproduce accurately the radiance for any realistic scene.

4 SENSITIVITY STUDY

4.1 General approach



Figure 4.1.1: Modelled ISRF shape for the VII-5 channel.
FWHM = 10 nm

We performed the sensitivity study with the ARTDECO radiative transfer package (see section 3.4). We computed reflectance for various atmosphere and ground properties. We use specifically the DOAD adding and doubling RTE solver. The phase function of any used particle (either cloud or aerosols) are truncated with the δ -M method. We use 8 computational angles (streams) and apply the single scattering correction (TMS) to the TOA reflectance. For a pure scattering liquid cloud of opacity 5.0 (see benchmark from Kokhanovsky et al. [2010]), the obtained TOA radiance is accurate to better than 0.4% out of the rainbow and glory geometries. Unless directional effects are looked for, the sun is placed at a zenith angle of 30.0° and the observation is at nadir (out of the rainbow and glory). The polarisation is neglected in the computation. It has a negligible impact at studied wavelengths. The Rayleigh scattering is accounted for with an opacity following Hansen and Travis [1974] and a depolarisation factor of 0.0279 [Young 1980].

Specific k-distribution for the METimage channels were derived using a line-by-line model and the HITRAN database [Rothman et al. 2009]. Except for VII-5 channel, the ISRF are modelled as rectangle function with the position and FWHM specified in table 1. For the VII-5 channel, wings were added to the ISRF that represents 1% of the full ISRF transmission. Either the heart and the wings of the ISRF are modelled through rectangle functions having a FWHM of 0.01 nm (as specified in table 1). The resulting shape is shown in figure 4.1.1. The whole ISRF is centred at 763 nm (as specified in table 1). With the present ISRF definition, only O₃ and O₂ absorb significantly (transmission < 99.9%) in channels of interests for our study (670, 752, 763 and 865 nm). The others gases are not accounted for in the computation. Figure 4.1.2 shows the error on VII-5 channel gas transmission obtained for a correlated k-distribution for various numbers of k-interval and various airmass. The error is obtained by comparison to the line-by-line computation. We see that the error is less than 1.5% for airmass < 10. In order to lower the CPU demand, we use the case with 20 k-intervals in the following.

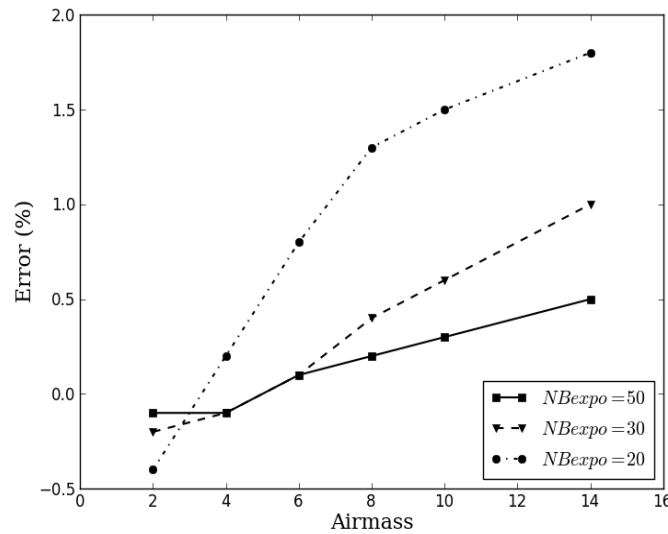


Figure 4.1.2: Error on VII-5 channel gas transmission obtained for a correlated k-distribution for various numbers of k-interval and various airmass. The error is obtained by comparison to the line-by-line computation

The meteorological profile is the AFGL US62 from Anderson et al. [1986]. For computation in band VII-5 the atmosphere vertical resolution is re-sampled to 1.0 km outside the cloud while it is set to 50m inside the cloud. We cut the atmosphere at 50 km (0.98 hPa). The vertical distribution for ice (liquid) clouds is the one derived for Cirrostratus (Stratocumulus) by Carbajal-Henken et al. [2013] (see figure 2.3.2). Unless the sensitivity to that parameter is studied, the CGT is set to 1 km.

The liquid cloud optical properties are computed using the Mie theory. The size distribution of droplets follows a log-normal distribution with an effective variance of 0.09. The optical properties of ice clouds are those of General Habit Mixture ice particles from Baum et al. [2014]. Unless the sensitivity to that parameter is studied, we fix the particle effective radius to 14 and 25 microns for liquid and ice clouds respectively. Those values are typical average value derived with MODIS [King et al. 2013].

Figure 4.1.3 shows the band VII-5 and VII-4 reflectance ratio, $R = I_{763}/I_{752}$, as a function of the cloud opacity (COT) and CTP obtained with the model described above. The opacity range between 0.5 and 500 for both ice and liquid cloud. The CTP goes from 400 to 900hPa for liquid cloud and from 100 to 700 hPa for ice clouds. The surface is assumed to be Lambertian. The left panels show the liquid cloud case while the right panels show the ice cloud case. As expected, with a black surface, we see that the ratio essentially varies with CTP. Otherwise, the signal is dominated by the surface for low opacity clouds and the ratio is less sensitive to CTP. This effect is exacerbated for an a bright surface ($\omega_0 = 0.6$) where the ratio is nearly insensitive to the CTP for COT less than ~ 3.0 . As already demonstrated in the past, the impact of the surface reflectance on the signal is crucial. It has to be sampled in the LUT. In the following, unless explicitly stated, the surface will be Lambertian with an albedo of 0.1.

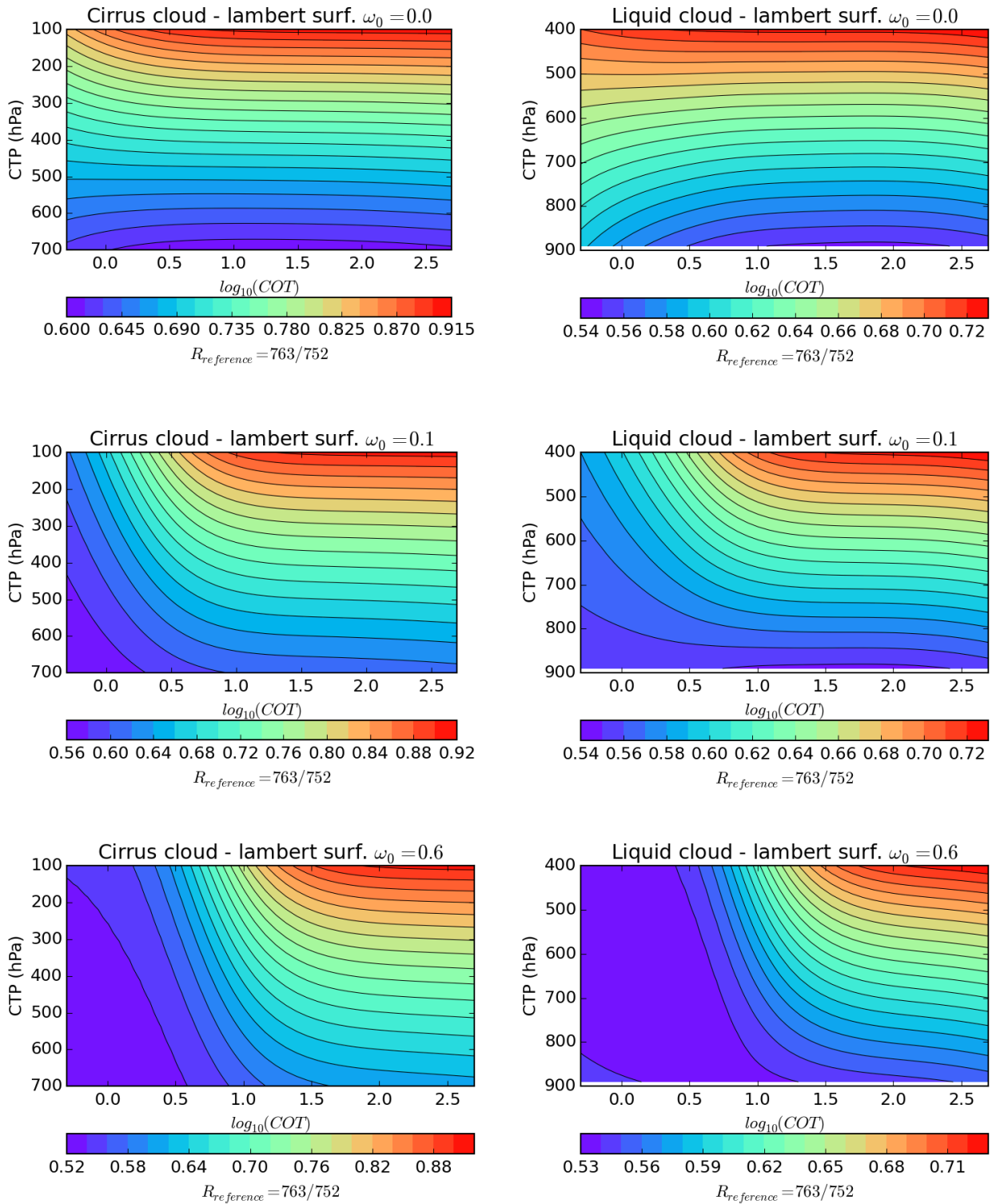


Figure 4.1.3: METimage 763/752 nm reflectance ratio as a function of the optical thickness and CTP for ice (right) and liquid clouds (left). Computation are done for a Lambertian surface of albedo 0.0 (higher panels), 0.1 (middle panels) and 0.6 (lower panels). The sun zenith angle is 30° and the observation is at nadir.

4.2 Sensitivity of the signal ratio and impact on CTP retrieval

To assess the sensitivity of $R = I_{763}/I_{752}$ to a given parameter, we vary the parameter and we measure the impact ΔR as a function of COT and CTP. For any (COT, CTP) couple, ΔR can be converted into an equivalent variation of CTP. ΔCTP is the CTP variation that would produce the same variation of R as the parameter change. This corresponds to a bias that will occur if fixing the given parameter for the retrieval.

4.2.1 Instrument noise

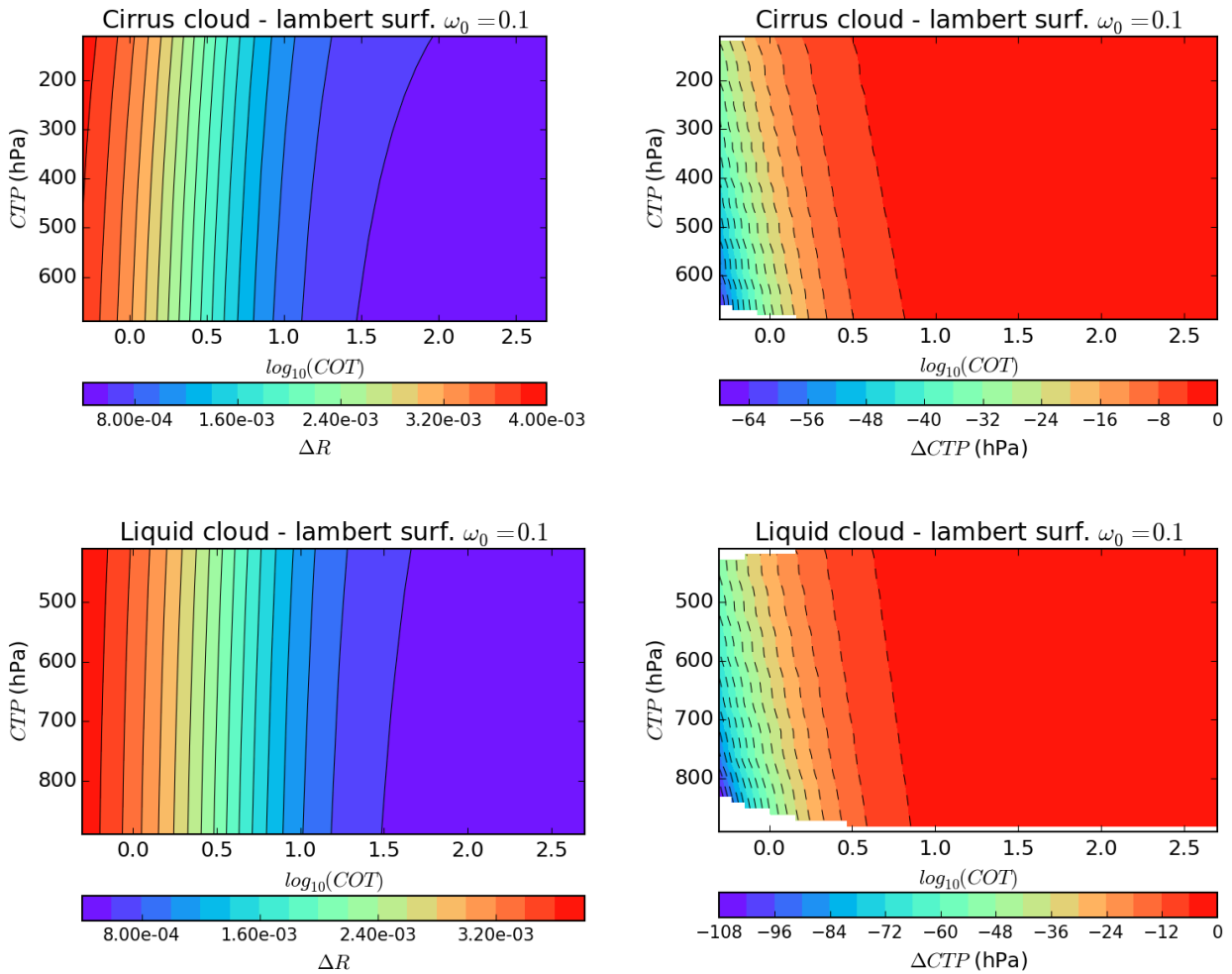


Figure 4.2.1 (Left) Variation of the 763/752 nm reflectance ratio corresponding to expected METimage noise level. (Right) Equivalent variation of CTP.

We compute the impact of noise on the signal ratio as $\Delta R = R_{high} - R_{low}$ with $R_{high} = \frac{I_{763} + \sigma_{763}}{I_{752} - \sigma_{752}}$ and

$R_{low} = \frac{I_{763} - \sigma_{763}}{I_{752} + \sigma_{752}}$. σ_{752} and σ_{763} is the noise level computed considering a signal to noise ratio of 420 for VII-5 and 480 for VII-4, at the typical measured radiance in each channel (28 and 20

$W m^{-2} sr^{-1} \mu m^{-1}$, see “EPS-SG System Requirements Document ” EUMETSAT [2013]). The impact on R decreases when increasing the opacity since the noise level will be less relatively less significant for higher reflectance. As seen on figure 4.2.1, the amplitude of the corresponding ΔCTP can be as high as $\sim 100hPa$ and $\sim 70hPa$ for the liquid and ice clouds respectively. The amplitude of ΔCTP increases with decreasing optical thickness and only slightly depends on the altitude.

This ΔCTP represents detection limits related to the instrument noise. It can then be seen as a reference for the relevance of signal sensitivity to other parameters (see annex section 8.1)

4.2.2 Cloud optical thickness

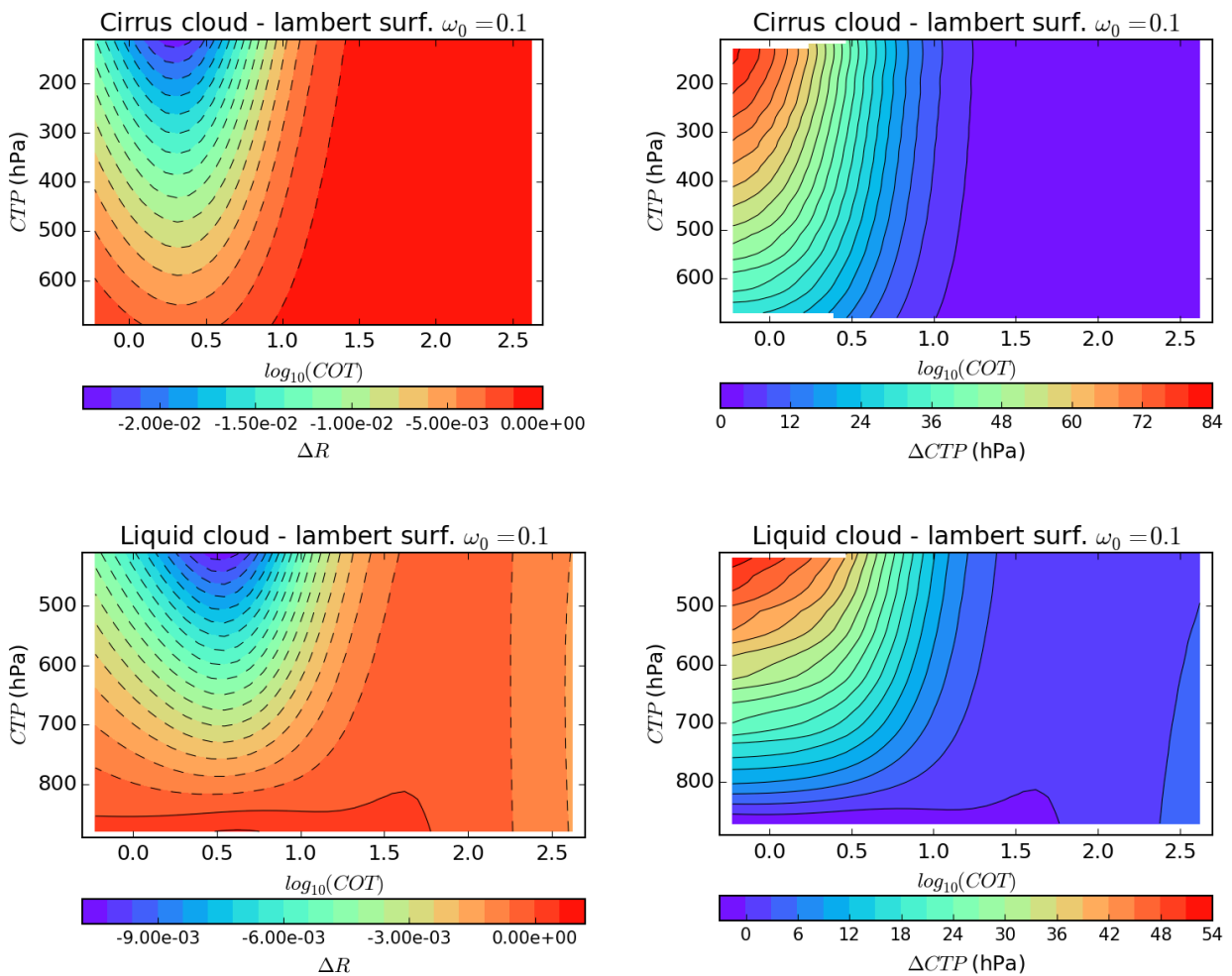


Figure 4.2.2 (Left) Variation of the 763/752 nm reflectance ratio due to a change of COT by $\pm 10\%$. (Right) Equivalent variation of CTP.

The COT is of prime importance for the retrieval as we saw with figure 4.1.3. It impacts the mean photon path-length by driving the fraction of photon that reaches the surface and the level of surface/cloud interaction. Its impact is then higher for brighter surfaces (see figure 4.1.3). We computed ΔR by varying the opacity by $\pm 10\%$ (see figure 4.2.2). At each point of the domain, we have $\Delta R = R_{cot \times 0.9} - R_{cot \times 1.1}$. To

decrease COT results in a decrease of R . This is mostly because the surface contribution is enhanced so that the mean photon path-length is lengthened. ΔR amplitude is peaked for highest altitude clouds with intermediate opacities (2 to 4) where the surface/cloud interaction may be enhanced while the difference between surface and cloud top pressure is high. It is slightly shifted toward thinner clouds for ice compare to liquid. ΔR is very small for opacities greater than ~ 20 . Regarding the equivalent CTP variation, its amplitude increases with increasing altitude and/or decreasing opacity. It reaches a value of ~ 55 hPa for liquid cloud (COT=0.5, CTP ~ 400 hPa) and ~ 85 hPa for ice cloud (COT=0.5, CTP ~ 150 hPa). ΔCTP is not significant for opacities greater than ~ 20 .

In section 4.3, we will do the same exercise but rather than applying a constant $\pm 10\%$ to the COT, we will have an equivalent $\Delta COT = f(COT)$ computed from the sensitivity of reflectances (i.e. the signal to constrain COT) to various parameters.

4.2.3 Cloud geometrical thickness

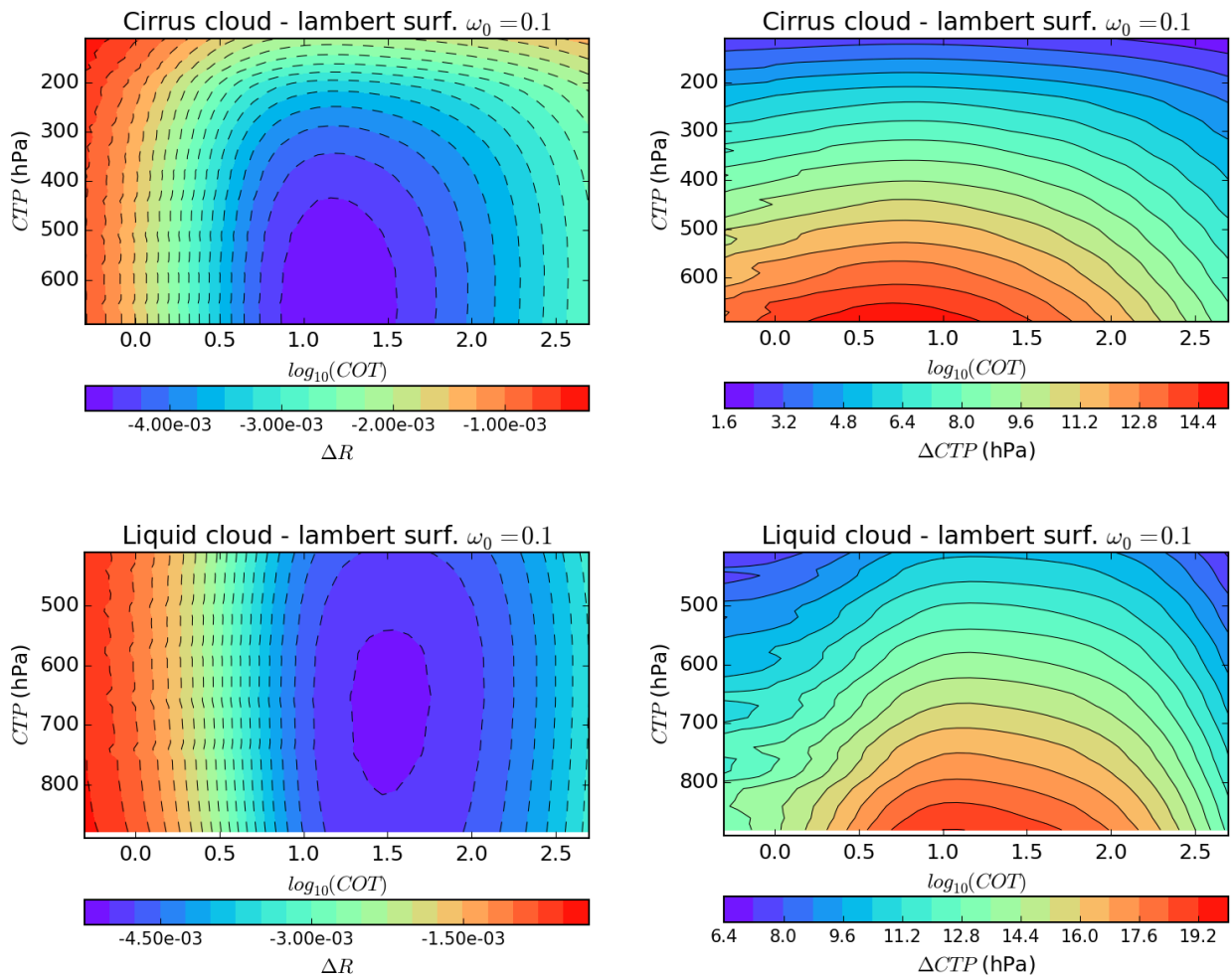


Figure 4.2.3 (Left) Variation of the 763/752 nm reflectance ratio due to a change of the CGT by $\pm 10\%$. (Right) Equivalent variation of CTP.

As already stated in other studies (see section 2), the cloud geometrical thickness impacts the photon penetration depth into the cloud and then its mean path-length. We computed $\Delta R = R_{CGT=1.1km} - R_{CGT=0.9km}$. As seen in figure 4.2.3, an

increase of the CGT leads to a decrease of R because the mean photon path-length increases. ΔR is maximum (in amplitude) for intermediate opacities (~ 10 to ~ 50) lower altitude clouds. The peak is shifted toward smaller opacities for ice clouds regarding liquid clouds. It is only slightly dependant on the altitude for lower liquid clouds. Its dependency on the altitude increases with altitude. Regarding the equivalent CTP variation, it is maximum for intermediate opacities (~ 2 to ~ 30). Again the peak is shifted toward smaller opacities for ice clouds regarding liquid clouds. Either for ice and liquid clouds, ΔCTP amplitude increases with decreasing altitude. For liquid clouds it ranges between ~ 7 hPa for $CTP=400$ hPa to ~ 19 hPa for $CTP=900$ hPa. For ice clouds, it varies between ~ 2 hPa at $CTP=100$ hPa to 14 hPa at $CTP=700$ hPa. Note that the same exercise with $CGT=3.0\text{km}\pm 10\%$ gives ΔCTP 2 to 3 times greater.

4.2.4 Cloud vertical profile

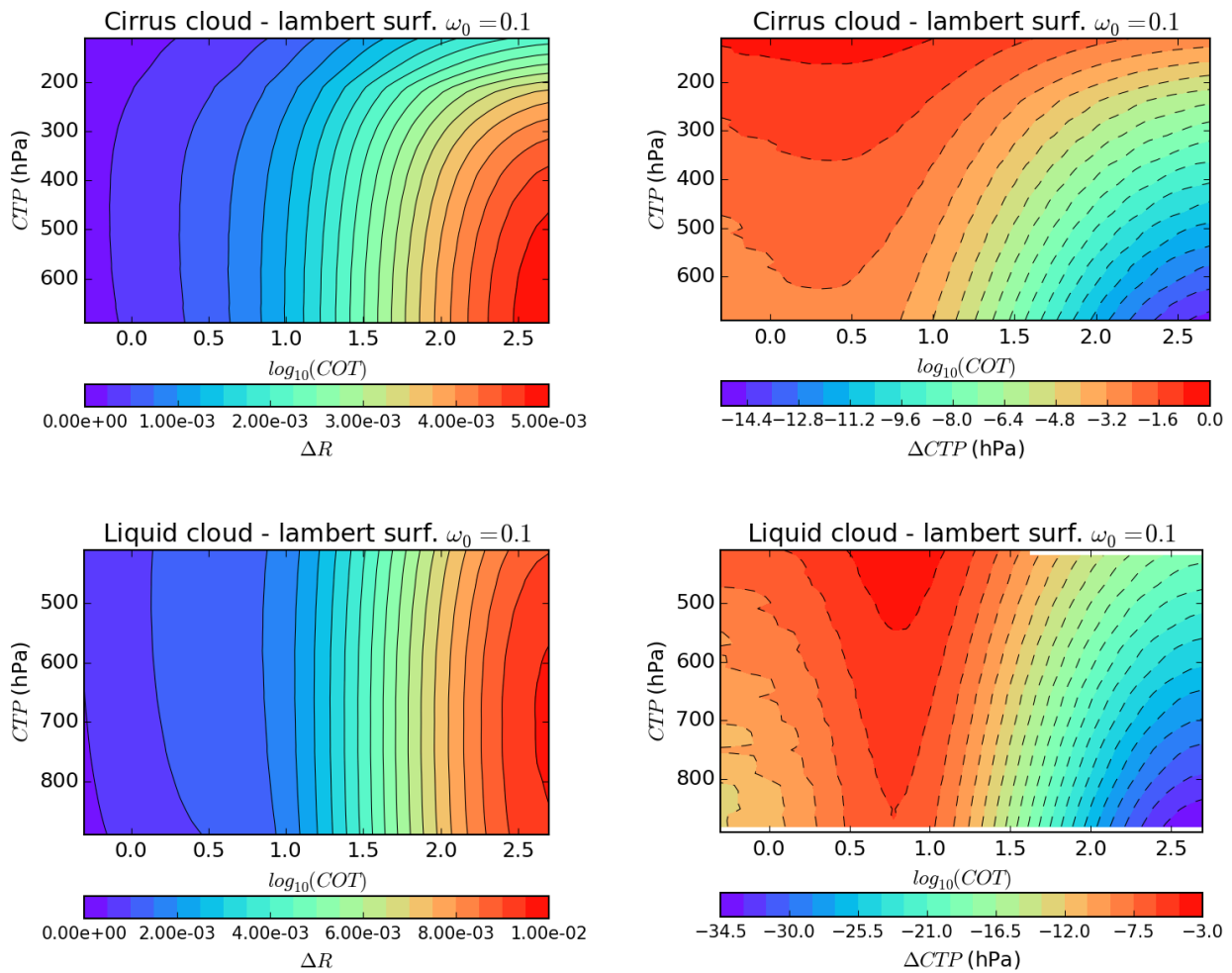


Figure 4.2.4 (Left) Variation of the 763/752 nm reflectance ratio due a change between a CPR profile (Cirrostratus and Stratocumulus) to a homogeneous profile. (Right) Equivalent variation of CTP.

Likewise the CGT, the cloud vertical profile drives the photon penetration depth into the cloud. We computed $\Delta R = R_{HOMO} - R_{CPR}$. As seen on figure 4.2.4, to go from a CPR to a homogeneous profile leads to an increase of R because the photon penetration depth into the cloud

is decreased, so is the photon path-length. ΔR increases as the opacity increases and/or altitude decreases. Indeed, for thin clouds we see the surface rather than the cloud anyway. For thick clouds, the increase of the

ΔR with decreasing altitude is related to the exponential decrease of the pressure so that a given increase of the photon path-length into the cloud leads to a higher increase of O₂ absorption at low altitude. Regarding the equivalent CTP variation, its amplitude essentially increases with increasing opacity and/or decreasing altitude for opacity greater than ~ 2 to ~ 5 where the minimum is. For liquid clouds, ΔCTP ranges from -3.0hPa for higher altitude thin clouds to -34hPa for low altitude thick clouds. For ice cloud, it is null for high altitude thin clouds and goes down to -15hPa for low altitude thick clouds. To do the same exercise with a cloud of CGT=3.0km leads to ΔCTP roughly 2 times greater.

4.2.5 Ice particle model

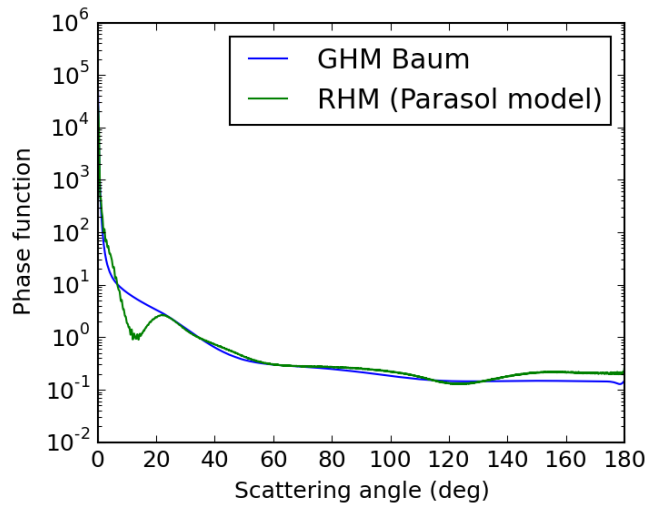


Figure 4.2.5 Phase function for General Habit Mixture model from Baum et al. [2014] and Rough Hexagonal Mono-crystal (POLDER/PARASOL like model). The effective radius is 25 microns.

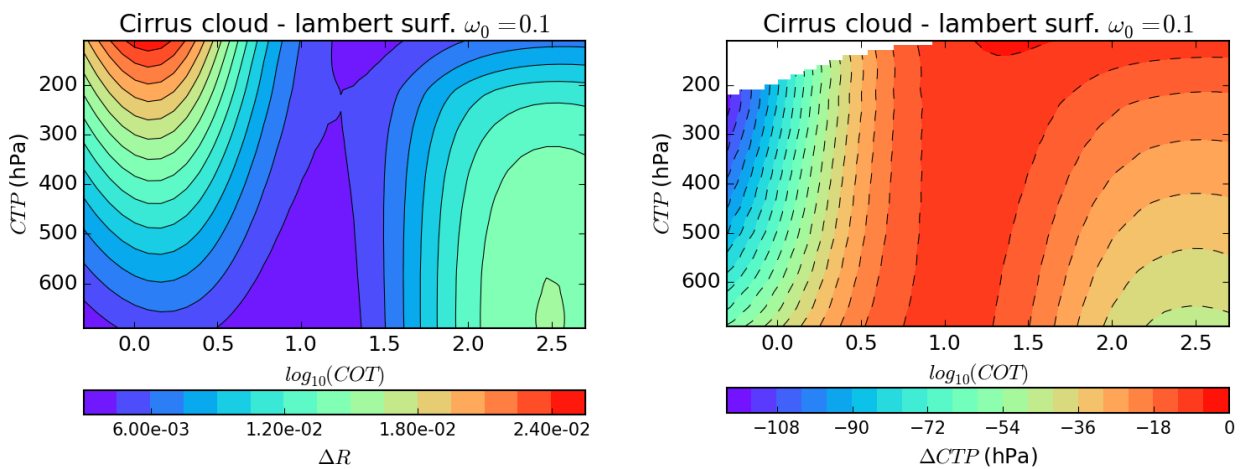


Figure 4.2.6 (Left) Variation of the 763/752 nm reflectance ratio due a change of ice particle model (see figure 4.2.5). (Right) Equivalent variation of CTP.

The ice particle model impacts the photon penetration depth through the phase function shape (i.e. asymmetry factor). We compute ΔR by varying the ice particle model from the General Habit Mixture (GHM) of Baum et al. [2014] to the Rough Hexagonal Mono-crystal (RHM, POLDER/PARASOL like model). Figure 4.2.5 shows the phase function for those two models. We have $\Delta R = R_{RHM} - R_{GHM}$. As seen on figure 4.2.6, to go from the GHM to the RHM model leads to an increase of the ratio. The photon penetrates less into the cloud with the RHM particles ($g=0.77$) than with the GHM particles ($g=0.80$). ΔR amplitude is peaked for high altitude clouds with $COT \sim 1.0$ and low altitude clouds with $COT \sim 300$. It is minimum for $COT \sim 10-15$. The equivalent CTP change is maximum for high altitude thinner clouds with an amplitude of ~ 120 hPa. It also reaches a significant value of ~ 45 hPa for low altitude thicker clouds.

4.2.6 Particle effective radius

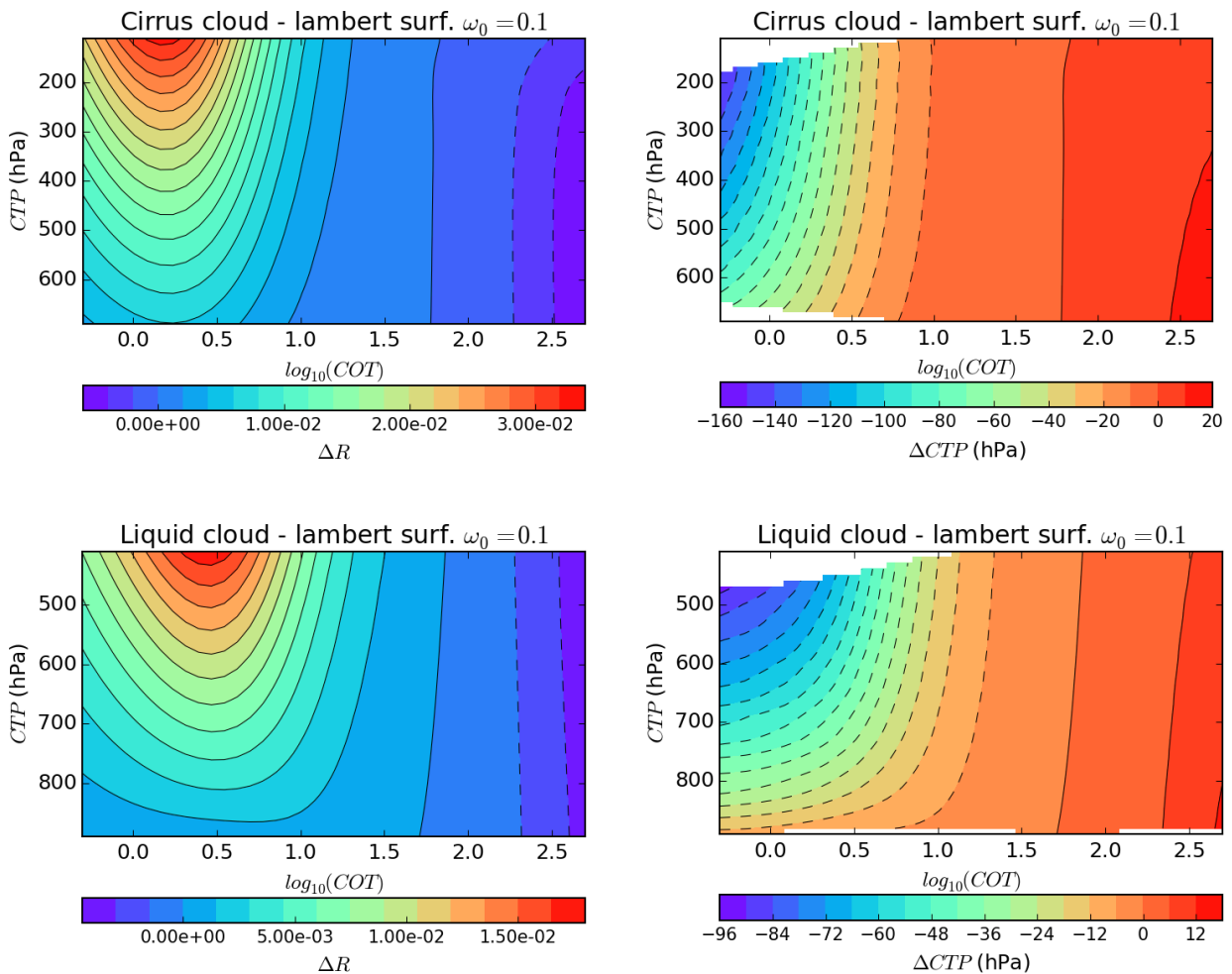


Figure 4.2.7 (Left) Variation of the 763/752 nm reflectance ratio due a change of particle effective radius between 5 and 30 (60) microns for Liquid (ice) cloud. (Right) Equivalent variation of CTP. White areas are produced where CTP corresponding to a given R is out of the modelled domain.

In that wavelength range cloud particles are almost purely scattering and the particle size essentially plays on the phase matrix. A big particle will scatter forward more than a small one. We computed ΔR by varying the effective radius of particles between 5 and 30 (60) microns for liquid (ice) clouds. We have $\Delta R = R_{r_{eff} min} - R_{r_{eff} max}$. As seen on figure 4.2.7, to decrease the effective radius results in an increase of R

for cloud with COT smaller than ~50-60. In that regime, a bigger particle will let photons go through the cloud more easily and the path-length will be larger. Moreover, ΔR increases with altitude because the pressure difference between the top of cloud and surface is increased. The effect is enhanced for intermediate opacity (~2) for which cloud surface interaction may be maximum. For clouds with opacity greater than ~50-60 a decrease of the effective radius results in a decrease of R . A tentative explanation is that photons that encountered a large number of scattering in the cloud (so with the largest path-length) will start to suffer from cloud absorption that is higher for bigger particle. Regarding the equivalent CTP variation it also changes of sign for opacities of ~50-60. For COT<50-60, the amplitude of ΔCTP is maximum for thin clouds at high altitude (-100hPa for liquid clouds, -160hPa for ice cloud). For a liquid cloud at 500hPa and with an opacity of 20 (like the study case of Preusker and Lindstrot [2009]), ΔCTP is ~-6hPa. Note that we consider a wider variability of the effective radius here. As shown by Preusker and Lindstrot [2009] the effective radius impact depends strongly on the geometry.

4.2.7 Presence of aerosols

4.2.7.a Continental average

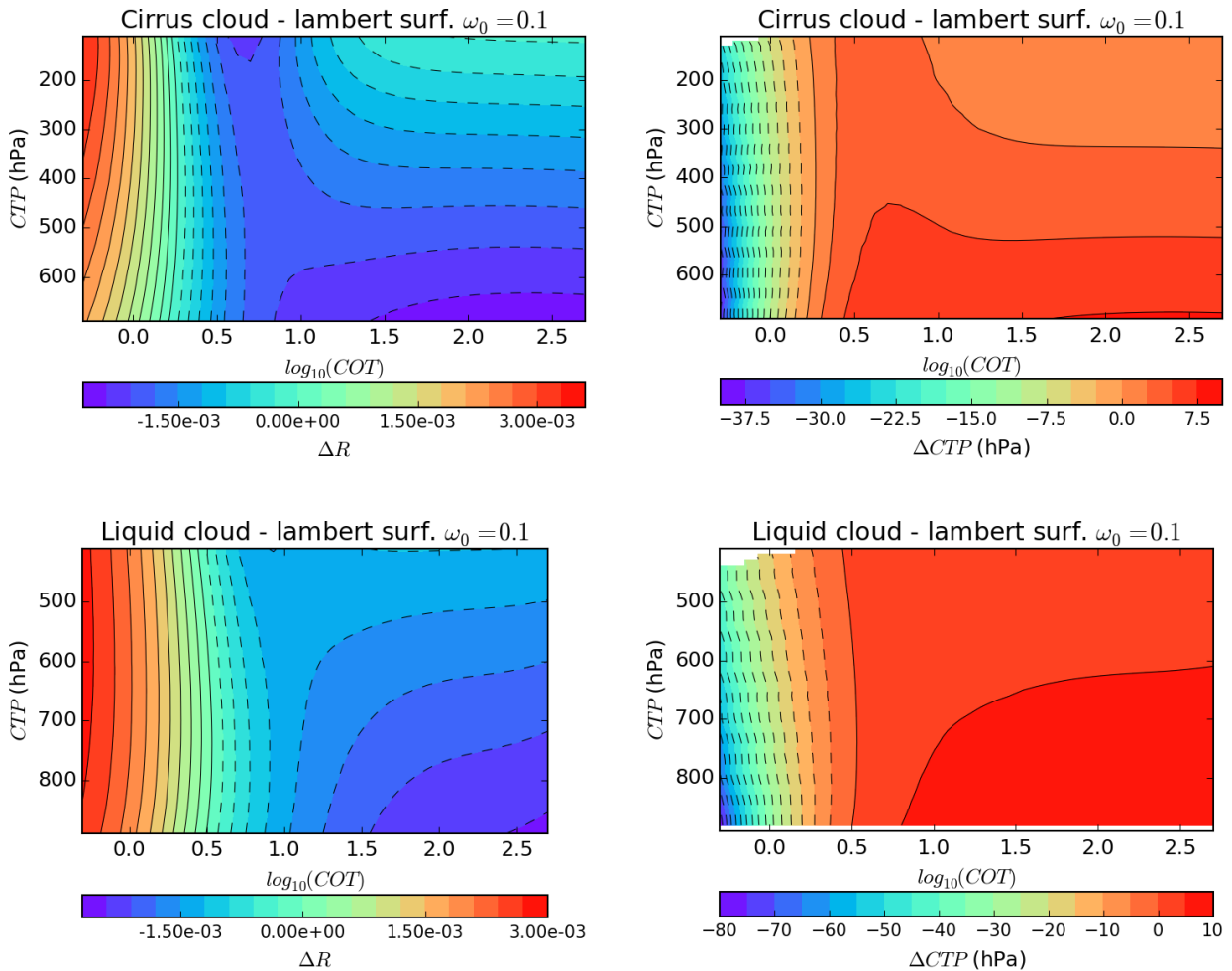


Figure 4.2.8 (Left) Variation of the 763/752 nm reflectance ratio due to the presence of a continental average aerosol ($H=8km, \tau=0.1$). (Right) Equivalent variation of CTP.

The presence of aerosols in cloudy atmosphere can either add more scattering or also continuum absorption.

Here, we compute ΔR by adding an aerosol of type continental average [Hess et al. 1998]. This aerosol has a scale height of 8 km (about the same as Rayleigh scattering) and an opacity of 0.1. We have $\Delta R = R_{with\ AER} - R_{without\ AER}$. As seen on figure 4.2.8, to add this aerosol results in an increase of R for $COT < 2-3$. In that regime and up to $COT \sim 4-8$, ΔR mostly decreases for increasing COT and does not depend much on altitude. For $COT > 4-8$, there is a transition to a regime where ΔR mostly depends on the altitude. For thin clouds, the aerosol will add to the atmosphere scattering opacity and may then reduce the mean photon path-length by screening the surface. The impact of this aerosol is complicated. Because of its scale height and because it is absorbing, the cloud/aerosol/surface interactions is quite complex. Regarding the equivalent CTP variation, its amplitude increases with decreasing opacity. At $COT=0.5$, it reaches ~ 80 hPa for liquid cloud and ~ 38 hPa for ice cloud. For opacities greater than 2-3, ΔCTP amplitude is smaller than ~ 10 hPa for both liquid and ice clouds.

4.2.7.b Maritime clean

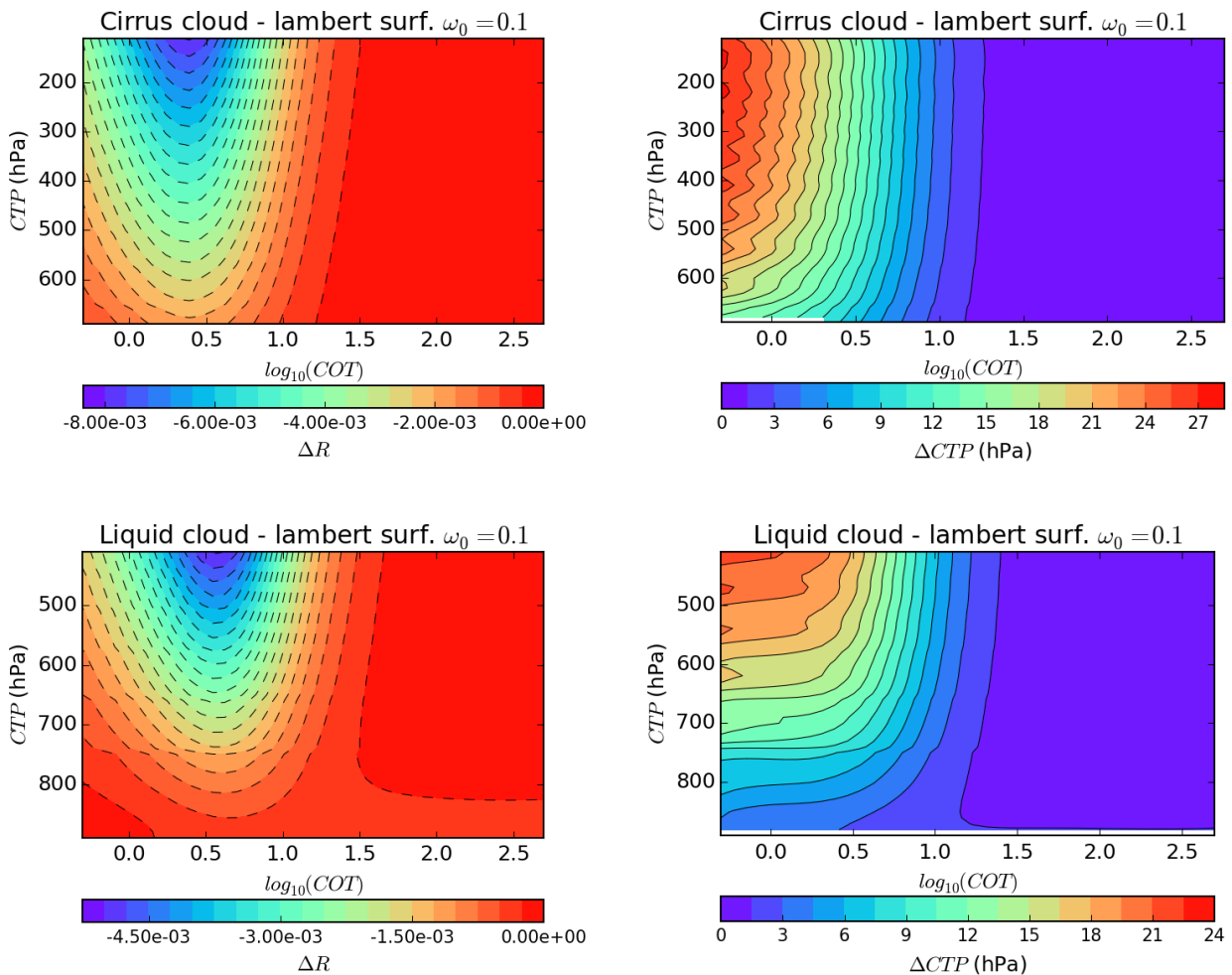


Figure 4.2.9 (Left) Variation of the 763/752 nm reflectance ratio due to the presence of a maritime clean aerosol ($H=1\text{km}$, $\tau=0.1$). (Right) Equivalent variation of CTP.

We compute ΔR by adding an aerosol of type maritime clean [Hess et al. 1998]. This aerosol has a scale height of 1 km and an opacity of 0.1 and is almost purely scattering. We have $\Delta R = R_{with\ AER} - R_{without\ AER}$.

To add this aerosol results in a decrease of R . The impact of this aerosol is very similar to the one resulting from a decrease of optical thickness or an increasing the surface albedo: it is an enhanced contribution of photons that reaches the surface (or near the surface for the present aerosol) compare to those scattered by the cloud. It corresponds to an increase of the photon mean path-length. ΔR amplitude is peaked for high altitude clouds (maximum difference of pressure between top of the cloud and the aerosol level) of intermediate opacity (2 to 4, maximum aerosol / cloud interaction). Again the peak is slightly shifted toward thinner clouds for the ice cloud. ΔR is very small for opacities greater that 15-20. Regarding the equivalent CTP variation, it increases with increasing altitude and/or decreasing opacity. It reaches a maximum value of ~ 24 hPa for liquid clouds and ~ 30 hPa for ice cloud. For opacities greater than ~ 15 , ΔCTP is not significant.

4.2.8 Surface pressure

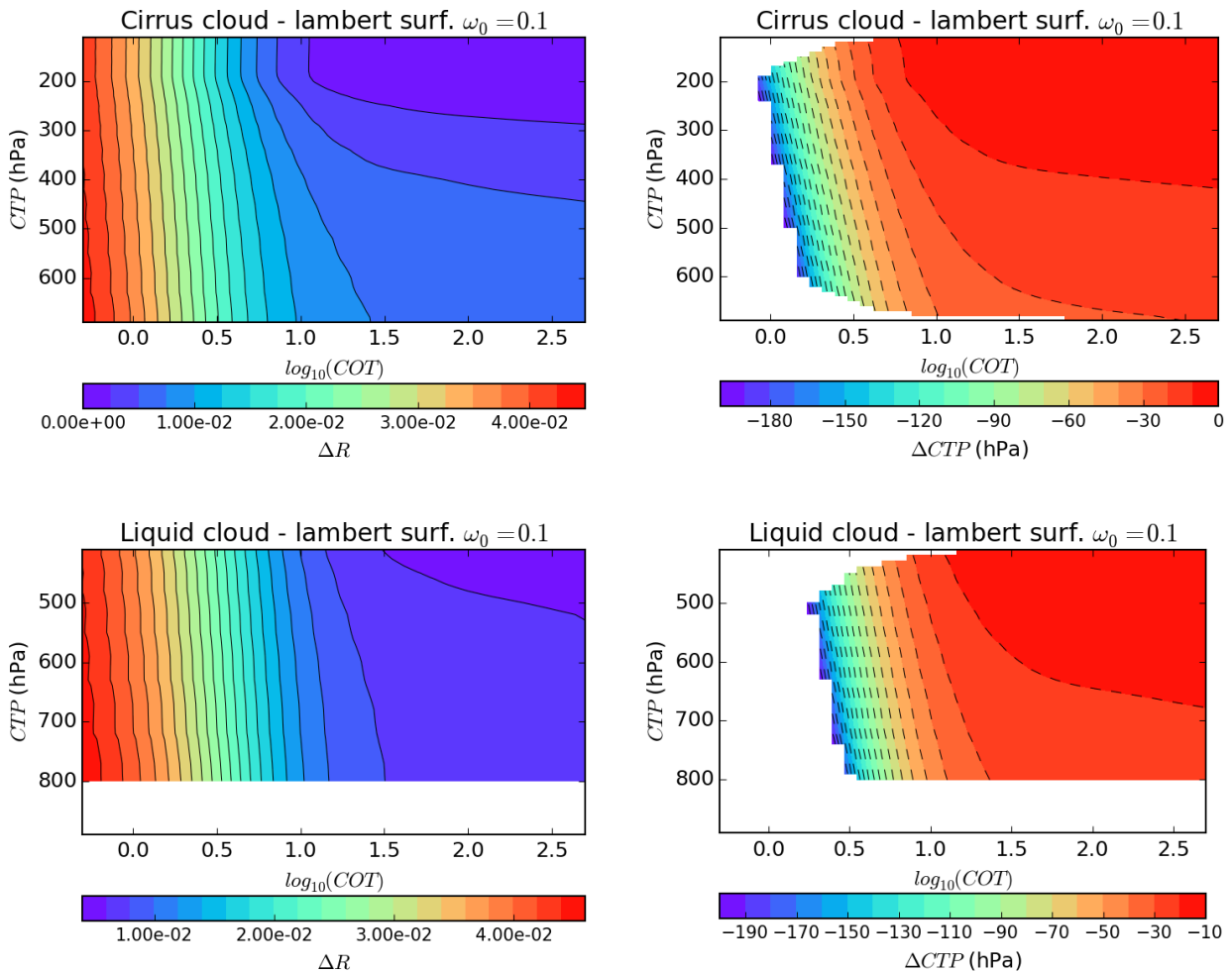


Figure 4.2.10 (Left) Variation of the 763/752 nm reflectance ratio due to a change of $\pm 10\%$ of the surface pressure (Right) Equivalent variation of CTP. The value >200 hPa are out of the domain (white areas).

The surface pressure can vary due to meteorological evolution and depending on the altitude of the surface. This drives the impact of photons that reach the surface. We compute ΔR by varying the surface pressure

by $\pm 10\%$ regarding the 1013hPa value. We have $\Delta R = R_{911.7\text{hPa}} - R_{1114.3\text{hPa}}$. We note that the atmospheric pressure of 1114.3hPa is not realistic for Earth atmosphere and only relevant for the sensitivity study. As seen on figure 4.2.10, a decrease of the surface pressure leads to an increase of R. ΔR increases with decreasing opacity. There is only a slight dependency on altitude, better seen on thicker clouds (due to the weakening of COT dependency). This poor dependency of the effect to the altitude may be related to the fact (i) that the same fraction of photons reaches the surface (the mean photon path-length is unchanged) and they are simply more affected by O₂ absorption and (ii) that there is no effect on photons that does not reach the surface. The equivalent CTP variation amplitude increases with decreasing opacity. For low opacities, ΔCTP is huge because the signal is not sensitive to CTP. As a consequence white areas are produced where the CTP corresponding to a given ratio is out of the modelled domain. Areas with $\Delta CTP < -200\text{hPa}$ where also masked for the colour bar dynamical range to be representative for lower value. For these areas in white, the CTP retrieval would be ruined by the corresponding bias. ΔCTP amplitude is smaller than $\sim 20\text{hPa}$ for cloud opacities greater than ~ 25 .

We must note that ΔCTP amplitude would be greater with a brighter surface.

4.2.9 ISRF wings

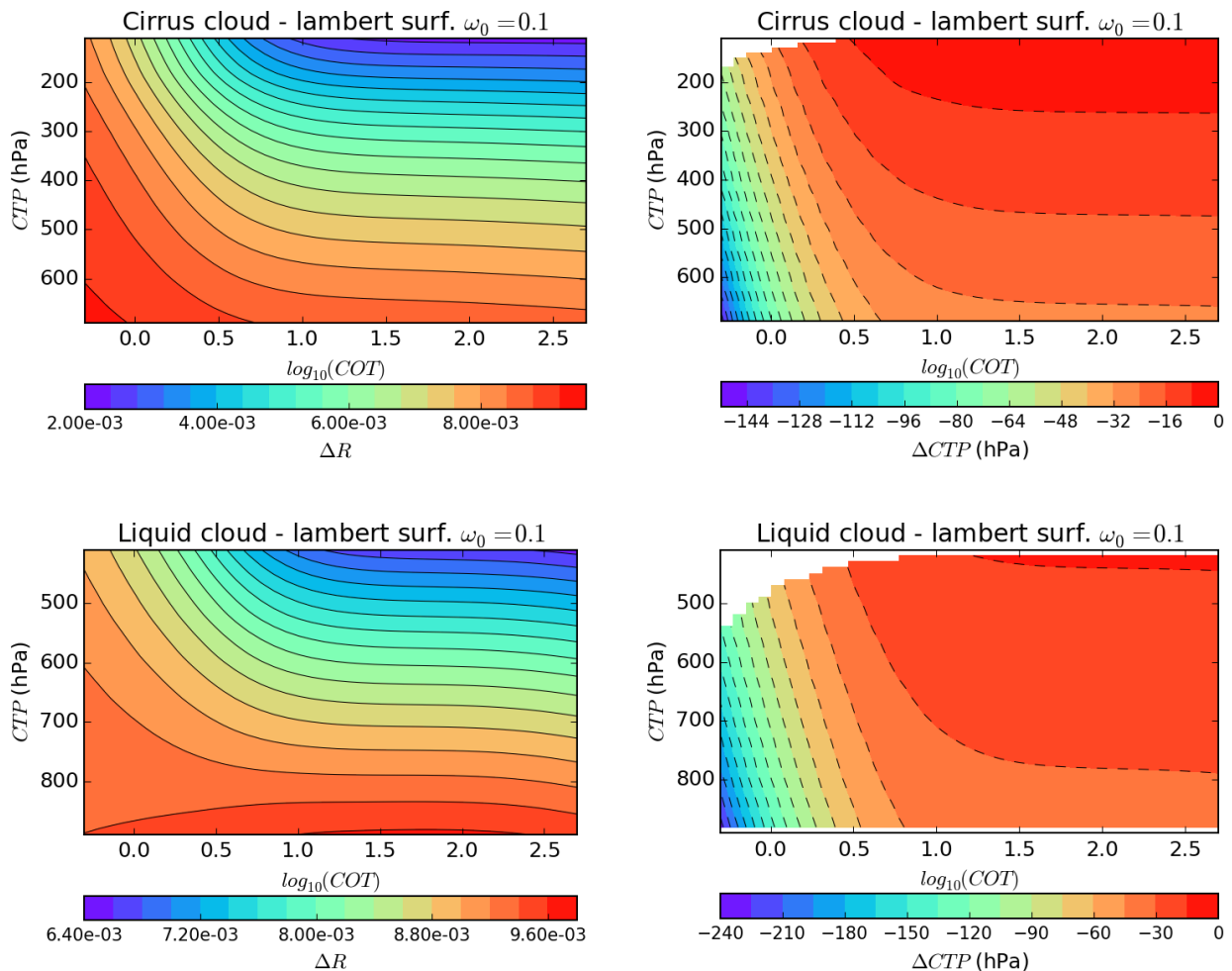


Figure 4.2.11 (Left) Variation of the 763/752 nm reflectance ratio due to a variation of energy in the 763 nm ISRF wings from 1% to 5%. (Right) Equivalent variation of CTP.

The ISRF used for the VII-5 channels is represented in figure 4.1.1. A variation of the fraction of energy falling into the wings will modify the corresponding O₂ transmission seen in the ISRF. Larger wings results in higher transmission since the wings are rather outside the O₂ A-band. ΔR is computed by varying the fraction of energy in the wing from 1% to 5%. We have $\Delta R = R_{5\%wings} - R_{1\%wings}$. As seen on figure 4.2.11, to increase the wings fraction leads to an increase of R. As stated above this is because the signal falling into the ISRF is then relatively less affected by the O₂ absorption. ΔR increases with decreasing opacity and/or decreasing altitude. It actually varies as the contrast between the reflectance in the O₂ absorption band and the one outside the absorption band (like R). Regarding the equivalent CTP variation, its amplitude increases with decreasing altitude and/or opacity. It reaches values of -240hPa for liquid cloud with COT=0.5 and CTP=900hPa and \sim -152hPa for ice clouds with COT=0.5 and CTP =700 hPa. For clouds with opacities >20-30 ΔCTP amplitude is less than \sim 30hPa.

4.2.10 Surface directionality

Bidirectional Anisotropy Standard shape (BASE)			
Biome	k_1/k_0	k_2/k_0	Mean k_0 for the biome
Grasses and cereal crops	0.1112	1.2709	0.1583
Shrubs	0.1945	0.5837	0.1627
Broad-leaf crops	0.0840	1.5642	0.1152
Savannah	0.1800	1.1699	0.0782
Broad-leaf forests	0.1503	2.8778	0.0311
Needle-leaf forests	0.1444	2.0585	0.0501
Deserts	0.0724	0.8977	0.2584

Table 2: 670 nm Li-Ross model directional parameters for various biomes as derived by Bacour and Bréon [2005]. Note that k_0 , k_1 , and k_2 , are usually referred to as isotropic, geometric and volumetric terms. The mean k_0 was obtained over the pixels used to derived the parametrization for each biome (several hundreds). It shows the typical level of reflectance expected for a given biome.

The mechanism that causes a bias due to BRDF miss-representation is the same as the one for a bad constraints of the Lambertian surface albedo, except it strongly depends on direction. In that section we look for effect related to the directionality of the surface reflection. We still show ΔR and ΔCTP variability in a 2 dimensions space but with (COT, view zenith angle) parameters. We then fix CTP to 400hPa and 800hPa for ice and liquid clouds, respectively.

For the ocean, the model use is the one described in section 3.4. We will vary the wind speed that drives the directionality of the ocean BRDF (see figure 4.2.12).

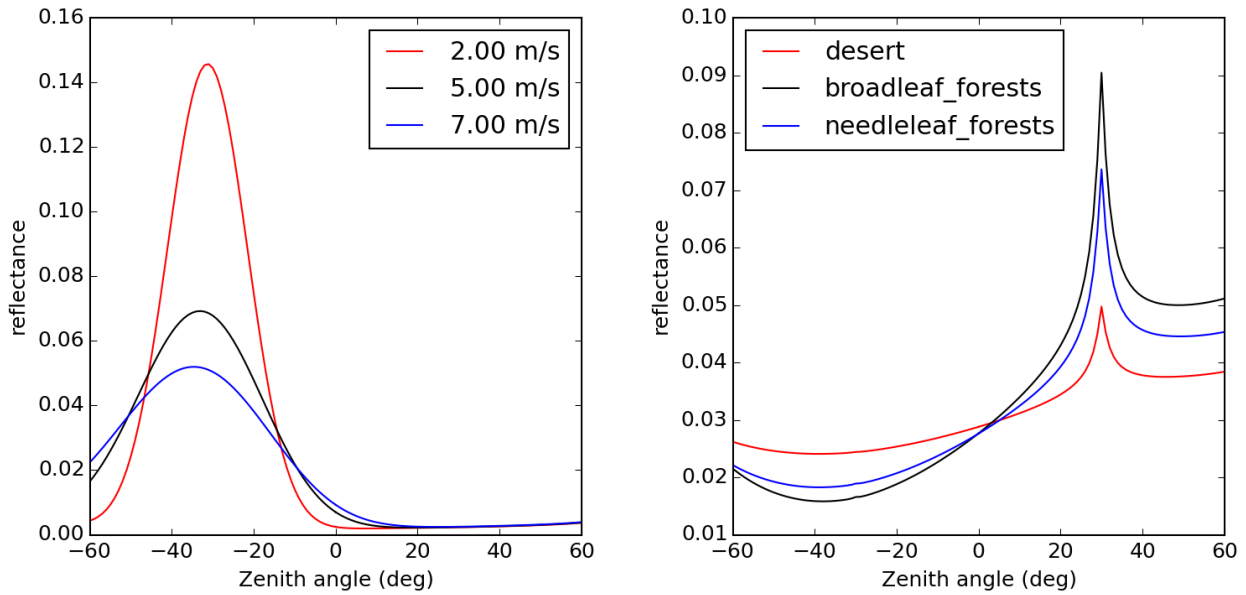


Figure 4.2.12: **(left)** 865nm reflectance at TOA for the ocean with various wind speed as a function of the view zenith angle in the solar plane. **(right)** 670 nm reflectance at TOA for various land surface type model with a Li-Ross model with hot-spot following the parametrisation of Bacour and Bréon [2005]. k_0 is set to 0.1. For both the land and ocean cases, the sun zenith angle is 30.0° .

Earth land-surfaces (except ice and snow) are found to exhibit similar bidirectional reflectance features that translate in magnitude depending on the leaf and soil optical properties [Bacour & Bréon 2005]. The Li-Ross model with a hot-spot [Maignan et al. 2004] is appropriate to model these. For purpose of normalizing bidirectional effect of land surface in operational satellite remote sensing, Bacour and Bréon [2005] derived the Bidirectional Anisotropy Standard shapes (BASEs) for various biomes using POLDER observations. The corresponding Li-Ross parameters are listed in table 2. The reflectance level of a BASE is adjustable with a single parameter k_0 (isotropic term). Bacour and Bréon [2005] concluded that although the variability of directional effects are important within a given biome, a fit of the directional effect on a pixel basis rather than the use of BASEs does not decrease significantly the error of normalization of those directional effects.

Snow and ice land surface are special cases. Their BRDF is significantly flatter than other land surface types [Kokhanovsky & Breon 2012]. We intend to use a Lambertian model in that case.

4.2.10.a Water surface

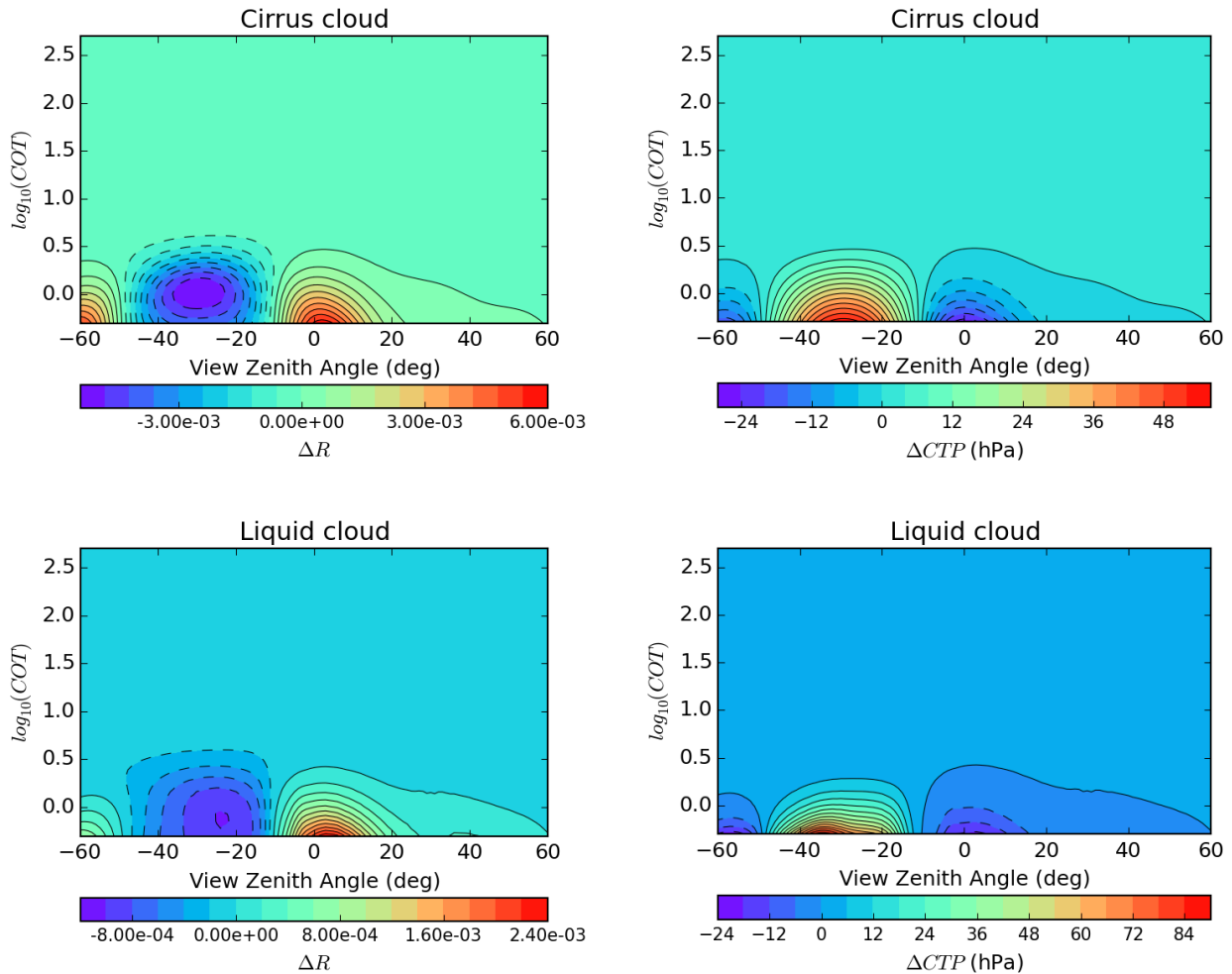


Figure 4.2.13 (Left) Variation of the 763/752 nm reflectance ratio over the ocean due to a variation of the wind speed of $\pm 10\%$ regarding 5m/s. (Right) Equivalent variation of CTP. The sun zenith angle is 30° . The observation is done in the principal plane.

A difference of wind-speed will result in different surface reflectance angular distribution. For a given geometry, it changes the fraction of the TOA reflectance related to the surface and thus the photon mean path-length. ΔR is computed by varying the wind speed by $\pm 10\%$ regarding 5m/s. We have $\Delta R = R_{4.5\text{m/s}} - R_{5.5\text{m/s}}$. As seen on figure 4.2.13, a decrease of the wind speed results in a decrease of R at glitter's peak and an increase of R in glitter's wings. This is due to the glitters spreading with increasing wind speed (see figure 4.2.12). As expected, the impact is rather located in the forward direction and for thinner clouds. The impact is negligible for COT greater than ~ 4 . Regarding the equivalent CTP variation, its amplitude is also greater in the forward direction and for thinner clouds. There also is a change of sign between the glitter's peak and wings. At glitter's peak for COT=0.5, it reaches values of ~ 85 hPa and 50hPa for liquid and ice clouds, respectively. In glitter's wings for COT=0.5, ΔCTP amplitude reaches values of ~ 25 hPa for liquid and ice clouds. ΔCTP is negligible for COT greater than $\sim 3-4$.

4.2.10.b Land surface

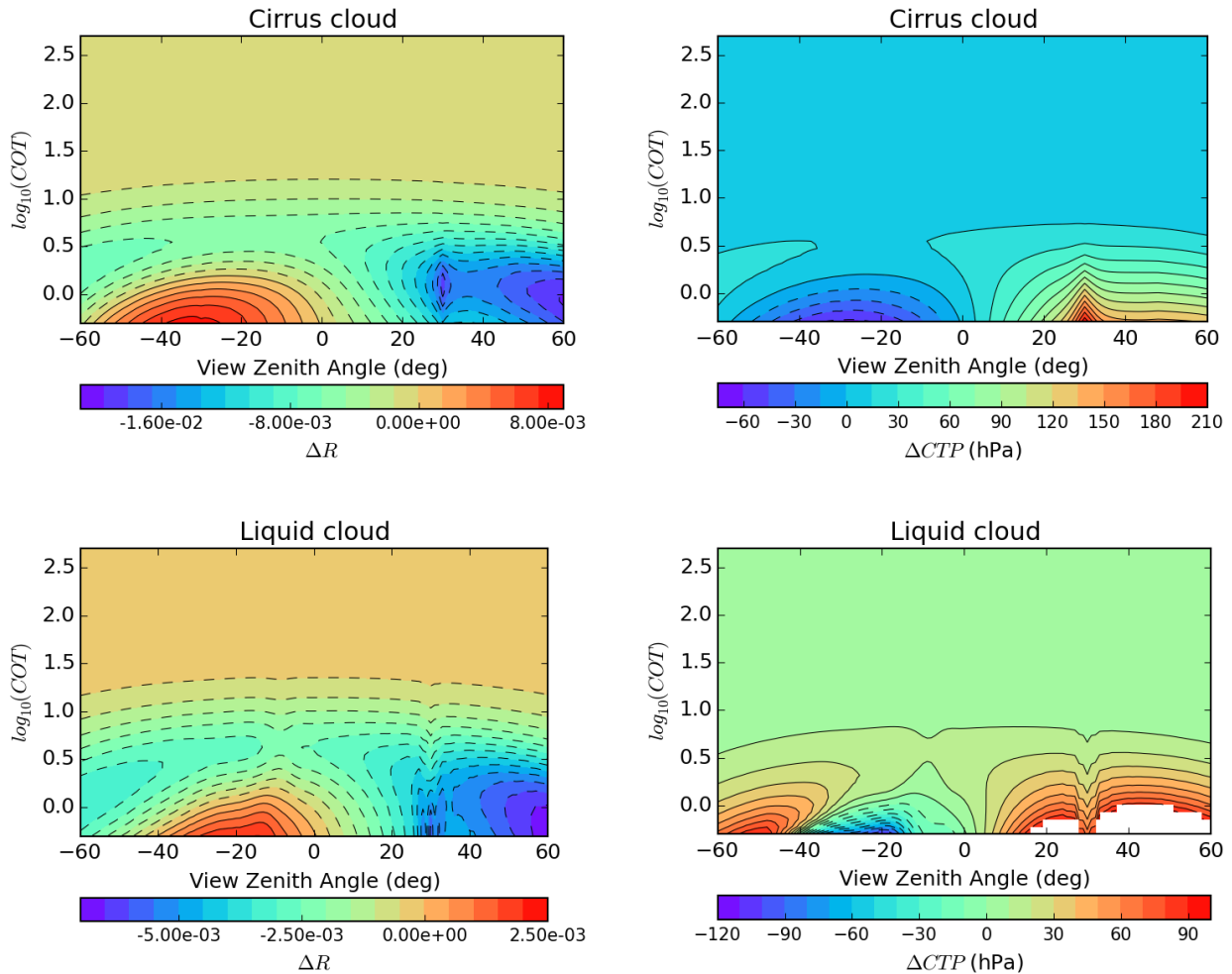


Figure 4.2.14 (**Left**) Variation of the 763/752 nm reflectance ratio due to changing from a desert BRDF to a broad-leaf forest BRDF. (**Right**) Equivalent variation of CTP. The sun zenith angle is 30°. The observation is done in the principal plane.

A different biome results in a difference BRDF. Here, the mechanism for R variation is the same as for the glitter case. ΔR is computed by going from a desert BRDF to a broad-leaf forest BRDF. k_0 is set to 0.1 for both. These BRDF are the most different among the land surface type (excluding ice and snow). These BRDF are shown figure 4.2.12. We have $\Delta R = R_{broadleaf} - R_{desert}$. As seen on figure 4.2.14 for thin clouds, to go from desert to broad-leaf forest BRDF results in an increase of R in forward direction and a decrease of R in the backward direction. Indeed, the surface reflectance is brighter in the forward direction for the desert which increases the photon mean path-length (through an increase of the TOA reflectance fraction related to the surface) and vice-versa for the backward direction. For clouds with COT greater than ~ 2 , R is systematically decreased for all directions. This is related to a change in white sky albedo between those land-surface at a given k_0 . Regarding the equivalent CTP variation, the white areas are produced where the CTP corresponding to a given ratio is out of the modelled domain or where the bias is > 200 hPa in amplitude. For these areas, the CTP retrieval would be ruined by the bias. ΔCTP sign also depends on the direction for thin clouds. Its amplitude drops to less than 15hPa for opacities greater than $\sim 5-6$.

4.3 Sensitivity of window channel reflectance and impact on the COT and CTP retrieval

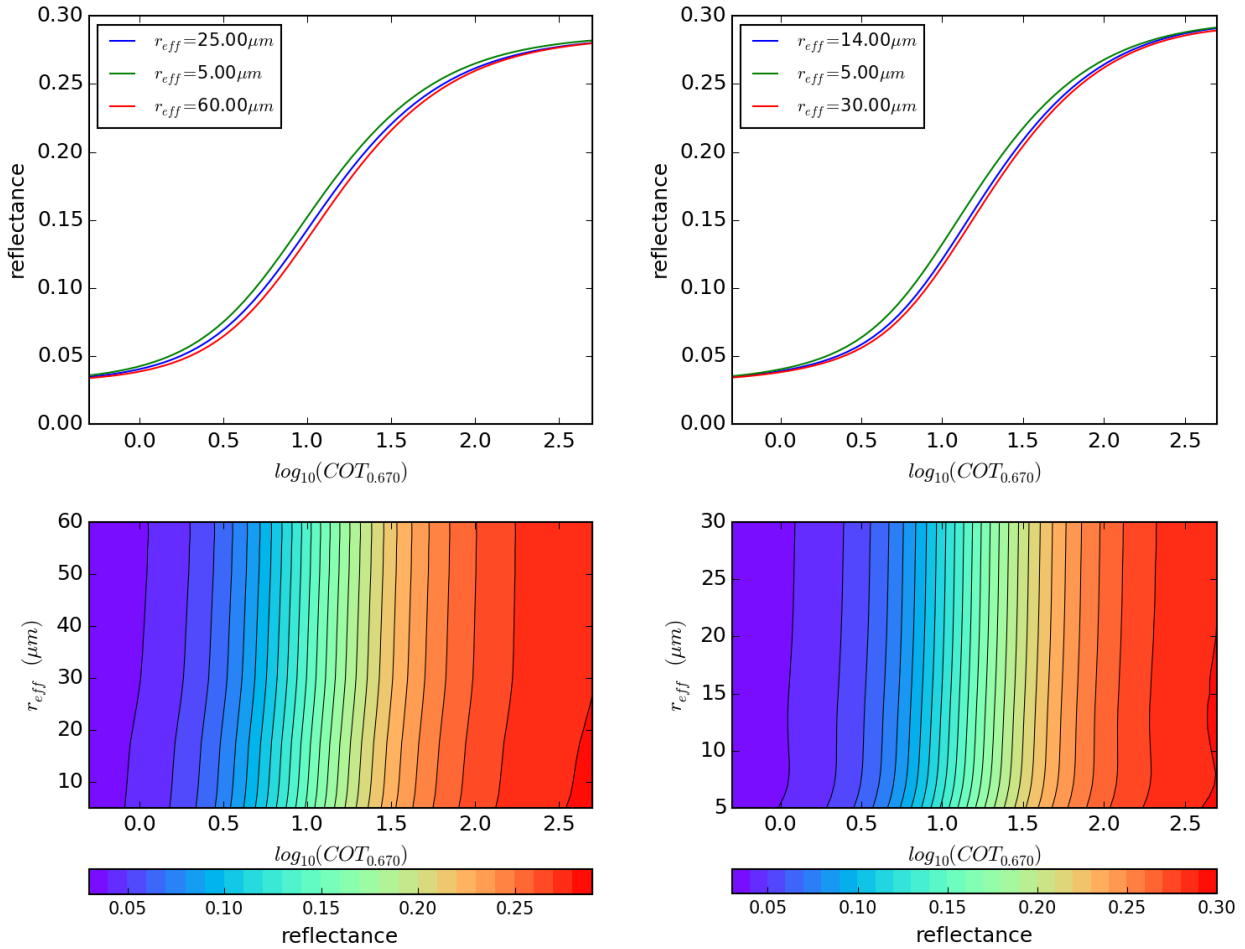


Figure 4.3.1 670 nm reflectance for a ice cloud (left) and liquid cloud (right) over a Lambertian surface with an albedo of 0.1.

In the foreseen algorithm, the COT will be retrieved jointly to the CTP. As we saw in section 4.2.2, an error on the COT leads to a bias of the retrieved CTP. In the present section, we study the sensitivity of the reflectance (either 670nm or 865nm) used to constrain COT, to various parameters. After varying those parameters, we measure the resulting ΔI as a function of COT. The ΔI can be converted to an equivalent variation of COT. ΔCOT is the COT variation that would produce the same variation of reflectance as the parameter change. This corresponds to a bias that will occur if fixing or having an uncertainty on the given parameter for the retrieval. On a second step, we can reproduce the exercise of section 4.2.2 but with the $\Delta COT = f(COT)$ corresponding to a bias in the COT retrieval. This represents a propagation of the COT bias to a bias in the final retrieved CTP.

The model used here is the same as the one described at section 4.1. Unless BRDF effect is studied, the surface is taken as Lambertian with an albedo of 0.1. Figure 4.3.1 shows the reflectance at 670 nm for ice

clouds (left) and liquid clouds (right) over a Lambertian surface with an albedo of 0.1 as a function of the effective radius and opacity. We see that the reflectance is essentially function of the opacity. The same conclusion holds for 865 nm. In the following, the effective radius is fixed to 14 and 25 microns for liquid and ice clouds respectively. The CTP has no impact on the reflectance at 670nm or 865nm that will be used to constrain the COT.

We note that as stated by Zeng et al. [2012], the sub-pixel inhomogeneities and shadowing effect as well as the broken cloud effect for glitter direction lead to important bias of the retrieved COT. To account for these effects is beyond the scope of the Day-A algorithm.

4.3.1 Ozone

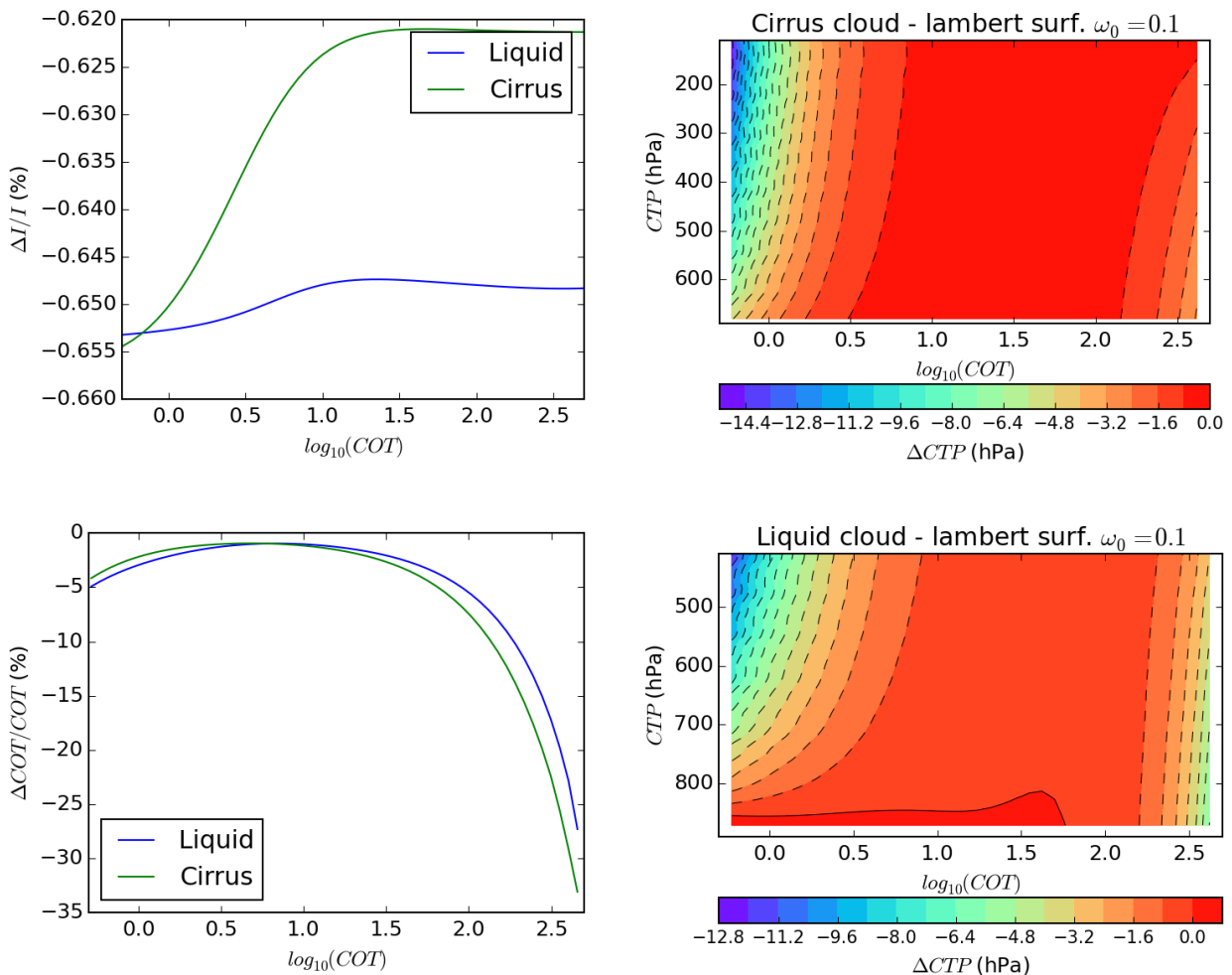


Figure 4.3.2 (**Upper left**) Relative variation of reflectance due to a variation of the Ozone column by $\pm 10\%$. (**lower left**) Equivalent relative variation of COT. (**Right**) Propagation of the COT variability to equivalent CTP variation.

The ozone absorption will directly impact the reflectance at 670nm. We compute ΔI by varying the ozone column by $\pm 10\%$ regarding the value for the AFGL US62 profile. We have $\Delta I = I_{+10\%} - I_{-10\%}$. As

expected, we see in figure 4.3.2 that an increase of the ozone column results in a decrease of the reflectance.

$\Delta I/I$ is almost constant to $\sim 0.6\%$ but slightly increases for thin clouds since we then see the surface. While $\Delta I/I$ is small, the equivalent COT variation is still high for thin and thick clouds where I is not very sensitive to COT. $\Delta COT/COT$ reaches an amplitude of $\sim 30\%$ for thick clouds. Regarding the propagation to ΔCTP , we use $\Delta R = R_{cot-\Delta cot/2} - R_{cot+\Delta cot/2}$. Like for a constant relative variation of COT (section 4.2.2) the ΔCTP amplitude is maximum for higher altitude low opacities. However, the low altitude, high opacity clouds are also affected up to $\sim 5\text{hPa}$ in amplitude.

Note that the ozone column can vary from 150 to 550 Dobson unit. The effect can then be important in term of the error on CTP. The exercise was performed at 670 nm. The effect will be almost negligible at 865 nm due to very low ozone absorption at that wavelength.

4.3.2 Ice particle model

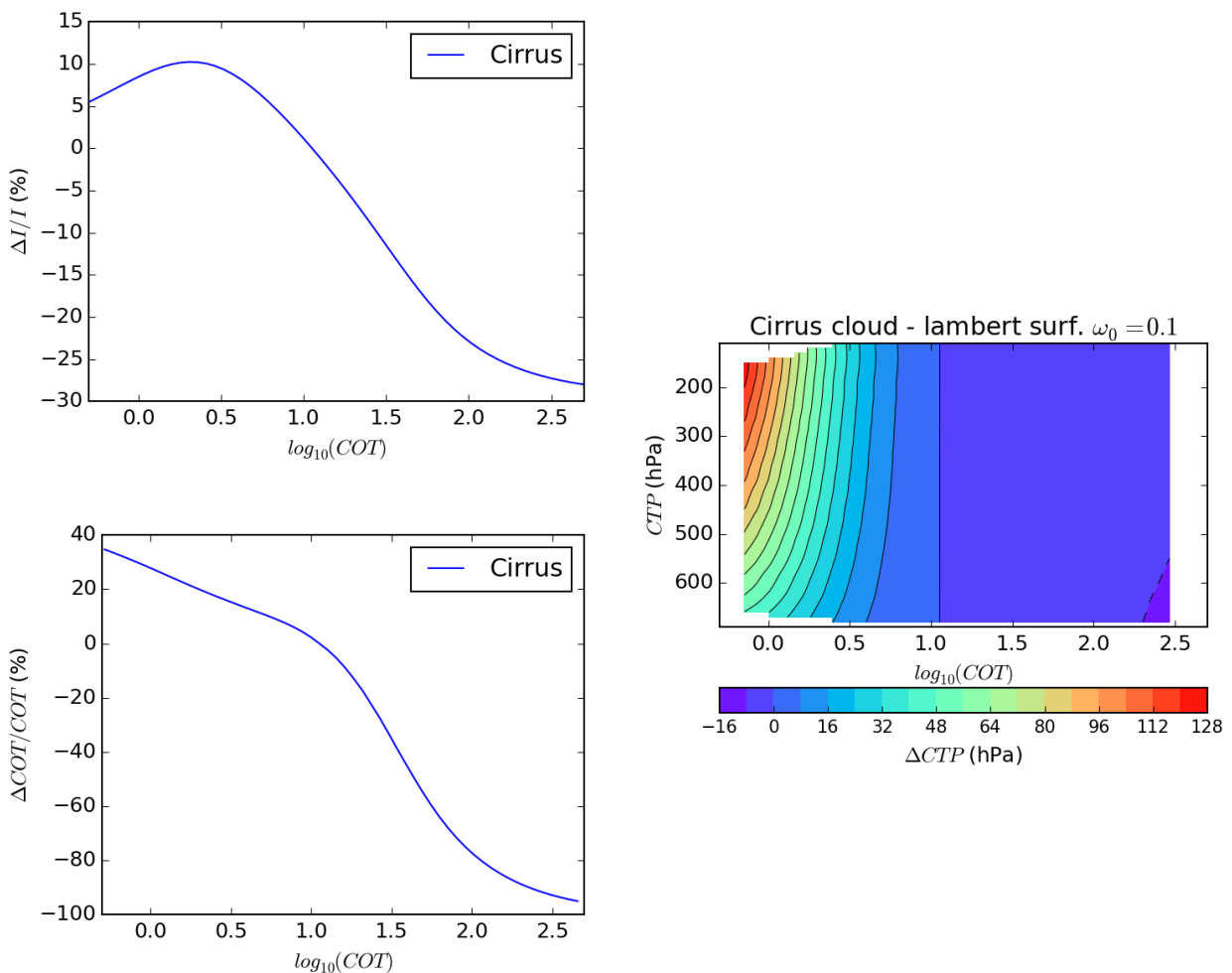


Figure 4.3.3 (**Upper left**) Relative variation of reflectance due a change of ice particle model (see figure 4.2.5) (**lower left**) Equivalent relative variation of COT. (**Right**) Propagation of the COT variability to equivalent CTP variation.

The ice particle model impacts the reflectance. We compute ΔI by varying the ice particle model from the General Habit Mixture (GHM) of Baum et al. [2014] to the Rough Hexagonal Mono-crystal (RHM,

Polder/Parasol like model). Figure 4.2.5 shows the phase function for those two models. We have $\Delta I = I_{RHM} - I_{GHM}$. As seen on figure 4.3.3, to go from the GHM to the RHM leads to an increase of the reflectance for COT smaller than ~ 10 and to a decrease of the reflectance for a greater COT. $\Delta I/I$ is equal to $\sim 10\%$ for COT ~ 3 and decreases down to $\sim 27\%$ for COT ~ 500 . The equivalent COT v also changes of sign around COT = 10. ΔCOT is equal to $\sim +35\%$ at COT=0.5 and decreases down to $\sim -95\%$ at COT=500. To compute ΔCTP , we use $\Delta R = R_{cot-\Delta cot/2} - R_{cot+\Delta cot/2}$. Like for a constant relative variation of COT (section 4.2.2) the ΔCTP amplitude is maximum for higher altitude low opacities. ΔCTP sign changes at COT ~ 10 . It is ~ -10 hPa for lower altitude thicker clouds.

4.3.3 Effective radius

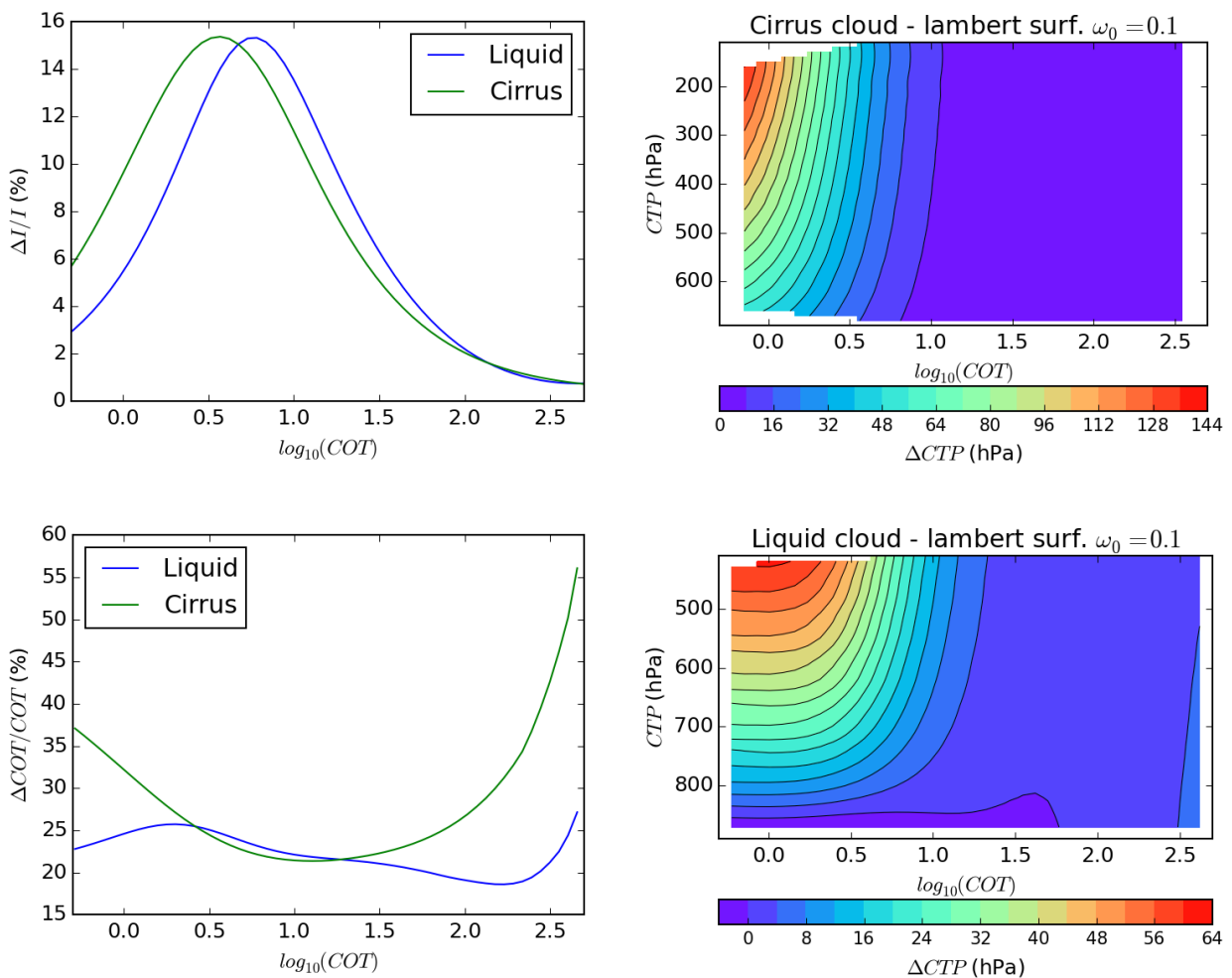


Figure 4.3.4 (**Upper left**) Relative variation of reflectance due to a change of particle effective radius between 5 and 30 (60) microns for Liquid (ice) cloud. (**lower left**) Equivalent relative variation of COT. (**Right**) Propagation of the COT variability to equivalent CTP variation.

As seen in figure 4.3.1 the effective radius moderately impacts the 670nm reflectance. We compute ΔI by varying the particle effective radius between 5 and 30 (60) microns for Liquid (ice) cloud. We have

$\Delta I = I_{r_{eff\ min}} - I_{r_{eff\ max}}$. As seen in figure 4.3.4, to decrease the effective radius results in an increase of the reflectance. $\Delta I/I$ is peaked for intermediate opacities. However, the amplitude of the COT equivalent variation remains greater for low and high opacities regarding intermediate opacities. This is again because I is not very sensitive to COT for thin and thick clouds. Regarding the propagation to ΔCTP , we use $\Delta R = R_{cot-\Delta cot/2} - R_{cot+\Delta cot/2}$. Like for a constant relative variation of COT (section 4.2.2) the ΔCTP amplitude is maximum for higher altitude low opacities. ΔCTP amplitude is smaller than 8hPa for COT greater than ~ 10 . The impact of effective radius variation may strongly depend on the geometry.

Note that at 865 nm, ΔI and ΔCOT is greater than at 670nm for optically thick clouds. However, for high opacities, the R is almost independent of COT. ΔCTP amplitude remains smaller 15hPa for COT greater than 10.

4.3.4 Aerosols

4.3.4.a Continental average

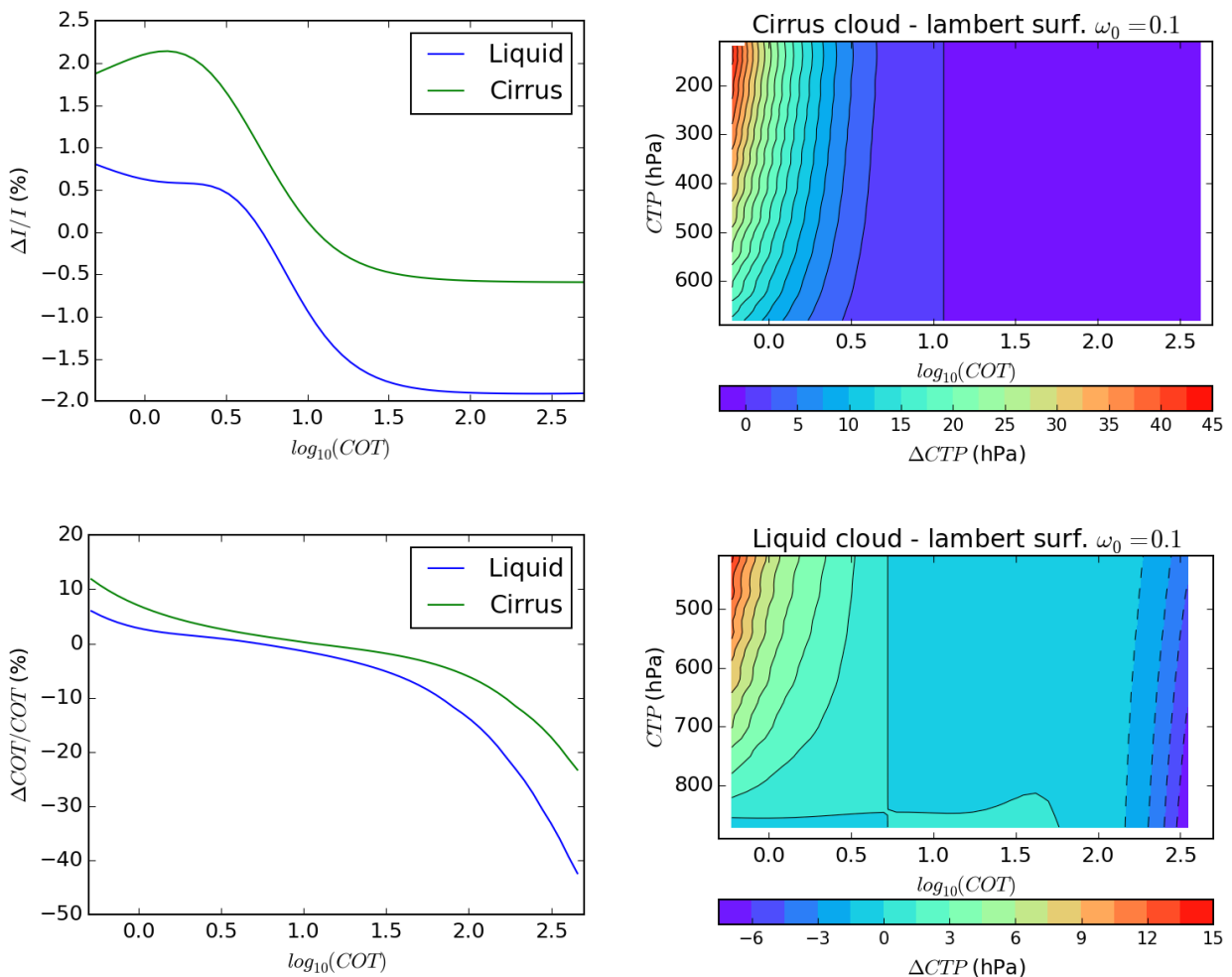


Figure 4.3.5 (Upper left) Relative variation of reflectance due to the presence of a continental average aerosol ($H=8km, \tau=0.1$). (lower left) Equivalent relative variation of COT. (Right) Propagation of the COT variability to equivalent CTP variation.

We compute ΔI by adding an aerosol of type continental average [Hess et al. 1998]. This aerosol has a scale height of 8 km and an opacity of 0.1. It is slightly absorbing. We have $\Delta I = I_{with\ AER} - I_{without\ AER}$. As seen in figure 4.3.5, $\Delta I/I$ globally decreases with increasing opacities. Its sign changes for intermediate opacities (~5-15). For low COT, continental aerosols reflectance is added to the thin cloud and produce a higher reflectance. For high opacities, the reflectance is saturated/dominated by the cloud and the aerosols absorption impacts it. It results in a lower reflectance. Regarding the equivalent COT variation, it also decreases with increasing opacities. ΔCOT sign changes for opacities ~4-10. To compute ΔCTP , we use $\Delta R = R_{cot-\Delta cot/2} - R_{cot+\Delta cot/2}$. Again the impact is maximum for thin clouds at high altitude. However because of the aerosol absorption effect an opposite ΔCTP can reach amplitude values of ~7.5hPa for low level thick clouds.

4.3.4.b Maritime clean

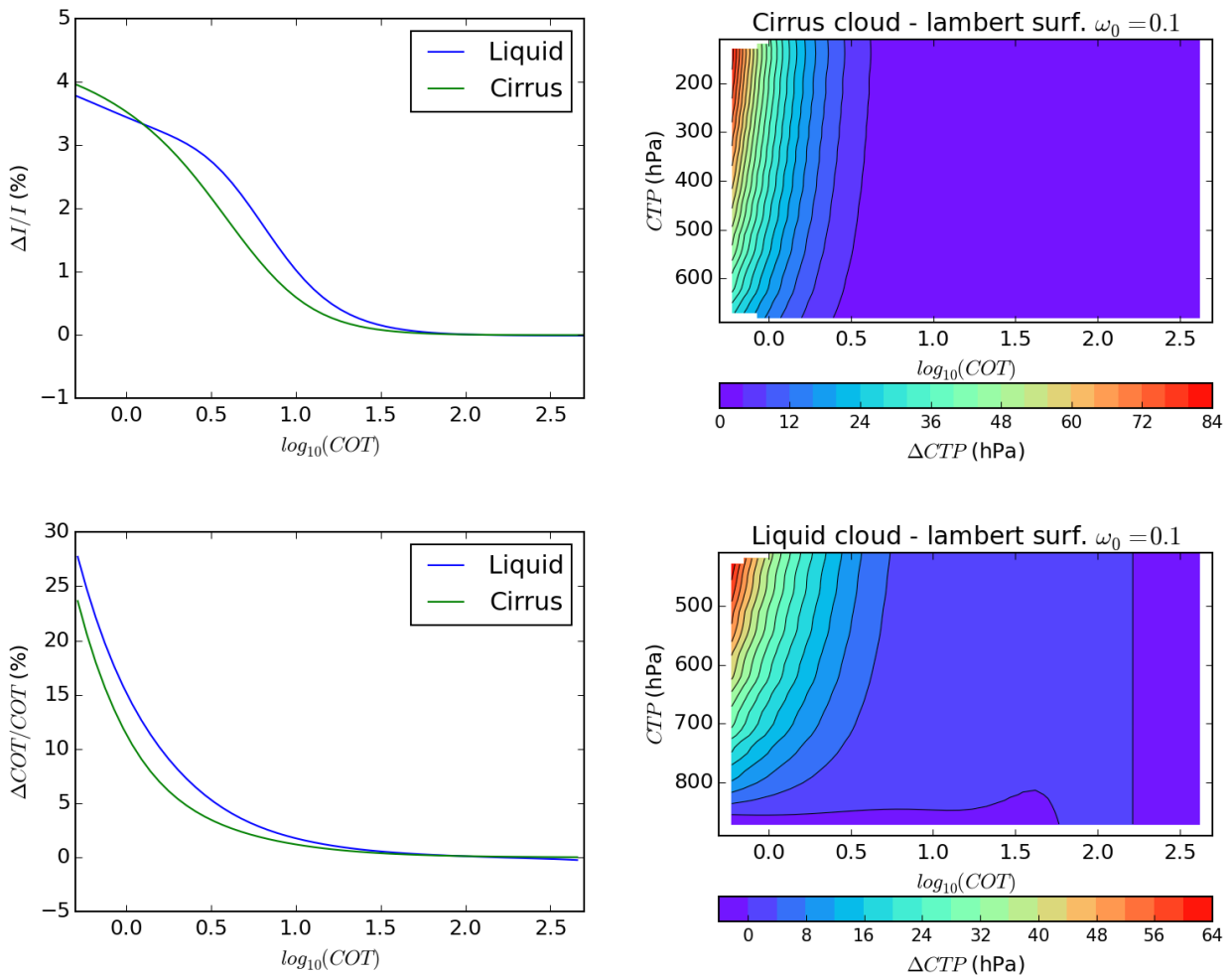


Figure 4.3.6 (Upper left) Relative variation of reflectance due to the presence of a maritime clean aerosol ($H=1\text{km}$, $\tau=0.1$). (lower left) Equivalent relative variation of COT. (Right) Propagation of the COT variability to equivalent CTP variation.

We compute ΔI by adding an aerosol of type maritime clean [Hess et al. 1998]. This aerosol has a scale

height of 1 km and an opacity of 0.1. Contrarily to continental average aerosols, it is almost purely scattering. We have $\Delta I = I_{with\ AER} - I_{without\ AER}$. As seen in figure 4.3.6, to add the maritime aerosol systematically results in an increase of the reflectance. $\Delta I/I$ decreases with increasing opacities. The mechanism is the same as with the continental aerosol except there is not sign change because the maritime aerosol does not absorb significantly. The equivalent COT variation also decreases in amplitude for increasing opacities. To compute ΔCTP , we use $\Delta R = R_{cot-\Delta cot/2} - R_{cot+\Delta cot/2}$. Again the impact is maximum for thin clouds at high altitude. ΔCTP amplitude is smaller than $\sim 8hPa$ for COT greater than ~ 3 .

4.3.5 Surface directionality

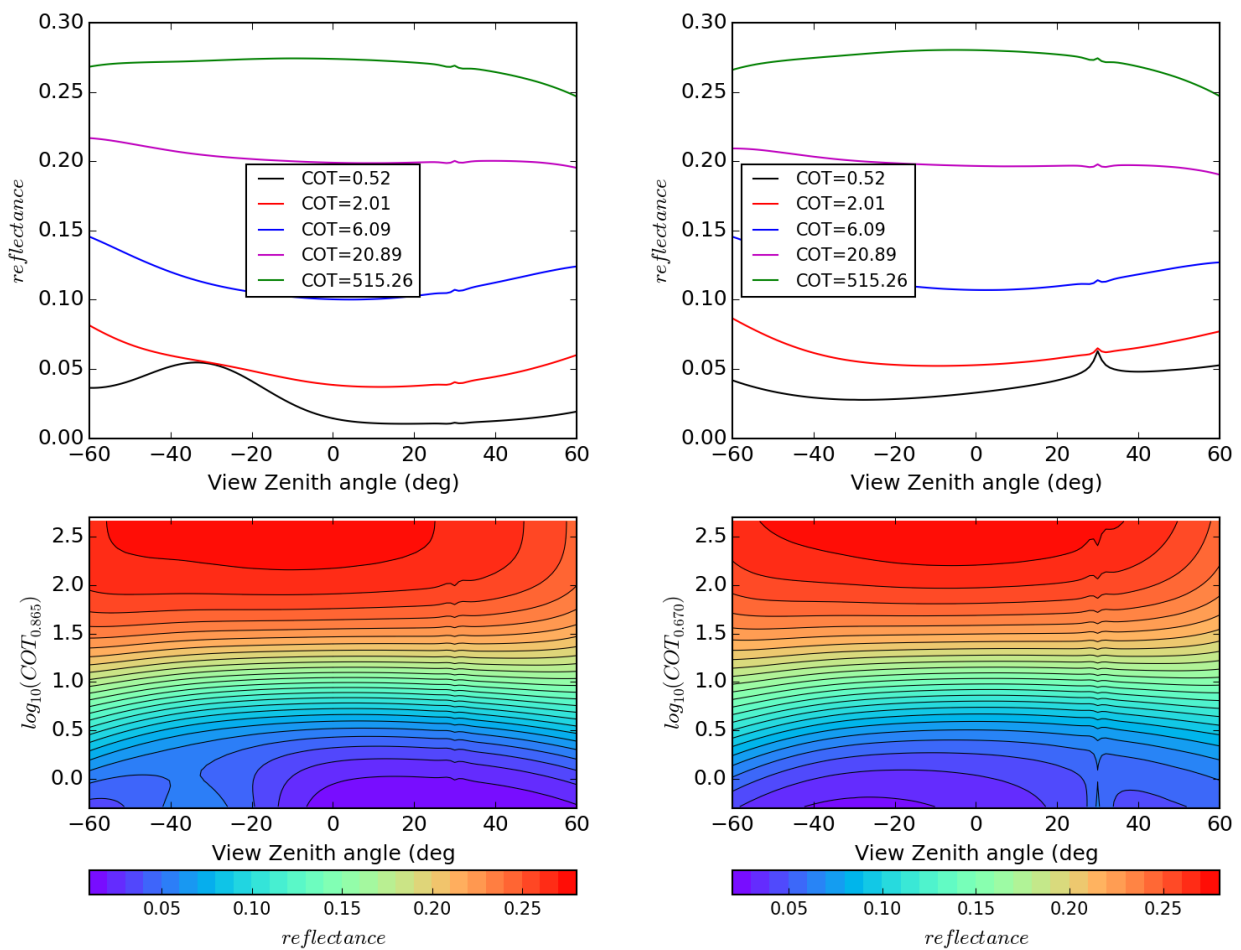


Figure 4.3.7 (left) 865nm reflectance as a function of COT and view zenith angle in the principal plane for a wind speed of 5m/s (right) 670nm reflectance as a function COT and view zenith angle in the principal plane for a needle-leaf forest BRDF. The sun zenith angle is 30° for both cases. The cloud properties are for ice cloud.

In that section we study the BRDF impact on the reflectance and the equivalent change of COT together with its propagation to an equivalent change of CTP. We use the same BRDF modelling as described in section 4.2.10. Figure 4.3.9 shows the corresponding reflectance for ocean at 865nm and needle-leaf forest at 670

nm for ice cloud. Indeed, we plan to use those respective wavelengths over ocean and land . ΔI , ΔCOT and ΔCTP are represented in a 2 dimension (COT, view zenith angle) space while CTP is fixed to 400hPa and 800hPa for ice and liquid clouds, respectively.

4.3.5.a Water surface

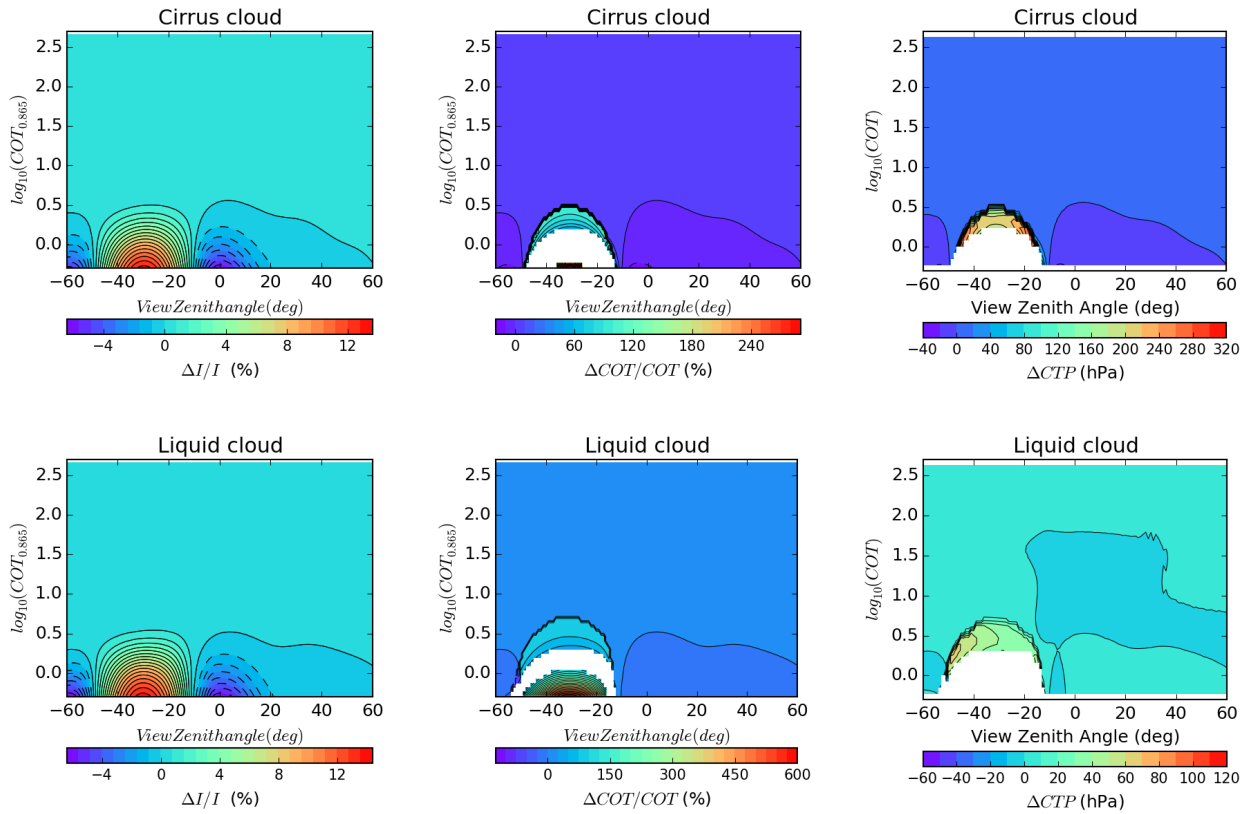


Figure 4.3.8 (Left) Relative variation of reflectance as a function of COT and view zenith angle in the principal plane due to a variation of the wind speed of $\pm 10\%$ regarding 5m/s. (middle) Equivalent relative variation of COT. (Right) Propagation of the COT variability to equivalent CTP variation. The sun zenith angle is 30° for both cases.

We compute ΔI by varying the wind speed by $\pm 10\%$ regarding 5 m/s. We have $\Delta I = I_{4.5m/s} - I_{5.5m/s}$. As seen in figure 4.3.8, to decrease the wind-speed results in an increase of reflectance at glitter's peak and a decrease in the wings as expected for the glitter spread. The variation is lower for backward directions. The corresponding COT variation is strong for thin clouds around the glitters. As seen in figure 4.3.7, this is explained by the reflectance being weakly sensitive to the COT in that "COT, geometry" regime. To compute ΔCTP , we use $\Delta R = R_{cot-\Delta cot/2} - R_{cot+\Delta cot/2}$. The equivalent CTP variation is very important for thin clouds in the glitter. It is lower in the backward scattering direction. The feature seen in the liquid case at $COT \sim 10$ in backward directions is a numerical artefact. It corresponds to a change of sign but for very small amplitude ($< 0.8hPa$). For clouds with COT greater than $\sim 5-6$, the amplitude of ΔCTP is smaller than 10hPa.

4.3.5.b Land surface

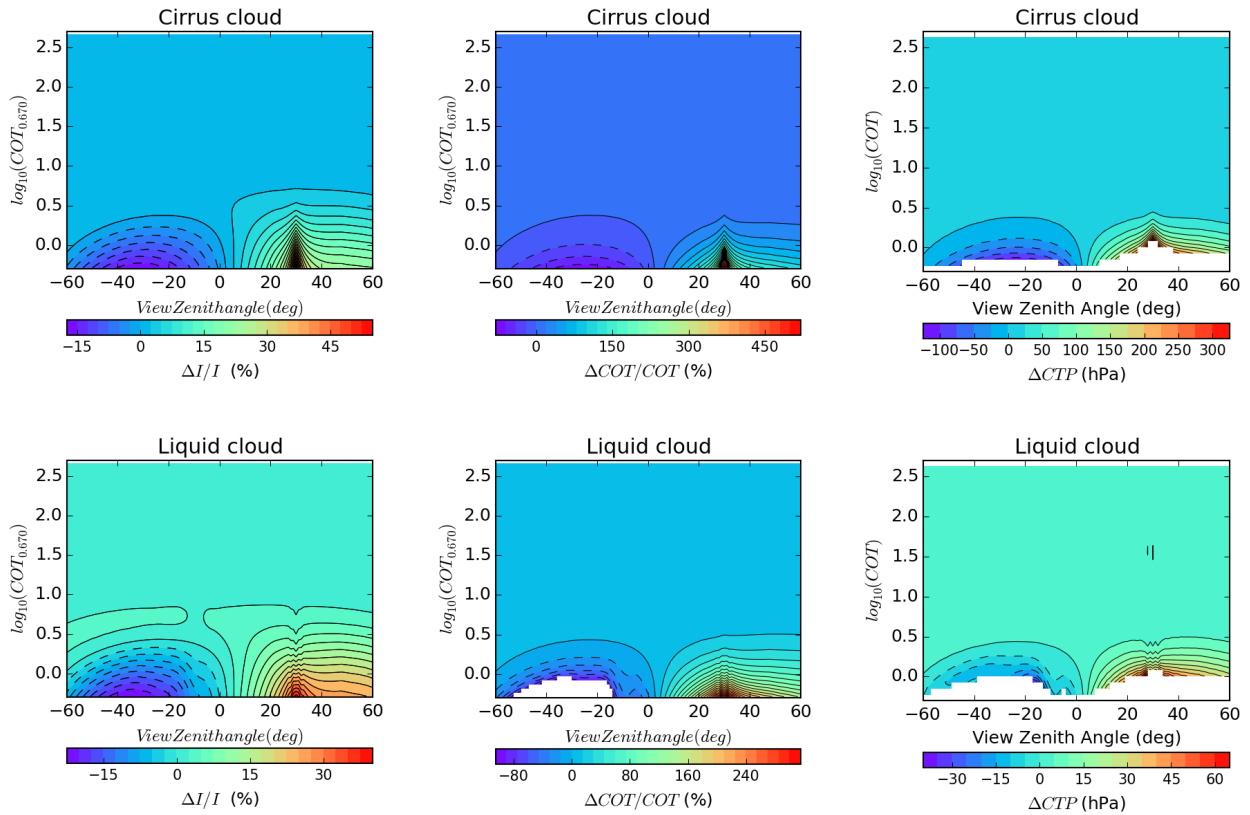


Figure 4.3.9 (Left) Relative variation of reflectance as a function of COT and view zenith angle in the principal plane due to change of BRDF from a desert to a broad-leaf forest. (middle) Equivalent relative variation of COT. (Right) Propagation of the COT variability to equivalent CTP variation. The sun zenith angle is 30° for both cases.

We compute ΔI by varying the land BRDF from a desert to a broad-leaf forest one. This is the biggest expected change of BRDF shape for land surfaces (excluding snow and ice). We have $\Delta I = I_{broad-leaf} - I_{desert}$. As seen on figure 4.3.9 to change from desert to a broad-leaf forest BRDF essentially results in a decrease of the reflectance in the forward direction and an increase of the reflectance in backward direction. This is fully consistent with the BRDF shape showed in figure 4.2.12. Again the equivalent COT variation is considerable for thin clouds. To compute ΔCTP , we use $\Delta R = R_{cot-\Delta cot/2} - R_{cot+\Delta cot/2}$. The equivalent CTP variation reaches values >300hPa for ice clouds backward scattering (Hot-Spot). For clouds with COT greater than ~5, ΔCTP amplitude is smaller than 10hPa.

4.4 Conclusion on sensitivity study

We extended the sensitivity studies gathered from the bibliography by continuously spending the range of COT, CTP when deriving the impact of different parameters. We also added some cases, in particular the impact of the BRDF or more specifically for METImage, the impact of varying the ISRF wings. We also performed the sensitivity study on the COT retrieval and propagated the ΔCOT to an equivalent variation of CTP. As expected, we see that the retrieval for thin clouds is the most challenging. Most of the parameters uncertainties will propagate to a bias that is strong for these. We see that the CGT and vertical

profile impact is not restricted to thin clouds. The vertical profile is even peaked for thickest clouds. To properly account for there variability is then of prime importance. The ice particle model also impacts significantly low altitude thick clouds.

5 DAY 1 ALGORITHM AND LOOK-UP TABLES

In this section, we describe the day-1 algorithm and corresponding LUTs. The algorithm is tested with synthetic METimage data and MERIS data in section 6. Its limit and foreseen improvements are described in section 7.

5.1 General description

The algorithm is based on the optimal estimate method with Levenberg-Marquardt iteration (see Rodgers [2000]). The Cloud Optical Thickness and Cloud Top Pressure are jointly retrieved as the state vector (COT, CTP). The measurement vector to be used is (I_{VII-6} , I_{VII-5}/I_{VII-4}) over water surface and (I_{VII-3} , I_{VII-5}/I_{VII-4}) over the land. Water is darker at 865 nm (VII-6) and the effect of aerosols is lower. Over the land, vegetation is darker at 670 nm (VII-3). To account for ozone absorption, a correction of observed TOA reflectance is performed with the assumption that the ozone absorption is not coupled to the scattering media. LUTs are used as forward model.

As already stated, the information content from METimage data is not sufficient to retrieve or even constrain the vertical profile and CGT as well as the CTP and COT. Unfortunately it has a significant impact on the signal ratio 763/752nm and must properly be varied to reduce biasing of the retrieval. We parametrized CGT and the vertical profile as a function of COT and CTP from climatology studies :

- The CGT is parametrized using CLOUDSAT/CALIPSO data climatologies for year 2008. These are shown on Figure 5.1.1. We distinguish between ice and liquid cloud as well as between ocean and inland locations.
- For the vertical profile, we use CPR profiles from Carbajal-Henken et al. [2013] (see figure 2.3.2). CPR profiles are given for the 9 ISCCP cloud type. To avoid discontinuities, the profiles are interpolated in the (CTP, COT) space. The geometrical thickness of the profile is scaled according to the CGT climatology.

It is important to note that this approach allows us to vary either CGT and the vertical profile without extra LUT entry. We only consider mono-layer clouds in the LUTs.

Separate LUTs for each phase (ice and liquid clouds) are created. The effective radius has a moderate impact for $COT < 10$ and a supplementary entry would unnecessarily make the LUT heavier. On the other hand, no clear tendency could be derived for a $R_{eff} = f(COT, CTP)$ climatology from MODIS data.

The directionality of the surface reflectance has a noticeable impact for the retrieval of thinner clouds. For the ocean, the considered surface model is the one described in section 3.4 and based on Cox and Munk [1954]. We sample the wind speed in the LUT. For Earth land-surfaces, in order to account for the diversity of directionnal effects, we consider 7 different surface kinds (biomes): (i) desert, (ii) grasses/cereal crops (iii) broad-leaf forests, (iv) needle-leaf forests, (v) shrubs, (vi) savannas and (vii) snow/ice. These biomes BRDF are represented with a Li-Ross model with hot-spot [Maignan et al. 2004] except for the snow/ice that is modelled as Lambertian. We use the Bidirectional Anisotropy Standard shapes (BASEs) from Bacour and Bréon [2005] for normalized volumetric and geometric parameters of each biome (see Table 2). One LUT is created for each biome and the white sky albedo is sampled in each LUTs. These LUTs are loaded successively in the retrieval to process pixels with the corresponding surface type. The surface pressure is also sampled in LUTs.

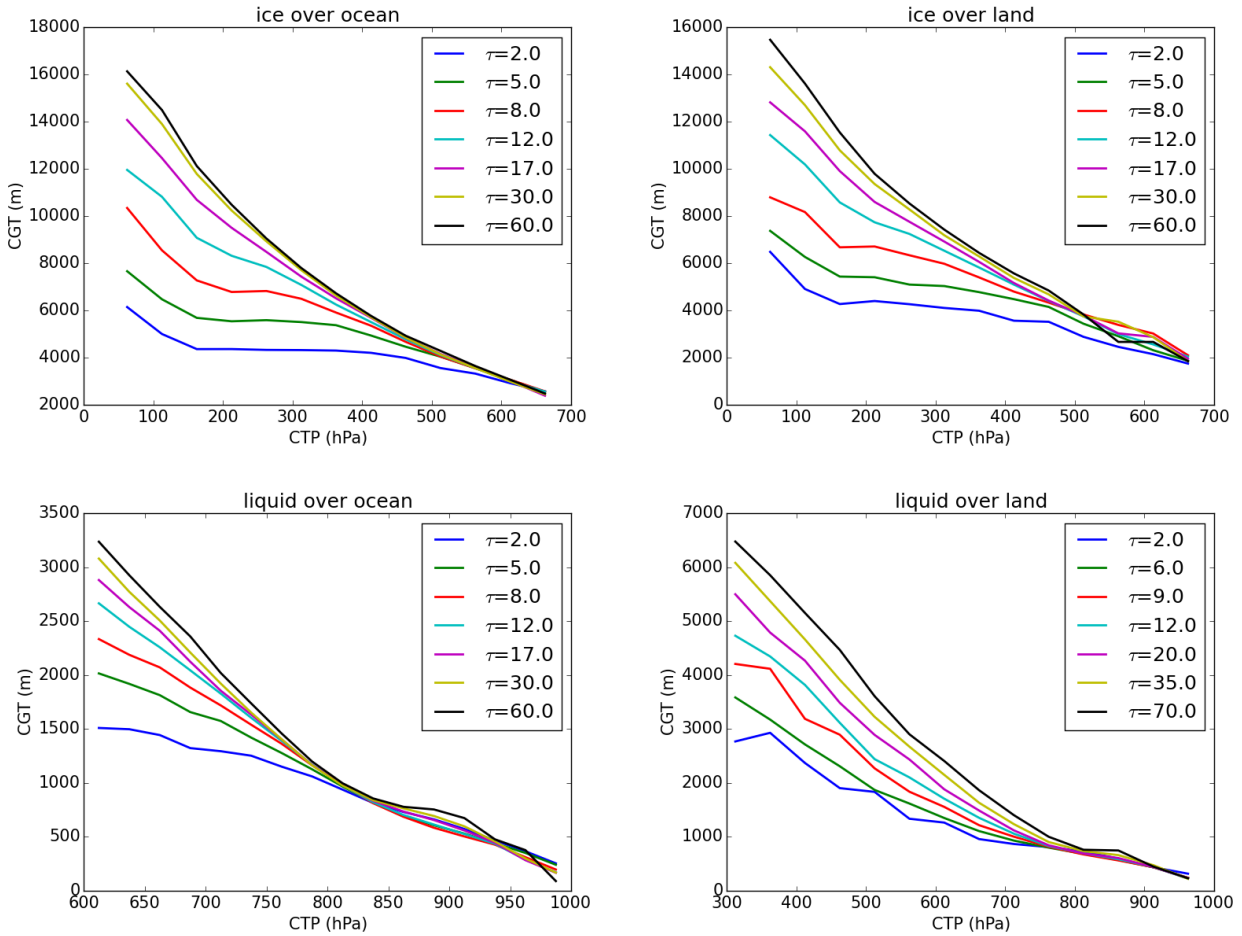


Figure 5.1.1 Climatology of Cloud Geometrical Thickness (CGT) per class of Cloud Optical Thickness and varying Cloud Top Pressure (CTP). (Upper left panel) ice cloud over ocean, (Upper right panel) ice cloud over land, (lower left panel) liquid cloud over ocean and (lower right panel) liquid cloud over land. Statistics are obtained from one year of CloudSat/Caliop measurements (product : 2B_GEOPROF_LIDAR, year : 2008, effective of population : 1096505 (liquid clouds) , 586170 (ice clouds)).

We could add aerosols depending on the surface type (e.g maritime clean for water, dust for desert, etc) but such aerosol would have constant properties (e.g. opacity) over a given LUT to avoid any extra LUT entry.

Finally the following parameters are sampled in the LUTs:

- Optical thickness, COT
- Cloud Top Pressure, CTP
- Solar Zenith angle, SZA
- View Zenith Angle, VZA
- Relative Azimuth, RAA
- White sky albedo land surfaces (WSA) / wind speed for water surface (W_{spd})
- Surface pressure (P_{surf})

We have a LUT for the intensity (I , either 865 nm or 670 nm) and a LUT for the signal ratio 763 nm/752 nm (R). The R_{LUT} depends on all parameters listed above while the I_{LUT} does not depend on the CTP and P_{surf} . By neglecting CTP variability in I_{LUT} , we neglect the effect of varying the Rayleigh opacity above the cloud but the total Rayleigh opacity at 670nm is <0.05 . The R_{LUT} has 7 dimensions while the I_{LUT} has 5 dimensions. On

the other hand, the I_{LUT} and R_{LUT} do not follow the same variability regarding the geometry. The intensity can vary sharply regarding the scattering angle (because of the rainbow or sun glitter for example) while the signal ratio is more affected by the air mass, so the cosine of the solar zenith and view zenith angles. I_{LUT} is then sampled on a higher resolution grid with constant angle steps while R_{LUT} is sampled on a lower resolution grid with constant steps in cosine of SZA and VZA. RAA follows a grid with constant angle steps in both R_{LUT} and I_{LUT} but with a better resolution for I_{LUT} . COT, WSA and W_{spd} are the same for both R_{LUT} and I_{LUT} .

For the retrieval, we need to build a set of 16 $R_{LUT} - I_{LUT}$ couples (2 cloud phases x 8 surface types).

5.2 Specifics about the $CTP - P_{surf}$ space in LUT

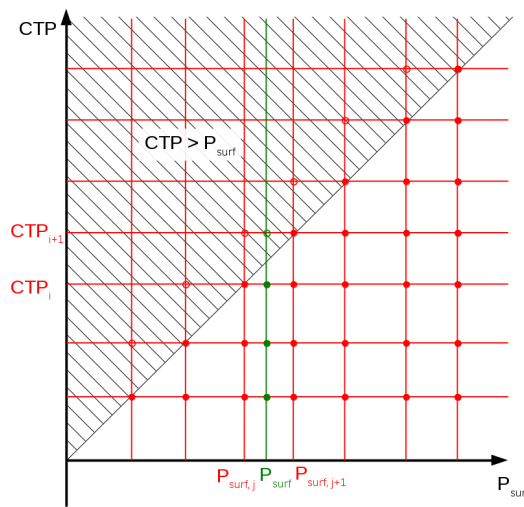


Figure 5.2.1 Representation of the CTP and P_{surf} dimensions of LUTs. Red grid represents the LUT sampling. Hatched area shows the space for which no LUT entry can be computed since $CTP > P_{surf}$. The green axis shows $R=f(CTP)$ for an interpolated value of P_{surf} . Filled circles represent computed LUT entries while void circles represent non-physical “ghost” values computed by extrapolation of values defined in the LUT (see the text).

In building the LUTs, grid points for which the CTP is higher than the considered P_{surf} are not defined. On the Figure 5.2.1, the corresponding area is represented with hatching. Because of the finite sampling, this can cause some CTP values close to P_{surf} not to be defined. Looking at Figure 5.2.1, for the P_{surf} value, the highest defined CTP (filled circles) will be CTP_i that is lower than the P_{surf} . R is undefined for $P_{surf} > CTP > CTP_i$ because the interpolation to that range imply the grid point $(CTP_{i+1}, P_{surf,j})$ that is undefined. To avoid that, we add “ghost” points (void circles in Figure 5.2.1) to the LUTs that are non-physical numerical extrapolation of $R=f(CTP)$ to the first $CTP > P_{surf}$ grid point. This allows to compute R for $P_{surf} > CTP > CTP_i$ during the retrieval.

We sample the $CTP - P_{surf}$ space so that any P_{surf} sample has a corresponding CTP sample = $P_{surf} - 1$ hPa (grid points almost on the diagonal on Figure 5.2.1)

5.3 Specifics about optimal estimate

The measurement vector is $y = (I, R)$. The state vector is $x=(\log_{10}(COT), CTP)$ and the non retrieved parameter vector is $b=(W_{spd}, P_{surf}, SZA, VZA, RAA)$ over water surface and $b = (WSA_{670}, WSA_{752}, P_{surf}, SZA,$

VZA, RAA) over land. The forward model $F(x, b)$ is made up of LUTs linear interpolations. $F(x, b) = (I_{LUT}(x,b), R_{LUT}(x,b))$. The non-retrieved parameters are set on a pixel-by-pixel basis. The first guess state vector $(\log_{10}(COT_0), CTP_0)$ is computed on a pixel-by-pixel basis using simple 1-D interpolation into the LUT:

- COT_0 is obtained by looking at the value in I_{LUT} that is the closest to measured I (knowing b).
- CTP_0 is then obtained by looking at the value in R_{LUT} that is the closest to measured R (knowing b and COT_0).

We do not have any a-priori state vector x_a . We then set the corresponding covariance (S_a) to a huge values and $x_a = x_0$.

Superior and inferior limits x_{lim} are given to the OE routine for the state variable (COT,CTP). These generally corresponds to the limits of the LUT range. The first guess and prior estimate must lie into that limits and during the iterations, x_{i+1} must also be included in that range.

The covariance matrix S_ϵ used for the retrieval is $S_\epsilon = S_y + S_F + S_i$ where

- S_y is the covariance due to measurement noise. It is a diagonal matrix with $S_{y(0,0)}$ the variance of I due to noise and $S_{y(1,1)}$ the variance of R due to noise.
- S_F is the covariance due to the non-retrieved parameters uncertainties. $S_F = K_b S_b K_b^T$. K_b is the Jacobian (sensitivity) of the forward model regarding non-retrieved parameters. S_b is the covariance matrix of non-retrieved parameters. S_F should be computed on a pixel-by-pixel basis. However, this computation is time consuming and S_F can then be optionally computed only once for a given value of b . This is treated as a noise because S_b is not necessarily systematic but rather random.
- S_i is a covariance matrix corresponding to interpolation error on I and R due to LUT sampling. It is a diagonal matrix. S_i is also treated as a noise. Although the error is systematic given a set of state vector and non-retrieved parameter, we do not manage to characterise this error continuously for the whole range of values and rather treat it as random.

The bias on measurement $S_{y,bias}$ is not used in the retrieval through S_ϵ since it is a systematic error. We only account for it when computing the posterior estimate covariance: $S_{x,bias} = G_y S_{y,bias} G_y^T$ with the gain matrix G_y defined as $G_y = (K^T S_\epsilon^{-1} K + S_a^{-1})^{-1} K^T S_\epsilon^{-1}$

Levenberg-Marquardt method is used for the iterative process (see Rodgers [2000], eq 5.36):

$$x_{i+1} = x_i + [(1+\gamma) S_a^{-1} + K_i^T S_\epsilon^{-1} K_i]^{-1} \{ K_i^T S_\epsilon^{-1} [y - F(x_i)] - S_a^{-1} [x_i - x_a] \}$$

with x_i the state vector, K_i the weighting function (Jacobian) of the forward model regarding the state vector, $F(x_i)$ the forward model, y the measurement vector, x_a and S_a the prior state vector and its covariance matrix and S_ϵ the covariance matrix described above. γ is a parameter adjusted to minimize the cost function J_{i+1} . Iterations starts at number 1. At i^{th} iteration:

1. we set $\gamma_i = \gamma_{init} / 10^{i-1}$ with $\gamma_{init} = 0.1$
2. we compute the x_{i+1} :
 - While " $J_{i+1} > J_i$ " or " x_{i+1} is out of x_{lim} ", γ_i is multiplied by 5.0:
 - If γ gets greater than 10^{10} , we exit with the current x_i and do not account for the i^{th}

iteration

- Otherwise if $J_{i+1} \leq J_i$ (so x_{i+1} is within x_{lim}) we update x_i and go to the next iteration.

A retrieval is considered as failed if no satisfying γ is found at iteration 1.

During the OE, iteration stops if at least one the the three following condition is true:

- Maximum number of iteration reaches ($N_{iterMAX}=15$)
- Cost function not significantly reduced between two iterations ($\frac{J_{i-1} - J_i}{J_{i-1}} < 0.01$)
- $[y - F(x_i)] S_\epsilon^{-1} [y - F(x_i)] \leq n_y$ where n_y is the dimension of the measurement vector.

5.4 Input level 1b data and ancillary data

The algorithm uses calibrated level 1b data. It requires TOA reflectance for channels VII-3 (670nm), VII-4 (752nm), VII-5 (763nm) and VII-6 (865nm). The viewing and sun geometries are also required.

Additional auxiliary data are needed:

- A cloud mask and cloud phase mask
- The ground level atmospheric pressure or the sea level atmospheric pressure and Digital Elevation Model (DEM)
- The 670 and 752-763 nm surface white sky albedo
- The wind-speed
- The ozone column
- Land sea mask and Land Cover Type (e.g. IGBP type).

The phase mask is required as an ancillary data in order to successively load the corresponding LUT for the retrieval. However, if such a mask is not available, the retrieval could be done by assuming that the phase switches at a given critical CTP value.

5.5 Output data

The algorithm outputs are stored in HDF5 files. Stored products has the same dimension as the level1b data. Floats are store as float32. The output file contains:

- The geolocation (latitude and longitude)
- The retrieved COT at 670 nm (even above ocean where the 865 nm channel is used to retrieve the COT)
- The CTP in hPa
- The COT uncertainty (standard deviation)
- The CTP uncertainty (standard deviation) in hPa

As test outputs, we also write in file:

- The first guess state vector (COT₀, CTP₀)
- The cost function for the first guess state vector
- The final cost function
- The number of iterations (stored as INT8)
- The residual for I (either 670 or 865 nm channel) in % of I
- The residual for R in % of R
- the uncertainties (on COT and CTP) due to the a-priori measurement uncertainties
- the uncertainties (on COT and CTP) due to the forward model uncertainties
- the uncertainties (on COT and CTP) due to the measurement vector uncertainties
- A flag value describing the state of the pixel
 - 0 non-treated
 - 1 successful retrieval
 - 2 failed retrieval
 - 3 not treated because non retrieved parameters exceeded the range sampled in LUT
- A flag value describing the reason for OE iteration stop
 - =0: N/A (pixel non treated)
 - =1: No satisfying gamma value found
 - =2: Maximum number of iteration reached (N_{iterMAX}=15)
 - =3: Cost function not significantly reduced between two iterations ($\frac{J_{i-1} - J_i}{J_{i-1}} < 0.01$)
 - =4: $[y - F(x_i)] S_c^{-1} [y - F(x_i)] \leq n_y$ where n_y is the dimension of the measurement vector

5.6 LUT built in the present study

The LUT are built with the ARTDECO radiative transfer package (see section 3.4). We use specifically the DOAD adding and doubling RTE solver. The phase function of any used particle (either cloud or aerosols) are truncated with the δ -M method. In order to obtain LUTs in a reasonable time regarding the study time line, we use 8 computational angles (streams) and apply the single scattering correction (TMS) to the TOA reflectance. For a pure scattering liquid cloud of opacity 5.0 (see benchmark from Kokhanovsky et al. [2010]), the obtained TOA radiance is accurate to better than 0.4% out of the rainbow and glory geometries. Note that for the future building of LUTs to be used for the operational retrieval, this number of streams can be increased. The polarisation is neglected in the computation. It has a negligible impact at studied wavelengths. The Rayleigh scattering is accounted for with an opacity following Hansen and Travis [1974] and a depolarisation factor of 0.0279 Young [1980].

The gas absorption is treated with a correlated k-distribution (see section 3.4). Specific k-distribution for the METimage and MERIS channels were derived using a line-by-line model and the HITRAN database [Rothman et al. 2009]. We only use k-distribution for O₂ absorption in METimage channel 5 and MERIS

channel 11. No gas absorption is considered in other channels. Indeed, transmission in those channels is >99.9% after ozone correction (in observed TOA reflectance). The MERIS ISRF used is the nominal one, centred at 761.875 nm with a FWHM=3.744 nm (see also Figure 2.3.1). We do not account for the smile effect that corresponds to a variation of the central wavelength. This will be discussed in section 6.2. The METimage ISRF is taken as a rectangle function with central wavelength and FWHM described in Table 1. In both METimage and MERIS cases, we use 20 k-intervals. The resulting error on the transmission is less than 1.5% for airmass<10 compare to the exact line-by-line computation.

The meteorological profile is the AFGL US62 from Anderson et al. [1986]. The atmosphere vertical resolution is re-sampled to 1.0 km outside the cloud and 100m inside the cloud with an extra 5 levels within 0.1% of the CTP level. We cut the atmosphere at 50 km (0.98 hPa).

The liquid cloud optical properties are computed using the Mie theory. The size distribution of droplets follows a log-normal distribution with an effective variance of 0.09. The optical properties of ice clouds are those of General Habit Mixture ice particles from Baum et al. [2014]. We fix the particle effective radius to 14 and 25 microns for liquid and ice clouds respectively. Those values are typical average value derived with MODIS [King et al. 2013]. LUTs are free of aerosols.

We created several different sets of LUTs. Two different resolutions are tested : one “medium” and one “high”. The sampling for those two resolutions is summarized in Table 3. The precision related to the LUT sampling/interpolation is reported in section 6.1.2. I_{LUT} and R_{LUT} at “medium” resolution stored in float32 (single precision) weights 55 and 26 Mo, respectively. For “high” resolution, I_{LUT} and R_{LUT} weights 185 and 1026 Mo, respectively. We create a set of LUTs using the vertical structure (CGT, profile) climatology and an other one with homogeneous cloud vertical profile and constant CGT = 1km. This last set of LUTs is necessary for the testing of the algorithm against METimage synthetic data (see section 6.1) since the vertical structure climatology is not available in the simulator that is used to obtain the synthetic data.

	Sampling steps	minimum value	maximum value	# of sample “medium”	# of sample “high”
COT	constant steps in $\log_{10}(\text{COT})$	0.1	500.0	10	20
CTP	constant steps in CTP	50 hPa	1080 hPa	13	30
P_{surf}	constant steps in P_{surf}	850 hPa	1080 hPa	5	10
W_{spd}	constant steps in W_{spd}	1 m/s	15 m/s	3	5
WSA	constant steps in WSA	~0 (~0.5 for snow/ice)	~0.4 (~1.0 for snow/ice)	3	5
SZA	I_{LUT} : constant steps in SZA R_{LUT} : constant steps in $\cos(\text{SZA})$	0°	70°	I_{LUT} : 36 R_{LUT} : 9	I_{LUT} : 36 R_{LUT} : 15
VZA	I_{LUT} : constant steps in SZA R_{LUT} : constant steps in $\cos(\text{SZA})$	0°	70°	I_{LUT} : 71 R_{LUT} : 10	I_{LUT} : 71 R_{LUT} : 15
RAA	constant steps in RAA	0°	180°	I_{LUT} : 181 R_{LUT} : 38	I_{LUT} : 181 R_{LUT} : 38

Table 3: Characteristics of the LUT sampling. Note: in the LUT building process, k_0 (isotropic BRDF parameter) is actually sampled between 0.0 and 0.45. The WSA is then obtained for each biomes separately.

For METimage, R_{LUT} corresponds to VII-4/VII-5 (763/752 nm) while it corresponds to channel 11/channel 10 (761/753 nm) in MERIS case. I_{LUT} is either for VII-3 (670nm, over land) or VII-6 (865nm, over water) in METimage case while it is for channel 7 (665nm, over land) and channel 13 (865 nm, over water) in MERIS case. We also compute a $I_{LUT-752nm}$ in MERIS case, in order to test our algorithm with the same channel as the MERIS operational retrieval (see section 2.3.1).

For the land BRDF modelling, in the current LUTs building, we use the normalized volumetric and geometric parameters for each biome as given by Bacour and Bréon [2005] at 670nm (see Table 2) either for the 670 nm and for the 752/763nm. An interpolation using the values given by Bacour and Bréon [2005] at 865nm could be done in a future version.

LUTs are stored in HDF5 format. A single file contains I_{LUT} and R_{LUT} for ice and liquid clouds for a given surface type. An example for LUT file name is *LUT_MERIS_shrubs_medium_climato_ghost.he5*.

- LUTs correspond to *MERIS* instrument.
- LUTs correspond to *shrubs* surface.
- LUTs correspond to *medium* resolution (see Table 3)
- The string *_climato_* is present in the file name because the cloud vertical structure (CGT, profile) climatology (see section 5.1) was used. If homogeneous cloud is used, this string is not present
- This file has the extension *_ghost.he5* because “ghost” points were added (see section 5.2).

High level scripts for the LUTs building was written in Python (2.7). Those scripts loop over the LUT sampling grid. For a given grid point, it sets-up some variables for the RT computation (e.g. atmospheric profile, cloud physical properties, etc) and call ARTDECO through its Python interface. The computation was parallellized because of the high CPU demand. As an example, in our case (adding-doubling RT solver with 8 streams) the computation of single high resolution R_{LUT} for an homogeneous profile (CGT=1.0 km) liquid cloud requires about 51 days of CPU (on a Intel(R) Xeon(R) CPU E3-1230 v3 @ 3.30GHz with 8192 KB of cache). Note that this CPU demand can vary significantly depending on the RTE solver because the atmospheric content will impact the CPU demand differently (e.g. an adding and doubling solver is sensitive to the opacity and number of layers in the atmosphere while a discrete ordinate solver is not). Indeed, the number of computational angles also plays a crucial role for the CPU demand.

5.7 Algorithm implementation for the present study

The prototype for day-1 algorithm was developed in Python (2.7) language. The use of such a high level language is convenient for a prototype algorithms. It simplifies significantly the I/O access for any file format (ASCII, HDF5, Envisat). Linear algebra operations are also simplified by the use of the Numpy/Scipy library. We developed a generic OE routine that can be used for any problematic (*oe_retrieval.py*). This routine is called by two specific routines: one for the METimage retrieval (*SDS_retrieval.py*) and an other one for MERIS retrieval (*MERIS_retrieval.py*).

The general structure of the retrieval is the following:

- 1 Read radiances and ancillary data
- 2 Loop on surface biomes present on the image

2.1 load LUTs for the treated biome

2.2 loop on pixels of the image corresponding treated biome

3 Write results

If a phase mask is available (for METimage SDS case), the retrieval can either be done one phase after the other (only one R_{LUT}/I_{LUT} couple loaded at a time) or the two phases together (two R_{LUT}/I_{LUT} couples loaded at a time). For the case where no phase mask is available, we need to switch from a phase to an other at a given CTP_{critical}. We then need to have two R_{LUT}/I_{LUT} couples loaded at a time.

As an ancillary data in the retrieval, we read the IGBP type for the surface. There are 17 IGBP types that we map into our LUT surface biomes as follow:

- **broadleaf forests** LUT biome gathers:
 - evergreen broadleaf forest IGBP
 - deciduous broadleaf forest IGBP type
- **desert** LUT biome gathers:
 - urban and built-up IGBP type
 - barren or sparsely vegetated IGBP type
- **grasses cereals crops** LUT biome gathers
 - croplands IGBP type
 - grasslands IGBP type
 - permanent wetlands IGBP type
 - cropland/natural vegetation mosaic IGBP type
- **needleleaf forests** LUT biome gathers
 - evergreen needleleaf forest IGBP type
 - deciduous needleleaf forest IGBP type
 - mixed forests IGBP type
- **savannas** LUT biome gathers:
 - woody savannas IGBP type
 - savannas IGBP type
- **shrubs** LUT biome gathers:
 - closed shrubland IGBP type
 - open shrublands IGBP type
- **snow/ice** LUT biome gathers:
 - snow and ice IGBP type
- **Water** LUT biome gathers:
 - water IGBP type

Additionally in the MERIS retrieval, we switch the biome to snow/ice for pixels with $WSA > 0.5$.

For wind speed values smaller than the smallest sampled value in LUT (1m/s), we use this smallest sampled value.

The forward model consists of LUT interpolation. As already mentioned, we perform multi-linear LUT interpolation. For an interpolation among N axis, the algorithm first look for the indices (in float) corresponding to values requested for each axis and perform the sum of 2N weighed values (each corner of the “polytope”) to obtain the interpolated LUT value.

The retrieval is parallelized. The actual CPU time required for a METImage 5 minutes granule (3800 x 3264 pixels) retrieval is of the order of 8.4 hours for 66.7% of cloudy pixels (on a Intel(R) Xeon(R) CPU E3-1230 v3 @ 3.30GHz with 8192 KB of cache). This corresponds to ~ 0.0036 s per pixel on average. In the algorithm, one of the first step in retrieving a given pixel is to reduce LUTs by performing the linear interpolation for the non-retrieved parameters. I_{LUT} is reduced from 5 dimensions to one dimension (COT) and R_{LUT} is reduced from 7 dimensions to 2 dimensions (COT, CTP). This step account for $\sim 30\%$ of the CPU time. 60% of the time is spend in the actual OE routine and $\sim 10\%$ remaining is spend to compute x_0 .

It should be noted that no significant effort was done to reduce this CPU demand for the retrieval since it was not the goal of the study. In particular, nested loop that are used in the algorithm are particularly not efficient in Python. On an other hand, no simplifications for diagonal matrix computation were performed. A big reduction of the CPU time can then be expected after optimization or translation to low level language (C, Fortran) for some parts of the algorithm.

On the other hand, it must be noted that when splitting the granule in smaller parts to be retrieved separately by a sub process for parallelisation, the number of pixels to be retrieved for a given surface kind can drop dramatically. In such a case, the time necessary to load the corresponding LUT can become a significant fraction of the actual retrieval time if each sub-process load LUTs separately.

6 DAY-1 ALGORITHM TESTING

In this section, we present the testing of the algorithm and LUTs described in section 5.

6.1 4MSDS synthetic data

The synthetic data are used to test either the retrieval (section 6.1.3) and the LUTs themselves (section 6.1.2). We will study the “high” resolution LUT since it is the resolution that is intended to be used in the future algorithm. We will also study the “medium” resolution LUTs because we used it for the testing on MERIS retrieval.

6.1.1 Data description

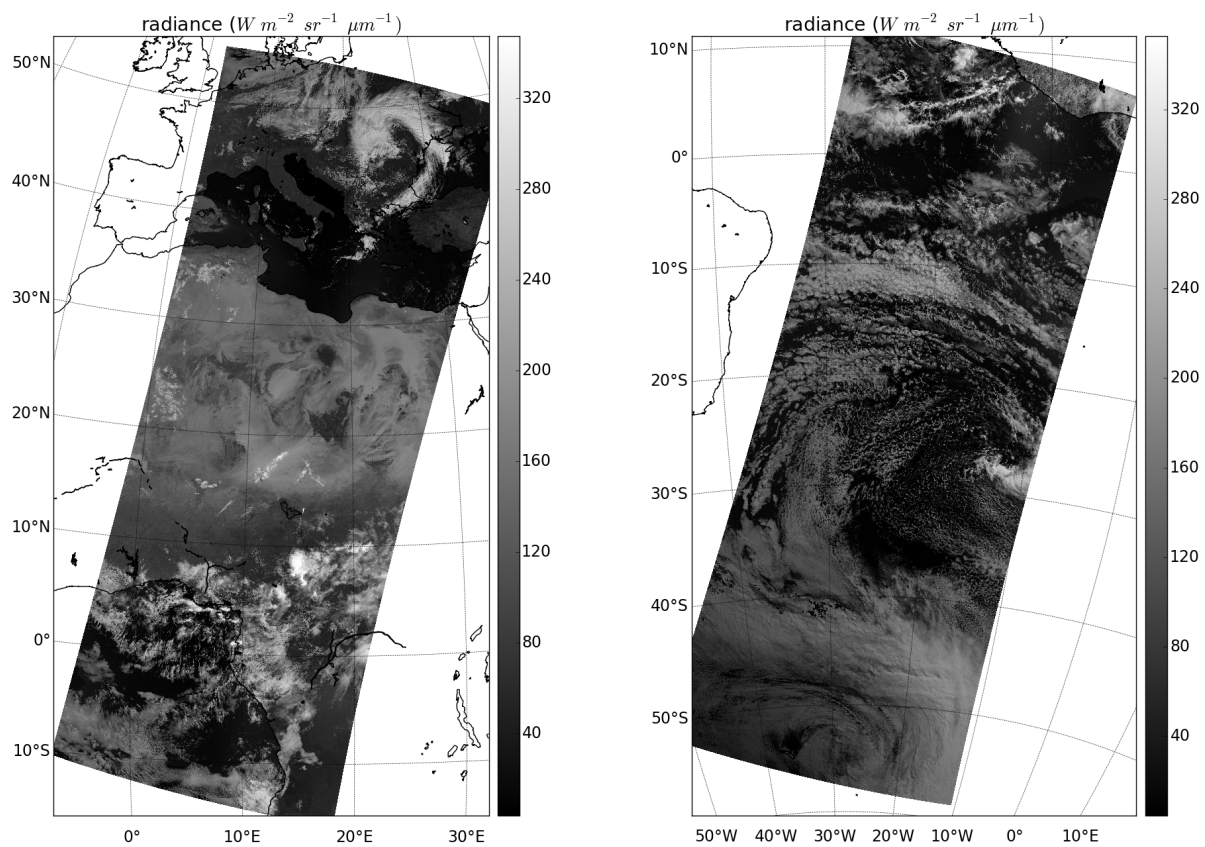


Figure 6.1.1 Synthetic data set for METImage VII-4 (752 nm) created with ARTDECO RT package as part of the EUMETSAT project “Test Data for the EPS-SG instruments METImage and 3MI”. Both panels represents ~20min data acquisition.

A former EUMETSAT study “EPS Second Generation – Test data for the METImage and 3MI instruments” (also called 4MSDS) has been performed to provide realistic synthetic test data for METImage (and 3MI) in support to the ground processor development. Top of the atmosphere (TOA) radiances for a full range of representative atmospheric and surface conditions are generated. Observation geometries (sensor reference frame) are simulated based on instrument sampling characteristics (instantaneous FOV, scan period and limit angles) and EPS-SG orbit propagation. Geolocation and sampling geometries are used to model the radiative transfer in which surface and atmosphere (clouds, aerosols, gas) are realistically described based on ancillary information obtained for dates and time of required simulation (among which AVHRR products for clouds, MACC reanalysis for aerosols, ECMWF reanalysis for atmospheric state, MODIS BRDF parameters

climatology for land properties). The simulated TOA radiances are generated at level 1b, equivalent to the calibrated and geolocated measurement. The radiative transfer part of the simulator is built around the ARTDECO package. Figure 6.1.1 shows the resulting simulated radiances corresponding to ~20 minutes of observation for VII-4 (752nm) channel. Figures 6.1.2 and 6.1.3 show the corresponding AVHRR COT and CTP. The visible-SWIR part of the METimage/3MI SDS simulator was developed by HYGEOS/LOA and we then have full access to the source code.

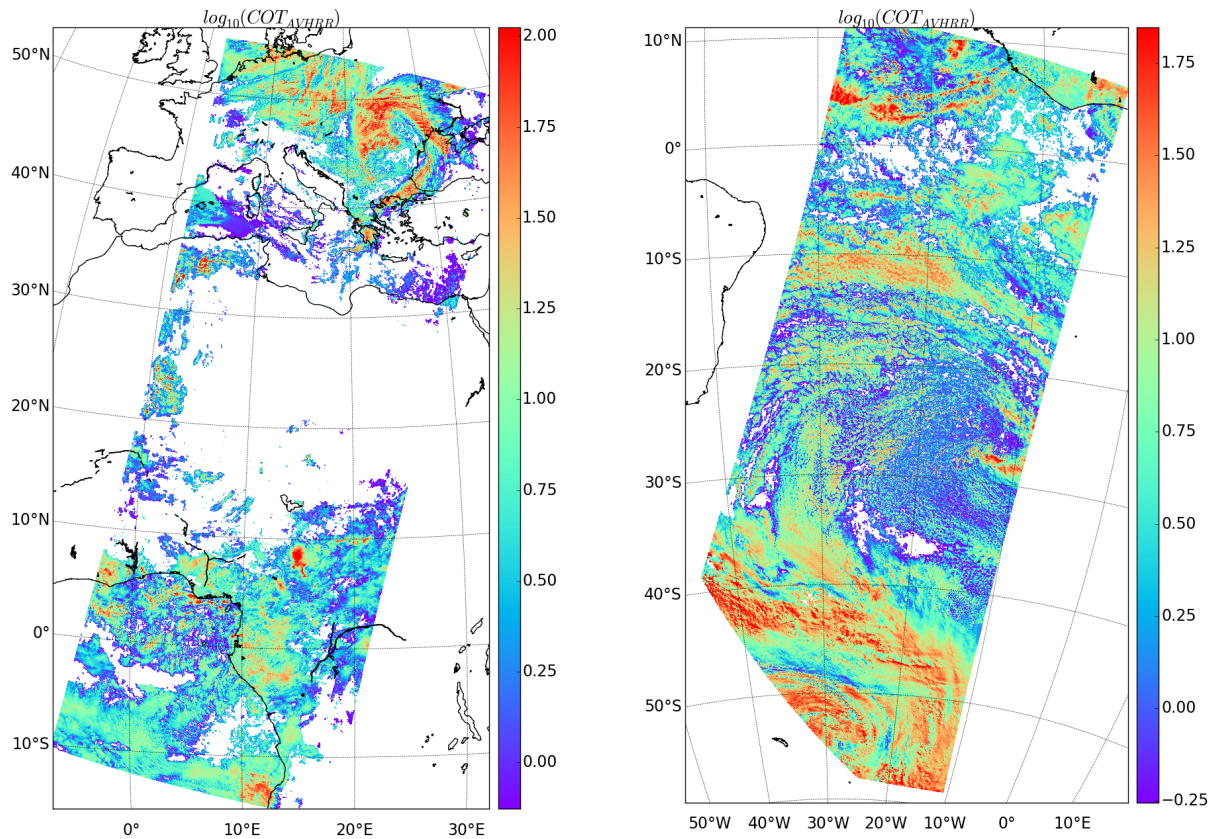


Figure 6.1.2 AVHRR (dcomp algorithm) Cloud Optical Thickness used for the SDS.

In order to properly manage all sources of discrepancy between the day-1 algorithm retrieval products and the AVHRR cloud products used to generate the synthetic dataset (SDS), we re-ran the SDS simulator with a modified physical modelling that perfectly match the one for LUT building (described in sections 5.1 and 5.6). Note that the cloud vertical structure (CGT, profile) climatology described in section 5.1 is not implemented in the SDS simulator. The testing here is then performed for homogeneous clouds with a constant CGT=1.0 km (either in the SDS simulator and LUTs). We focus on scenes displayed on figure 6.1.1 corresponding to ~2x20 minutes of data acquisition. Each scene is made of four ~5 minutes observation granule:

- For Europe/Africa scene, granules are:
 - 2007-09-12T08-43-03
 - 2007-09-12T08-47-47
 - 2007-09-12T08-52-31

- 2007-09-12T08-57-15
- For Atlantic scene, granules are:
 - 2007-09-12T10-36-46
 - 2007-09-12T10-41-30
 - 2007-09-12T10-46-14
 - 2007-09-12T10-50-59

One scene is mostly above the South Atlantic while the other crosses Eastern Europe and Africa. The produced SDS radiances, geolocation files, and ancillary data files are in HDF5 format and will be delivered as part of the study deliverables:

- radiance files are named EPS-SG_VII_RAD_granule#_METimCTP_final.he5
- ancillary data files are named EPS-SG_VII_ANCILLARY_granule#_V1.4.he5
- geolocation files are named EPS-SG_VII_GEOLOC_granule#_V1.5.he5

Radiance files only contain radiances for cloudy pixels. Other pixels were not computed.

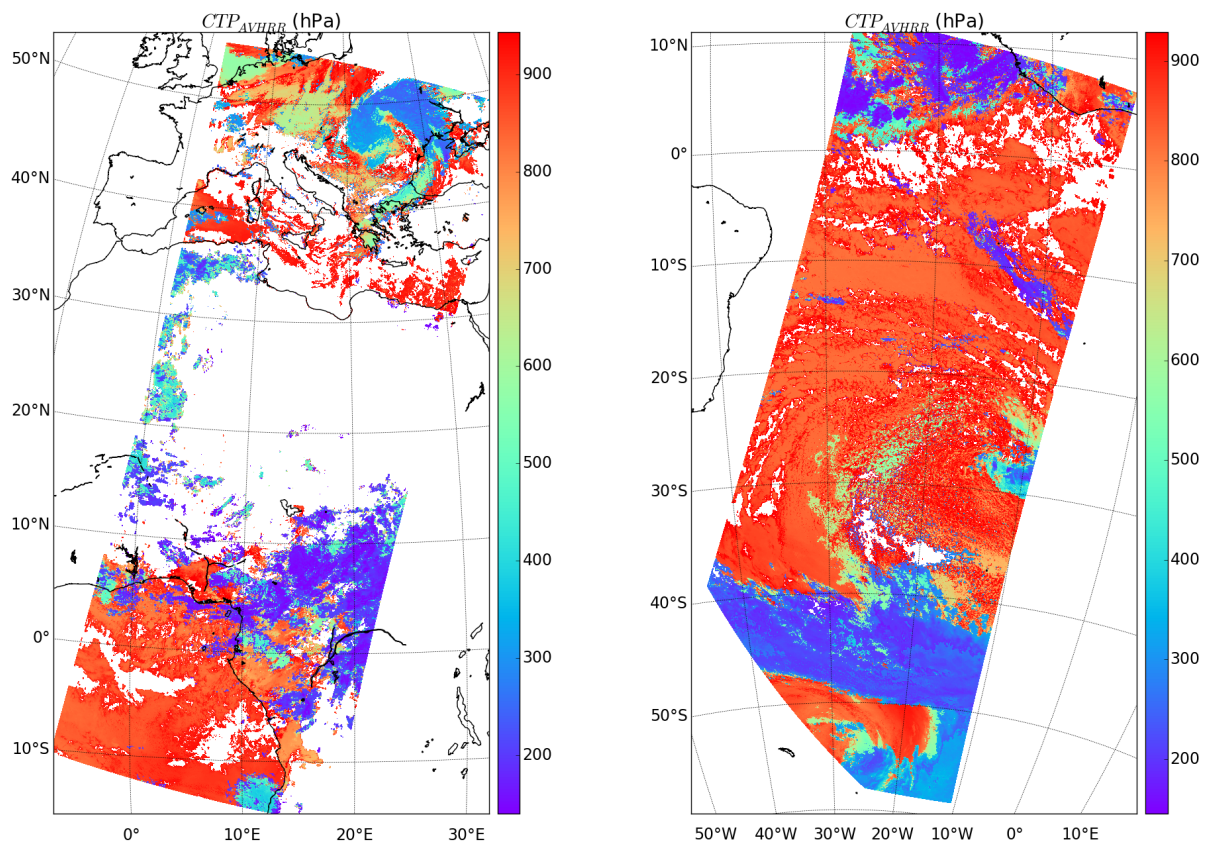


Figure 6.1.3 AVHRR (acha algorithm) CTP used for the SDS.

6.1.2 LUT sampling/interpolation errors

In order to assess LUT interpolation errors due to finite sampling of a given parameter x , we generally choose a single grid point for the other parameters and perform direct computation for a range of x values with a very high resolution (very small steps). We then compare the direct computation to interpolated values from LUTs. To look at interpolation errors for all parameters over their full range would then come back to building a very high resolution LUT to be compared to the working resolution LUT.

Here, we can take an other approach thanks to the SDS simulator. We re-ran the SDS simulator for the two scenes (Europe/Africa and Atlantic) but using the LUTs as the forward model instead of the direct “on-the-fly” use of ARTDECO RT solver in the normal version of the simulator. The differences between the intensities maps $I_{\text{on-the-fly}}$ and the I_{LUT} (either at 670nm or 865nm) and between the signal ratio maps $R_{\text{on-the-fly}}$ and the R_{LUT} (763 nm / 752nm) are LUT interpolation error. The histogram of differences between the “on-the-fly” and “LUT” values over the whole scenes can be seen as the interpolation error over the LUT sample range weighted by the frequency of occurrence of LUT grid points (i.e. combination of sampled values) in a realistic scene.

6.1.2.a High resolution LUTs

Figures 6.1.4 and 6.1.5 show maps and histograms the relative differences $(I_{\text{LUT}} - I_{\text{on-the-fly}})/I_{\text{on-the-fly}}$ and $(R_{\text{LUT}} - R_{\text{on-the-fly}})/R_{\text{on-the-fly}}$ for Atlantic and Europe/Africa scenes. I_{LUT} and R_{LUT} were obtained with “high” resolution LUTs (see Table 3). These relative differences are due to LUT interpolation error. Note that white areas where clouds should be present in the Atlantic scene (figure 6.1.4 mostly at latitudes South of 40°S) are related to LUT out of boundary values for the sun zenith angle (high values of SZA not sampled in LUT) and wind-speed (low wind speed not sampled in the LUT).

We see on histograms that I interpolation errors are lower than ~3% for a vast majority of pixels. The distribution is peaked around ~0 but is not symmetric, over-estimation being more frequent than under-estimation (for which the error is lower than ~1%). Looking at maps, we see that due to the limited angular sampling in the LUT, the error is greater in rainbow geometries. On the other hand, we see that the error is bigger for thinner clouds. This tendency is clearly seen if we look at histograms for clouds with $\text{COT} > 10$ (see Figure 6.1.6). For that thicker clouds, the error on I interpolation drops to less than ~1% for all pixels. Moreover, we see that the error distribution gets back to a symmetric tendency centred on ~0.

We see on histograms that R interpolation error is lower than 0.5% for almost all pixels. The error distribution is symmetric and almost centred on 0. Likewise for I, the R interpolation error is greater in the rainbow and for thinner clouds. We see on Figure 6.1.6, that this error drops to less than ~0.2% for clouds with $\text{COT} > 10$.

As a conclusion, we can say that interpolation error for I are lower than 3% for all clouds and drops to less than 1% for $\text{COT} > 10$. We see a bias toward an over-estimation of I for thinner clouds. The 1% error for thicker clouds especially occurs around special geometries like the rainbow and is then related to the geometry sampling. A way to overcome this problem will be proposed in section 7. For thinner clouds, the interpolation error is rather due to surface parameter (WSA or wind-speed). The interpolation errors on I and R for the “high” resolution LUT sampling are of the same order as the intended bias error (5% threshold, 3% objective) and inter-channel bias (1%) as specified in the EPS-SG system requirement document (EUMETSAT [2013]).

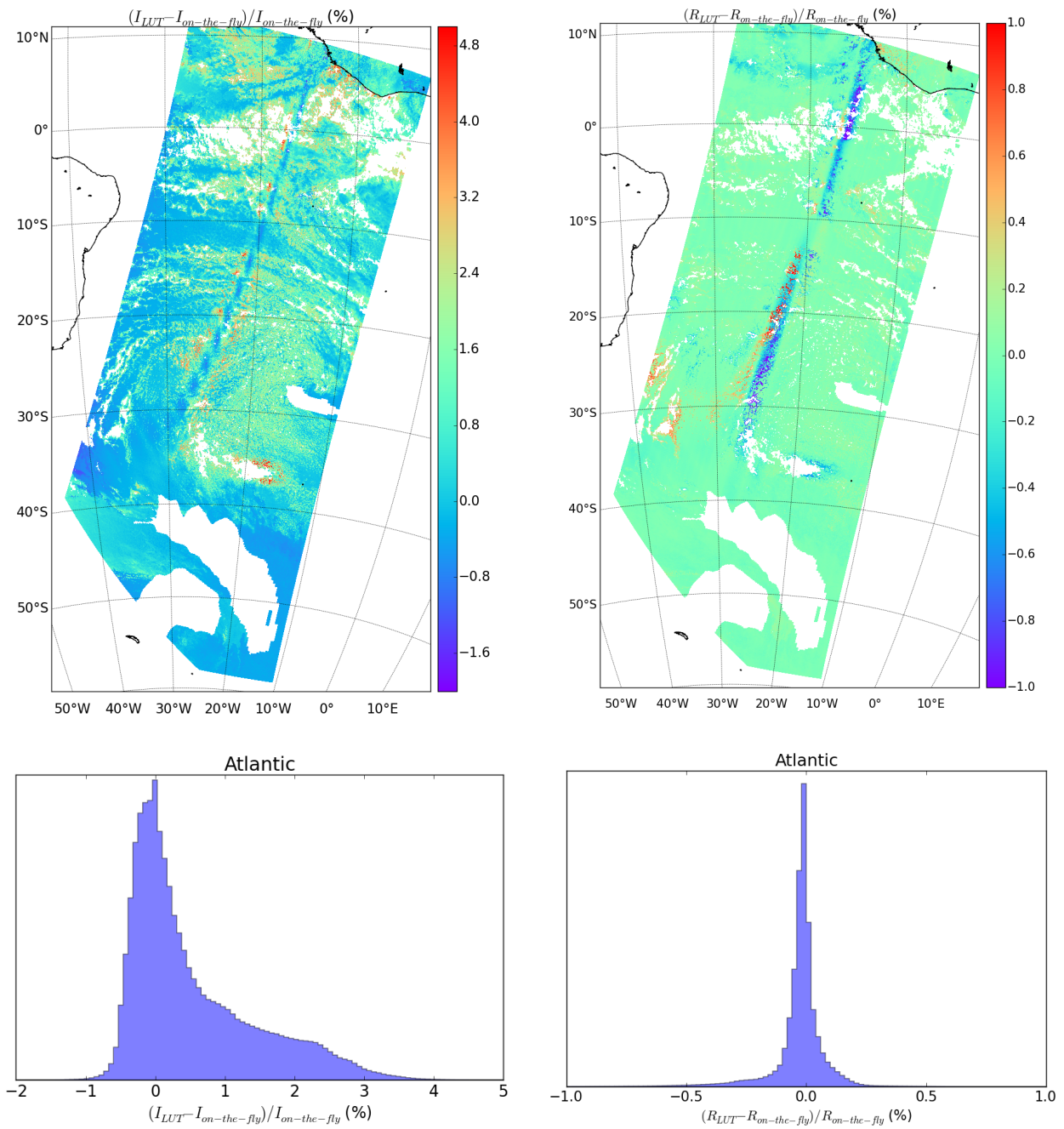


Figure 6.1.4 Maps (upper panels) and histograms (lower panels) of the relative differences $(I_{LUT} - I_{on-the-fly}) / I_{on-the-fly}$ (left panel) and $(R_{LUT} - R_{on-the-fly}) / R_{on-the-fly}$ (right panel) for the Atlantic scene. I_{LUT} and R_{LUT} were obtained with “high” resolution LUTs (see Table 3).

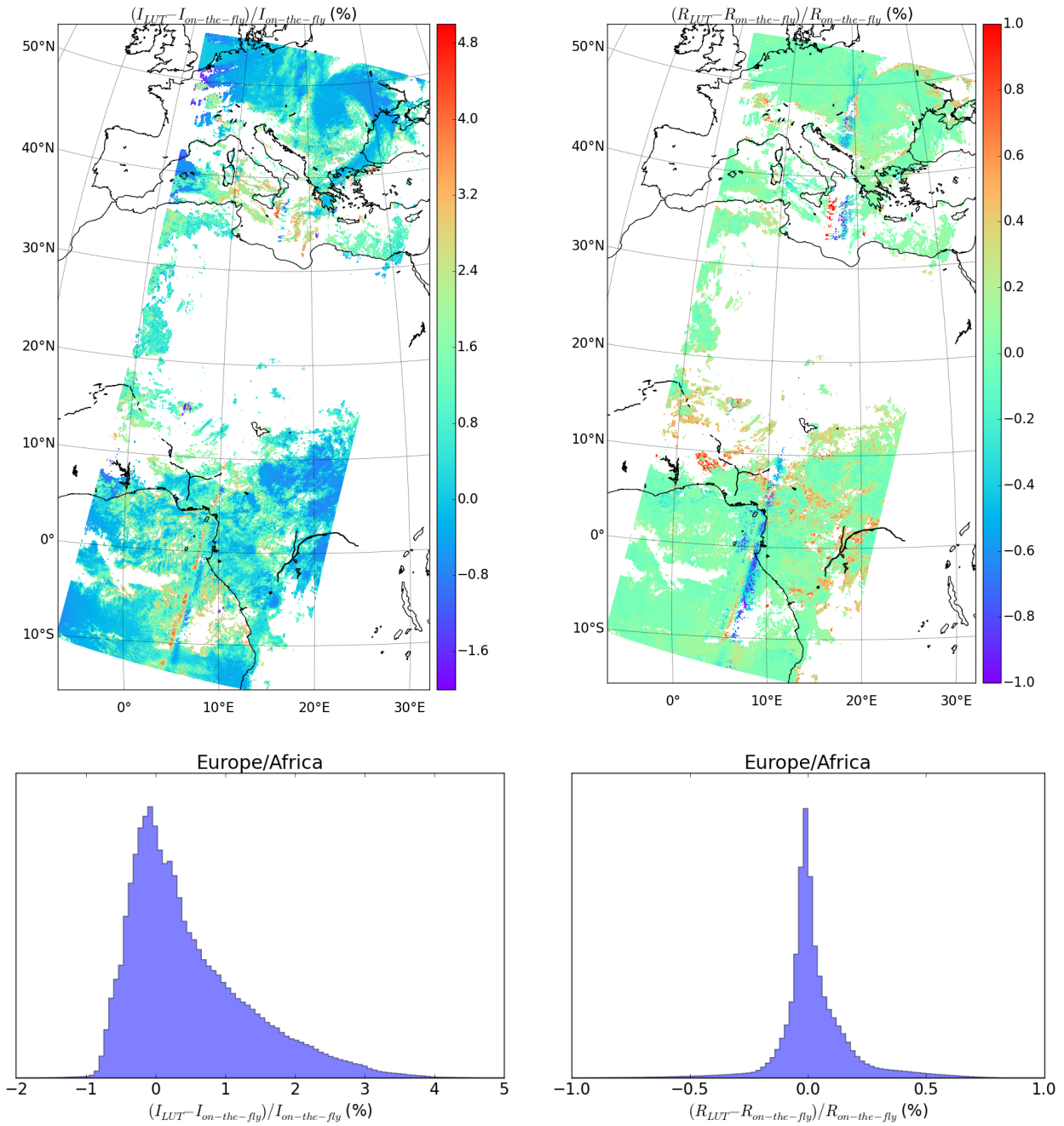


Figure 6.1.5 Maps (upper panels) and histograms (lower panels) of the relative differences $(I_{LUT} - I_{on-the-fly}) / I_{on-the-fly}$ (left panel) and $(R_{LUT} - R_{on-the-fly}) / R_{on-the-fly}$ (right panel) for the Europe/Africa scene. I_{LUT} and R_{LUT} were obtained with “high” resolution LUTs (see Table 3).

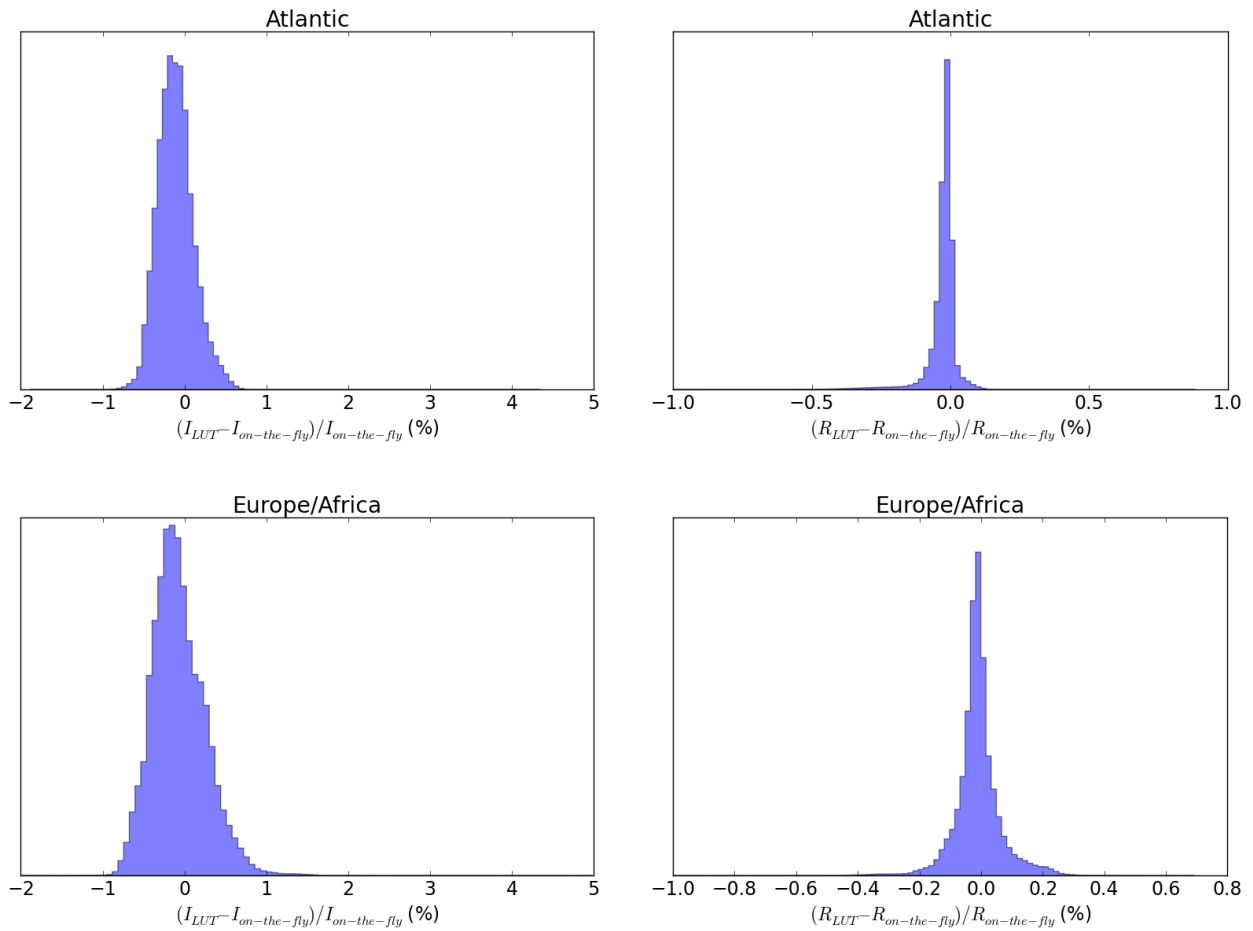


Figure 6.1.6 Histograms of the relative differences $(I_{LUT} - I_{on-the-fly}) / I_{on-the-fly}$ (left panels) and $(R_{LUT} - R_{on-the-fly}) / R_{on-the-fly}$ (right panels) for the Atlantic (upper panel) and Europe/Africa (lower panel) scene. This are obtained by restricting to $COT > 10$. I_{LUT} and R_{LUT} were obtained with “high” resolution LUTs (see Table 3).

6.1.2.b Medium resolution LUTs

Figure 6.1.7 shows the histograms of the relative differences $(I_{LUT} - I_{on-the-fly}) / I_{on-the-fly}$ (left panels) and $(R_{LUT} - R_{on-the-fly}) / R_{on-the-fly}$ (right panels) for the Atlantic (upper panel) and Europe/Africa (lower panel) scenes. I_{LUT} and R_{LUT} were obtained with “medium” resolution LUTs (see Table 3).

We see that the shapes of histograms are similar to the one for the “high” resolution LUTs, but with a greater amplitude. The interpolation error on I is up to $\sim 12\%$ with again a bias toward over-estimation. For $COT > 10$, the error on I drops to less than $\sim 1.8\%$. The error on R is less than $\sim 1\%$ for most pixels and the distribution is rather symmetric (regarding the I error distribution) and centred on ~ 0 . The error drops to less than $\sim 0.5\%$ for $COT > 10$.

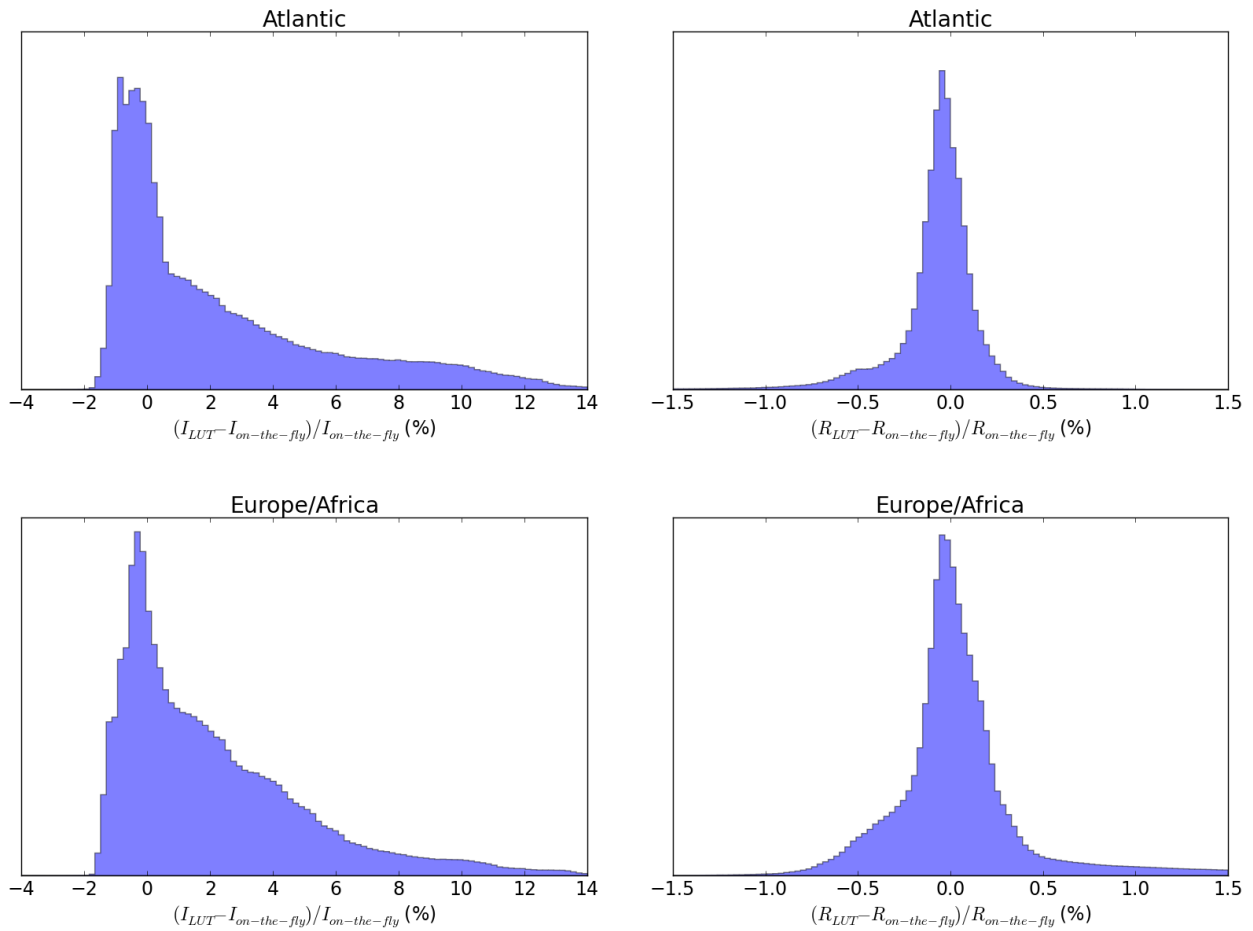


Figure 6.1.7 Histograms of the relative differences $(I_{LUT} - I_{on-the-fly}) / I_{on-the-fly}$ (left panels) and $(R_{LUT} - R_{on-the-fly}) / R_{on-the-fly}$ (right panels) for the Atlantic (upper panel) and Europe/Africa (lower panel) scenes. I_{LUT} and R_{LUT} were obtained with “medium” resolution LUTs (see Table 3).

6.1.3 COT, CTP retrieval

In that section, we compare the COT and CTP obtained with the day-1 algorithm to the AVHRR cloud products that are used to create the SDS. Of course, we perform the retrieval on SDS created with the “on-the-fly” version of the simulator. We then remind that in that case, the obtained discrepancies between the OE retrieval products and original AVHRR products are due to propagation of the LUT interpolation error.

6.1.3.a High resolution LUTs

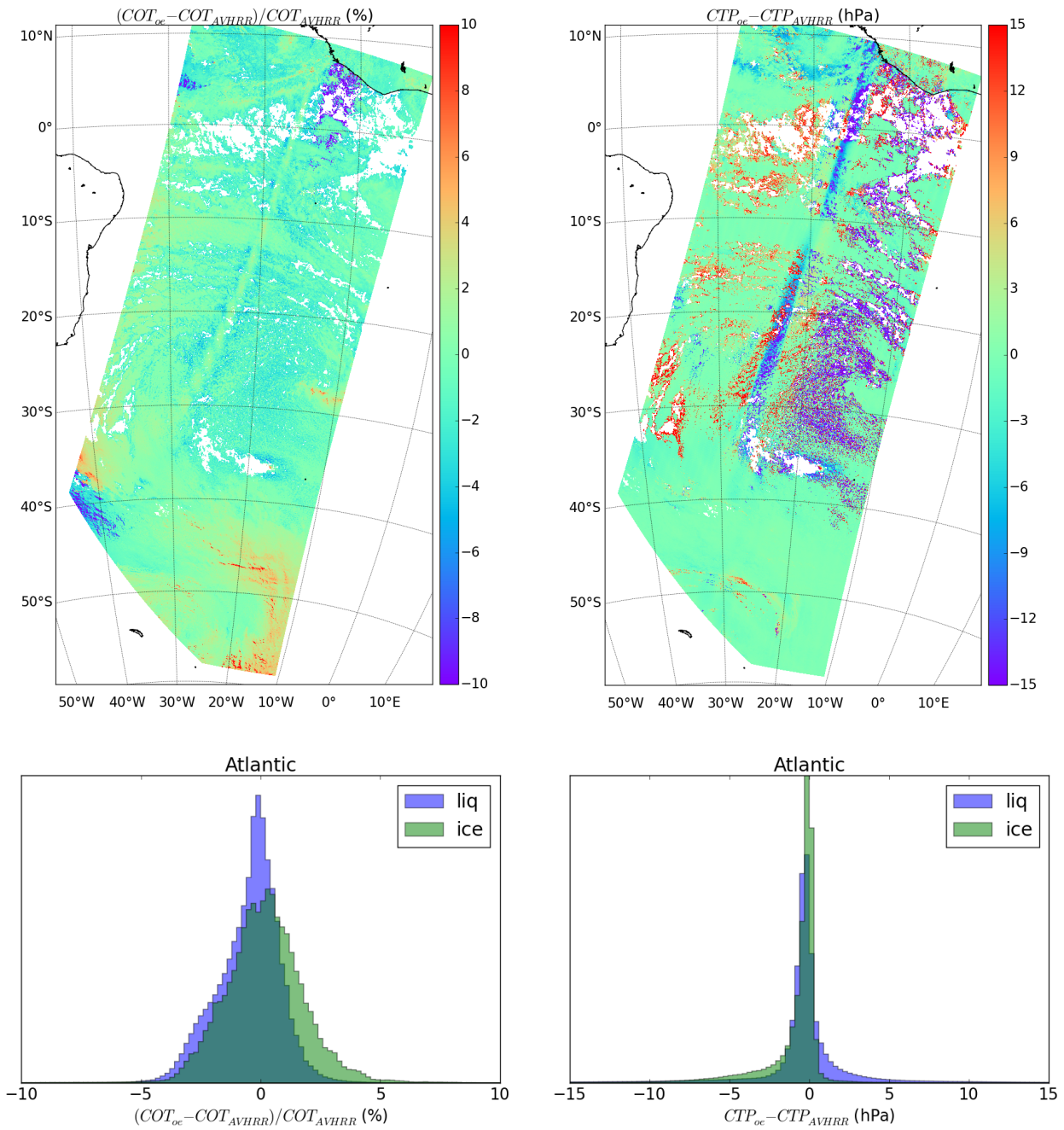


Figure 6.1.8 Maps (upper panels) and histograms (lower panels) of the relative difference $(COT_{OE} - COT_{AVHRR}) / COT_{AVHRR}$ (left panel) and absolute difference $CTP_{OE} - CTP_{AVHRR}$ (right panel) for the Atlantic scene. Retrieval was performed using the “high” resolution LUTs (see Table 3).

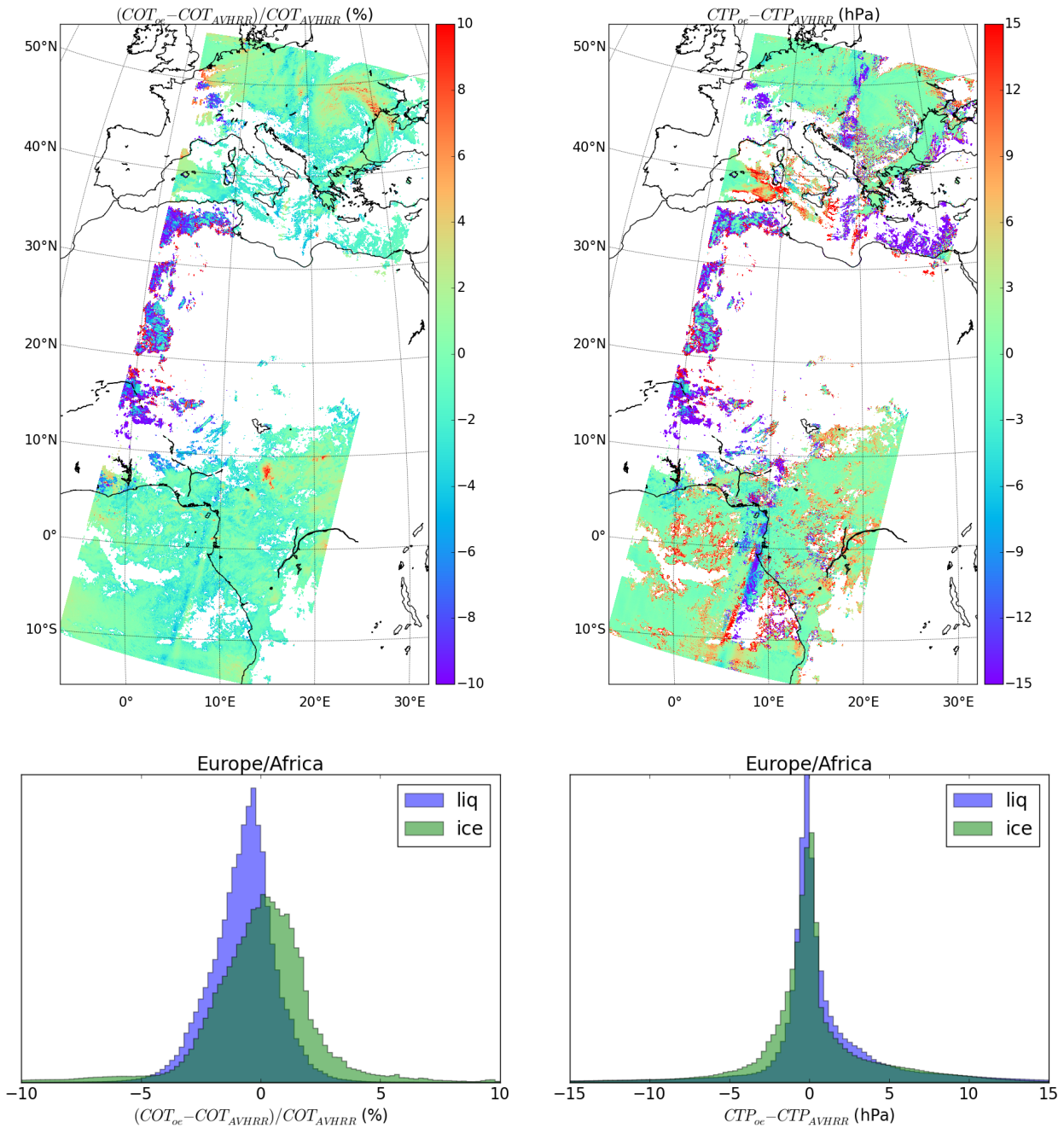


Figure 6.1.9 Maps (upper panels) and histograms (lower panels) of the relative difference $(COT_{OE} - COT_{AVHRR}) / COT_{AVHRR}$ (left panel) and absolute difference $CTP_{OE} - CTP_{AVHRR}$ (right panel) for the Europe/Africa scene. Retrieval was performed using the “high” resolution LUTs (see Table 3).

Figures 6.1.8 and 6.1.9 show maps and histograms of the relative difference $(COT_{OE} - COT_{AVHRR}) / COT_{AVHRR}$ and absolute difference $CTP_{OE} - CTP_{AVHRR}$ for the Atlantic and Europe/Africa scenes. Retrieval was performed using the “high” resolution LUTs (see Table 3).

We see that for most pixels, the relative COT error is less than ~5%. The error distribution is rather symmetric and almost centred on 0. However, the error distribution for liquid clouds is slightly narrower and

shifted toward lower COT estimate. The error on COT estimate can get high over bright surfaces (glitter and desert) for thin clouds. In this case, it propagates into a higher CTP error (even for pixels where the interpolation error on R was rather small). Error on COT can also be greater for higher opacity clouds because the intensity is then not very sensitive to COT. In this case, the propagation on CTP error is not significant. We see that the error raises in the rainbow geometry.

The error on CTP is less than ~10hPa for most of the pixels for the Europe/Africa scene and less than ~5hPa for the most pixels in the Atlantic scene. The distribution are rather symmetric and almost centred on 0 except for the ice clouds in Atlantic scene where the retrieved CTP tends to be slightly biased toward smaller values. The error is getting bigger over bright surfaces (glitter or desert) and for thinner clouds. For clouds with COT >10, the CTP error drops to less than ~5hPa for the Europe/Africa scene and less than ~3hPa for the Atlantic scene. We see that the error raises in the rainbow direction again.

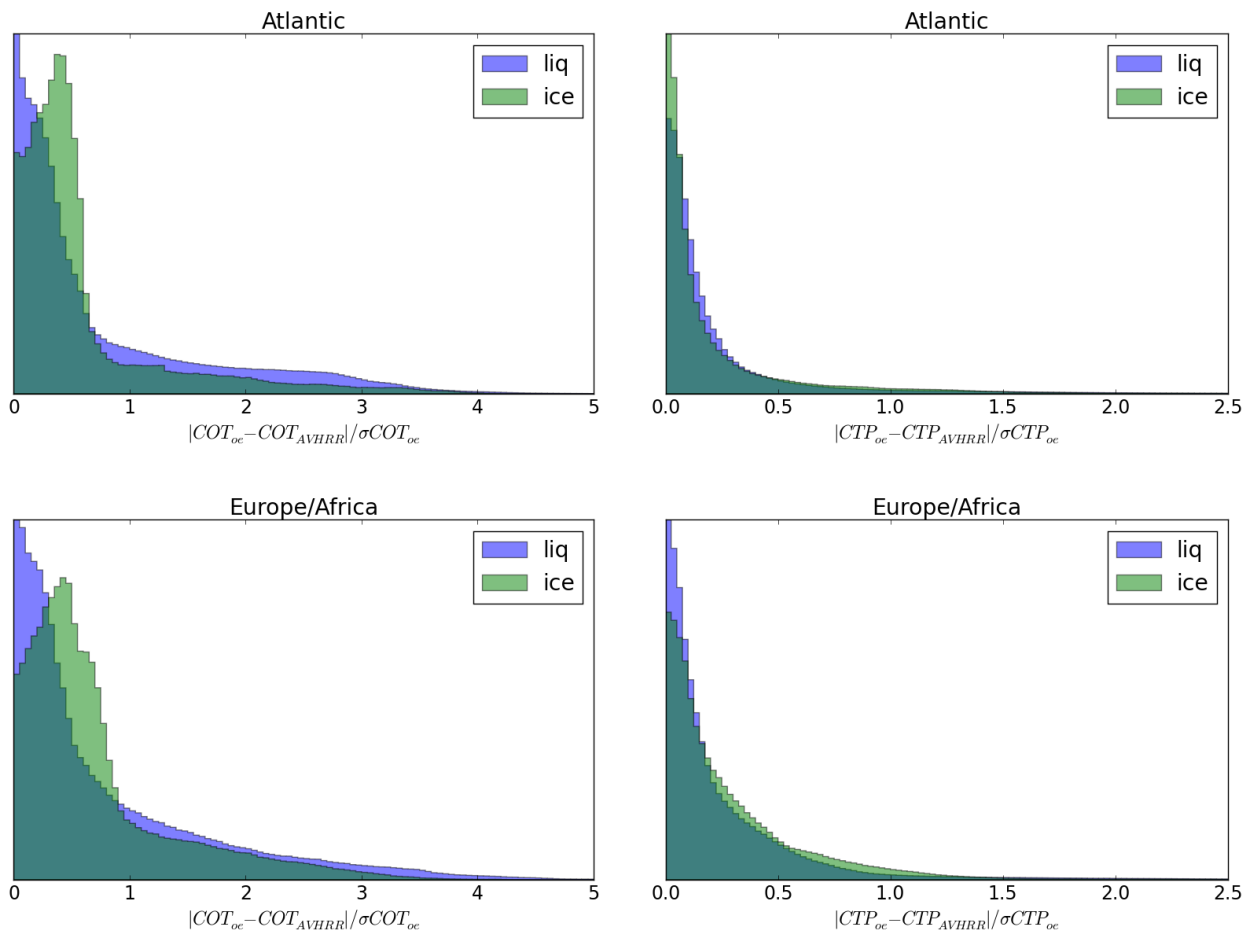


Figure 6.1.10 Histogram of the error on the OE retrieval $COT_{OE} - COT_{AVHRR}$ (left panel) and $CTP_{OE} - CTP_{AVHRR}$ (right panels) normalized by the OE estimated uncertainties (σCOT_{OE} and σCTP_{OE}) for the Atlantic scene (upper panels) and Europe/Africa scene (lower panel).

As a product of the OE retrieval, we have the estimation of the product uncertainty (standard deviation). In the present case, $S_e = S_i$ in input because the only source of error in the retrieval regarding the SDS

radiances is the LUT interpolation error (see section 5.3 for details about S_ϵ). The interpolation errors used in defining S_i are the one estimated in section 6.1.2.a. Figure 6.1.10 shows histograms of the error on the OE retrieval $COT_{OE} - COT_{AVHRR}$ and $CTP_{OE} - CTP_{AVHRR}$ normalized by the OE estimated uncertainties (standard deviation: σCOT_{OE} and σCTP_{OE}) for the Atlantic scene and Europe/Africa scene. We see that the OE uncertainties on retrieved COT and CTP are quite representative of the actual error since for most pixels the AVHRR value is within 3σ of the OE retrieved value.

We do not show results for the cost function and number of iterations. In the present case, the cost function is very low and the number of iterations is one for most of the pixels. The first guess usually falls close to the final retrieval.

6.1.3.b High resolution LUTs with noisy and biased data

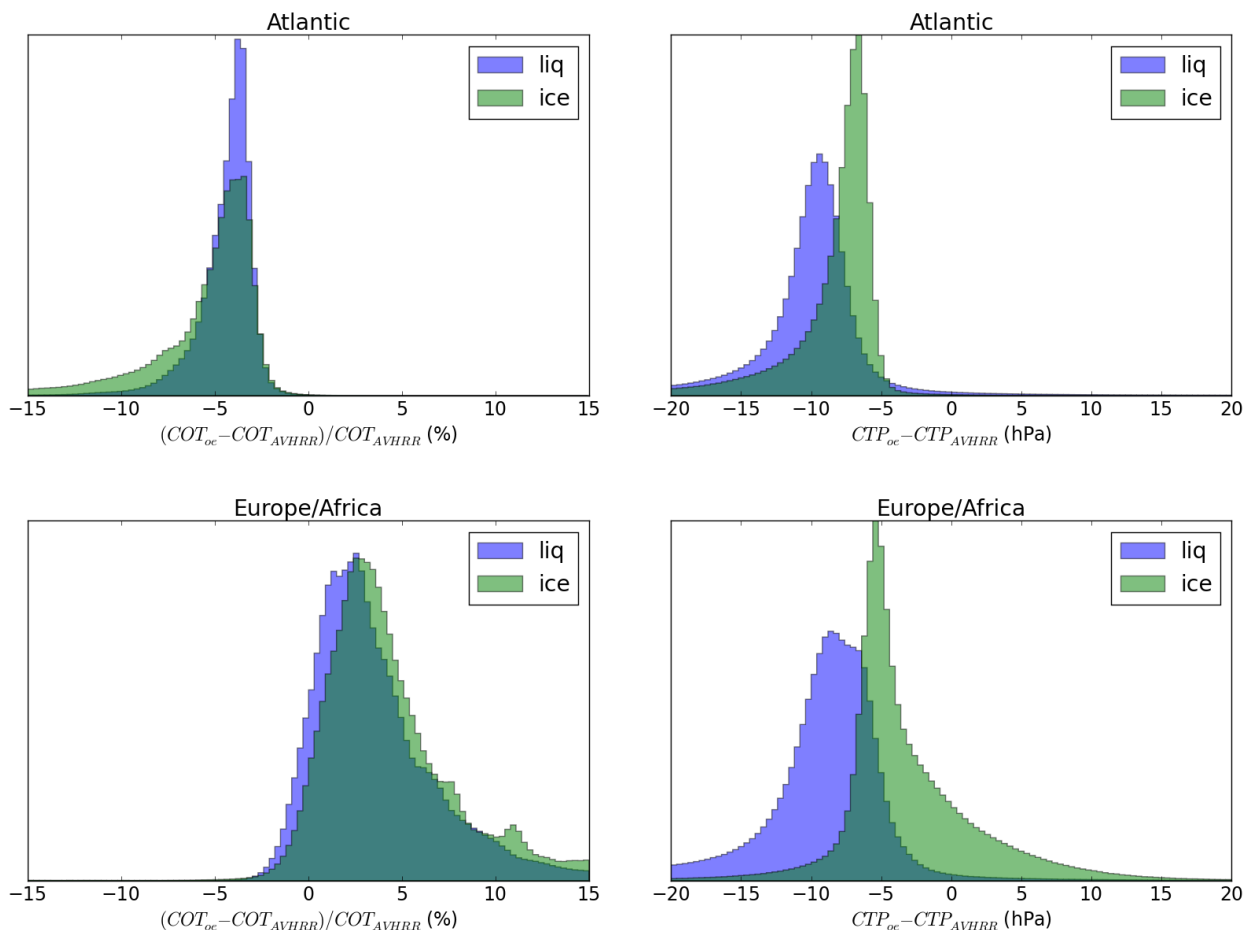


Figure 6.1.11 Histograms of the relative difference $(COT_{OE} - COT_{AVHRR}) / COT_{AVHRR}$ (left panel) and absolute difference $CTP_{OE} - CTP_{AVHRR}$ (right panel) for the Atlantic scene (upper panels) and Europe/Africa scene (lower panels). Retrieval was performed using the “high” resolution LUTs (see Table 3) on SDS data in which noise and biases were added.

In the present section, we study the impact of the noise and bias on data for the retrieved values. We perform

the same exercise as in the previous section (6.1.3.a) using SDS to which we added noise and bias as follow:

- We add Gaussian noise to all channels. The standard deviation for the noise intensity distribution is given by the breakthrough signal to noise ratio multiplied by typical intensity given for all channels in the system requirement document (see EUMETSAT [2013]).
- We apply an inter-band bias of 0.5% by multiplying the SDS signal ratio (VII-5/VII-4) by 1.005.
- We apply an absolute bias of 2% on VII-3 and VII-6 channels intensities by multiplying those by 1.02 for the Europe/Africa scene and 0.98 for the Atlantic scene.

Figure 6.1.11 shows the resulting histograms of the relative difference $(COT_{OE} - COT_{AVHRR}) / COT_{AVHRR}$ and absolute difference $CTP_{OE} - CTP_{AVHRR}$ for the Atlantic scene and Europe/Africa scene. As expected, distributions are larger than without noise. The inter-band bias of +0.5% on the signal ratio causes a bias toward lower retrieved CTP of about 6hPa (for ice clouds) to about 10hPa (for liquid clouds) for the peak of the distribution. This bias is similar in the two scenes. For the Europe/Africa scene (+2% absolute intensity bias) the peak of the distribution is shifted toward higher COT by 2-3%. For the Atlantic scene (-2% absolute intensity bias) the peak of the distribution is shifted toward smaller COT by 3-4%. The shape of the distribution also tends to be modified mostly because the sensitivity of I regarding COT is different across the COT range.

6.1.3.c Medium resolution LUTs

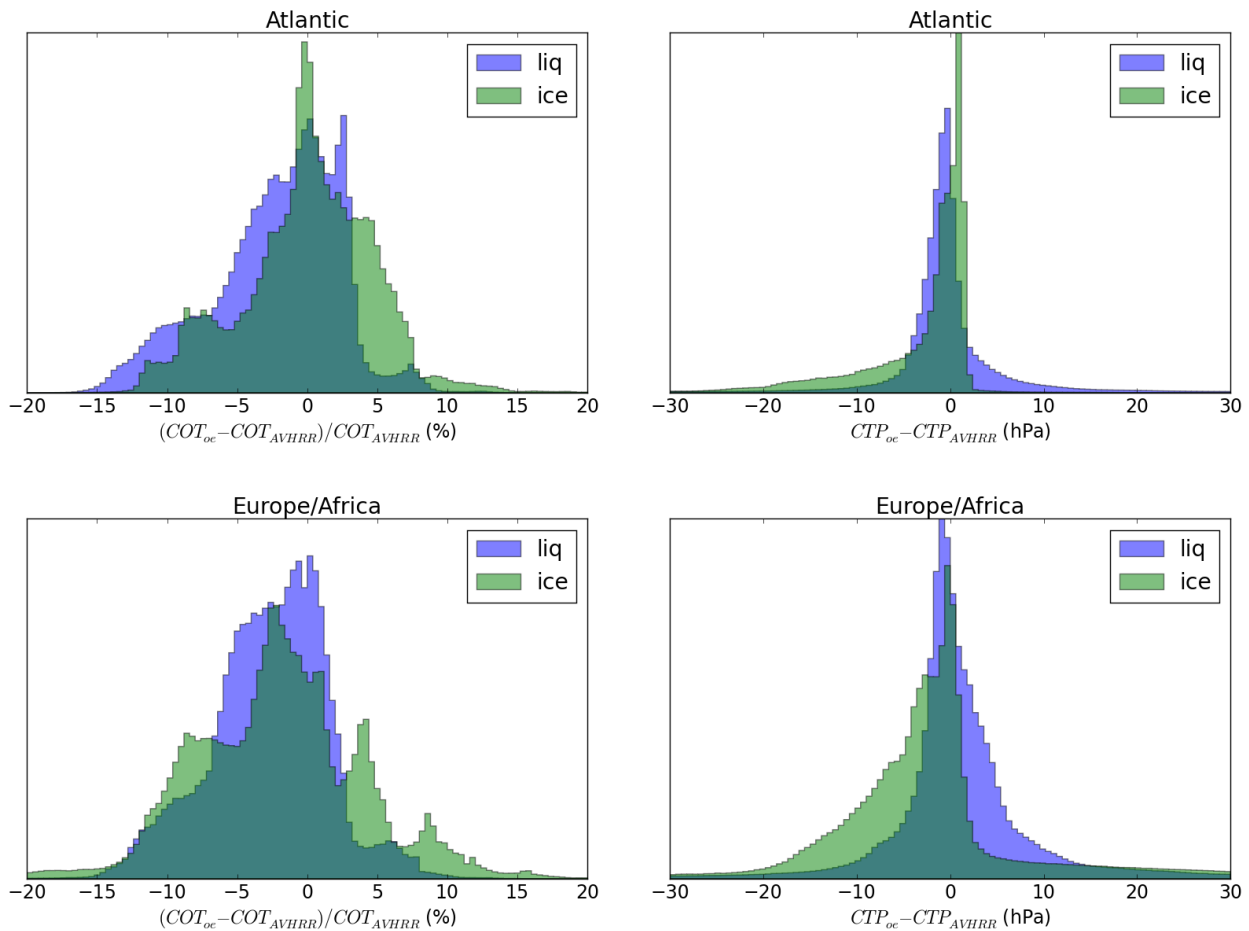


Figure 6.1.12 Histograms of the relative difference $(COT_{OE} - COT_{AVHRR}) / COT_{AVHRR}$ (left panel) and absolute difference $CTP_{OE} - CTP_{AVHRR}$ (right panel) for the Atlantic scene (upper panels) and Europe/Africa scene (lower panels). Retrieval was performed using the “medium” resolution LUTs (see Table 3).

Figure 6.1.12 shows histograms of the relative difference $(COT_{OE} - COT_{AVHRR}) / COT_{AVHRR}$ and absolute difference $CTP_{OE} - CTP_{AVHRR}$ for the Atlantic scene and Europe/Africa scene. Here the retrieval was performed using the “medium” resolution LUTs (see Table 3).

As expected, the error distribution gets larger regarding the results obtained with “high” resolution LUTs. For COT, the error is up to ~20%. We see multi-modes in the COT error distribution that may be related to the sampling. The CTP error is <30 hPa for most pixels. The distribution of CTP error remains rather symmetric for liquid clouds while a bias toward smaller CTP appears for ice clouds. Note that for clouds with $COT > 10$, the error on CTP drops to less than ~10hPa.

6.1.3.d Medium resolution with climatological cloud vertical structure LUTs

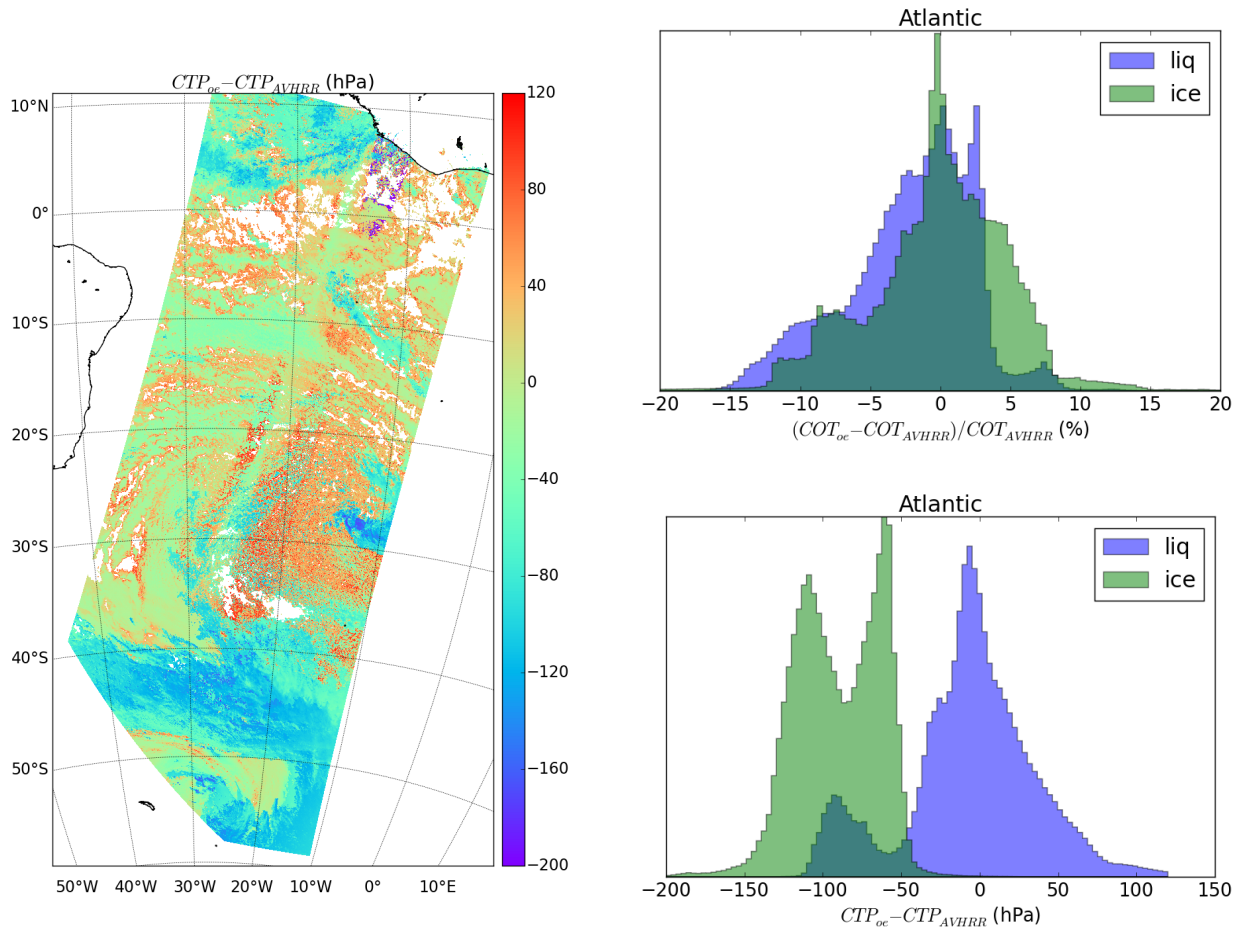


Figure 6.1.13 Map of $CTP_{OE} - CTP_{AVHRR}$ and histograms of the relative difference $(COT_{OE} - COT_{AVHRR}) / COT_{AVHRR}$ and absolute difference $CTP_{OE} - CTP_{AVHRR}$ for the Atlantic scene. Retrieval was performed using the “medium” resolution LUTs (see Table 3) with a climatological cloud vertical structure.

In the present section, we test the bias introduced by a wrong representation of the cloud vertical structure. The inversion is performed on the same SDS, for which homogeneous vertical profile with constant CGT=1.0km is used. However, we use LUTs produced with vertical cloud structure climatology (see section 5.1).

Figure 6.1.13 shows histograms of the relative difference $(COT_{OE} - COT_{AVHRR}) / COT_{AVHRR}$ and absolute difference $CTP_{OE} - CTP_{AVHRR}$ for the Atlantic scene and Europe/Africa scene. The error distribution on COT is not modified regarding the used of the right cloud vertical structure. That is expected because the vertical structure has no impact on the intensity. As already discussed in section 4, the bias on CTP retrieval caused by the misrepresentation of the vertical structure of the cloud is important and not only for thinner clouds. We see that the bias introduced is up to 150hPa. The bias on ice clouds is systematically toward smaller values of CTP. Most of the ice cloud on the scene will be represented within the LUT model with a CGT > 1.0km and a vertical extinction profile that roughly increases from the top of the cloud to the centre. To obtain the same signal ratio as the homogeneous cloud with CGT=1.0km used in the SDS, one needs to

place the cloud top at higher altitude (lower pressure) because photons penetration is greater in the non-homogeneous cloud.

Note that the OE estimated uncertainties does not reflect the huge bias because the covariance used in input (S_{ϵ}) for the retrieval does not account for the impact of vertical structure discrepancy.

This results does not exactly show the improvement of a retrieval with implicit account of cloud vertical structure (gain of LUT with implicit variation of CGT versus LUT with implicit fixed value of CGT). But it shows the important difference of the optimal estimation result with and without a physical relaxation of CGT. It thus demonstrates the importance of CGT, and for not generating synthetic data with fixed CGT.

6.2 MERIS data

In that section, we describe the testing of the Day-1 algorithm against MERIS data. For that exercise, we use “medium” resolution LUTs with cloud vertical profile climatology as the forward model in the OE. The production of a set of “high” resolution LUTs would have been too long regarding the time scales for the end of the study. On the other hand, the “medium” resolution is sufficient for the present testing considering the other sources of discrepancies between our products and the MERIS L2 operational products (differences in cloud model especially)

6.2.1 Data description

Thanks to the similarities in filter positions, MERIS data are well suited for testing of our Day-1 “METimage algorithm”. MERIS is described in section 2.3. We choose four MERIS orbits that cover part of Western Europe, Africa and Southern Atlantic (see Figure 6.2.1). Two orbits are in February 2003 and two are in August 2003:

- 20030815_101204_000026312019_00051_07620_0000
- 20030824_103018_000026302019_00180_07749_0000
- 20030205_102440_000026032013_00323_04886_0000
- 20030215_100910_000026032013_00466_05029_0000

We will compare the outputs of our Day-1 algorithm to the MERIS L2 operational retrieval product. We host all MERIS L1b 3rd reprocessing at HYGEOS and we retrieved L2 products from ICARE thematic centre (<http://www.icare.univ-lille1.fr/>).

The required auxiliary data for our retrieval are:

- the ozone column that we get in MERIS L1b data file. We perform an ozone absorption correction on all used channels by assuming that the ozone absorption is decoupled from the rest of the atmosphere. The ozone opacity corresponding to 1000DU is set to 0.00992 for channel 10 and 0.00740 for channel 11.
- The wind speed that we get from MERIS L1b data file.
- The sea level pressure and digital elevation model that are taken from MERIS L1b data file.
- The surface IGBP classification. We use the MODIS product MCD12C1 (https://lpdaac.usgs.gov/dataset_discovery/modis/modis_products_table/mcd12c1). The product is originally on a Climate Modeling Grid (CMG global) with 0.05° resolution. We re-grid it to MERIS L1b grid.
- The surface white sky albedo. We use the globalbedo (<http://www.globalbedo.org>) product that provides the albedo in the visible range for 8-days synthesis. The surface albedo is then not exactly the one for the MERIS band but this is sufficient for our testing. The product is originally on global scale with 0.05° resolution. We re-grid it to MERIS L1b grid.
- A cloud mask that we create from the MERIS L1b data with the VISAT tool (<http://www.brockmann-consult.de/cms/web/beam/>). The cloud mask is saved in HDF5 format.

The MERIS L1b and L2 together with the ancillary data projected to the MERIS grid are included in deliverables. For the MERIS orbit 20030815_101204_000026312019_00051_07620_0000, the following files are present:

- GlobAlbedo_20030815_101204_000026312019_00051_07620_0000.he5 for the visible range white sky surface albedo
- LCT_20030815_101204_000026312019_00051_07620_0000.he5 for the IGBP surface type
- MER_RR__1PRACR20030815_101204_000026312019_00051_07620_0000.N1_cloud.h5 for the cloud mask
- MER_RR__1PRACR20030815_101204_000026312019_00051_07620_0000.N1 as L1b data
- MER_RR__2PRACR20030815_101204_000026312019_00051_07620_0000.N1 as L2 data



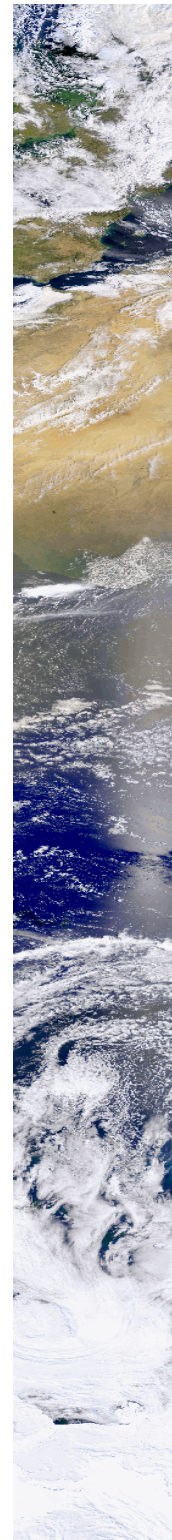
2003-08-24



2003-08-15



2003-02-15



2003-02-05

Figure 6.2.1 RGB representation for MERIS orbits that were used for testing of the Day-1 algorithm. In order for it to fit the page, these RGB pictures were squeezed in the vertical direction (The original data are ~1100 x 15000 pixels).

In order to better match the assumptions and method of the MERIS L2 operational retrieval (see section 2.3.1 and Preusker et al. [2010]), we only use the liquid phase and the (753nm, 761/753nm) as the measurement vector for our OE retrieval. For the S_e covariance matrix setting, we consider:

- An absolute bias of 4% on reflectance and inter-band bias of 1% for the setting of S_y .
- A LUT interpolation error of 7.0% on I and 0.8% on R for S_i .
- A 0.3% relative uncertainty on P_{surf} , 10% relative uncertainty on wind-speed, 10% relative uncertainty for WSA and 0.25 degree absolute uncertainty on geometry (view and sun) for the setting of S_f . Note that, we compute S_f only once for the following parameters (COT =10, CTP = 500.0hPa, $W_{spd} = 5.0$ m/s, WSA = 0.2, $P_{surf} = 1013.0$ hPa, $sza = 50.0^\circ$, $vza = 20^\circ$, $raa = 94.0^\circ$)

Before the inversion, we apply the stray light correction on the channel 11 as described by Lindtrot et al. [2010]. This correction is applied in the operational MERIS retrieval (see Preusker et al. [2010]). As already mentioned, we do not manage the smile effect that results in a variability of the filters central wavelength across the detectors for all MERIS channels. The smile is not so problematic for channel 10 but is critical for channel 11 due to the O₂ absorption. The proper treatment of the smile effect would require to add a LUT axis for the central wavelength of channel 11 and include it as a non-retrieved parameter. This is beyond the scope of the present testing. Despite the treatment of the smile effect, we perform the OE retrieval on all pixels of the image to assess test the global behavior of the algorithm on full dataset. We present the result for the whole retrieval and the results when restricting to the pixels for which the central wavelengths of channel 11 is equal to the one used for the LUT building.

6.2.2 Results for OE COT, CTP retrievals

First of all, the Day-1 algorithm retrieval performed without any human intervention on the 4 orbits. The vast majority of pixels were successfully retrieved. The algorithm then appears to be very robust on real data.

Figures 6.2.2 and 6.2.3 show the scatter plots and histograms of relative difference between OE COT and MERIS L2 COT for the four orbits. We see that for most of the pixels, the COT retrieved with the OE matches to about $\pm 50\%$ the one from the MERIS L2 operational product. A bias of few percent toward smaller COT is seen in our OE retrieval compare to MERIS L2 at the peak of the relative difference distribution. Discrepancies between the two retrievals is not surprising since cloud model are different. For example, we fix the effective radius of cloud droplets in our retrieval while it varies in MERIS L2. Note that the tendency observed here for the whole pixels is the same when restricting to the pixels with channel 11 central wavelengths matching the LUT one. That is normal since the COT is constrained by the channel 10 intensity.

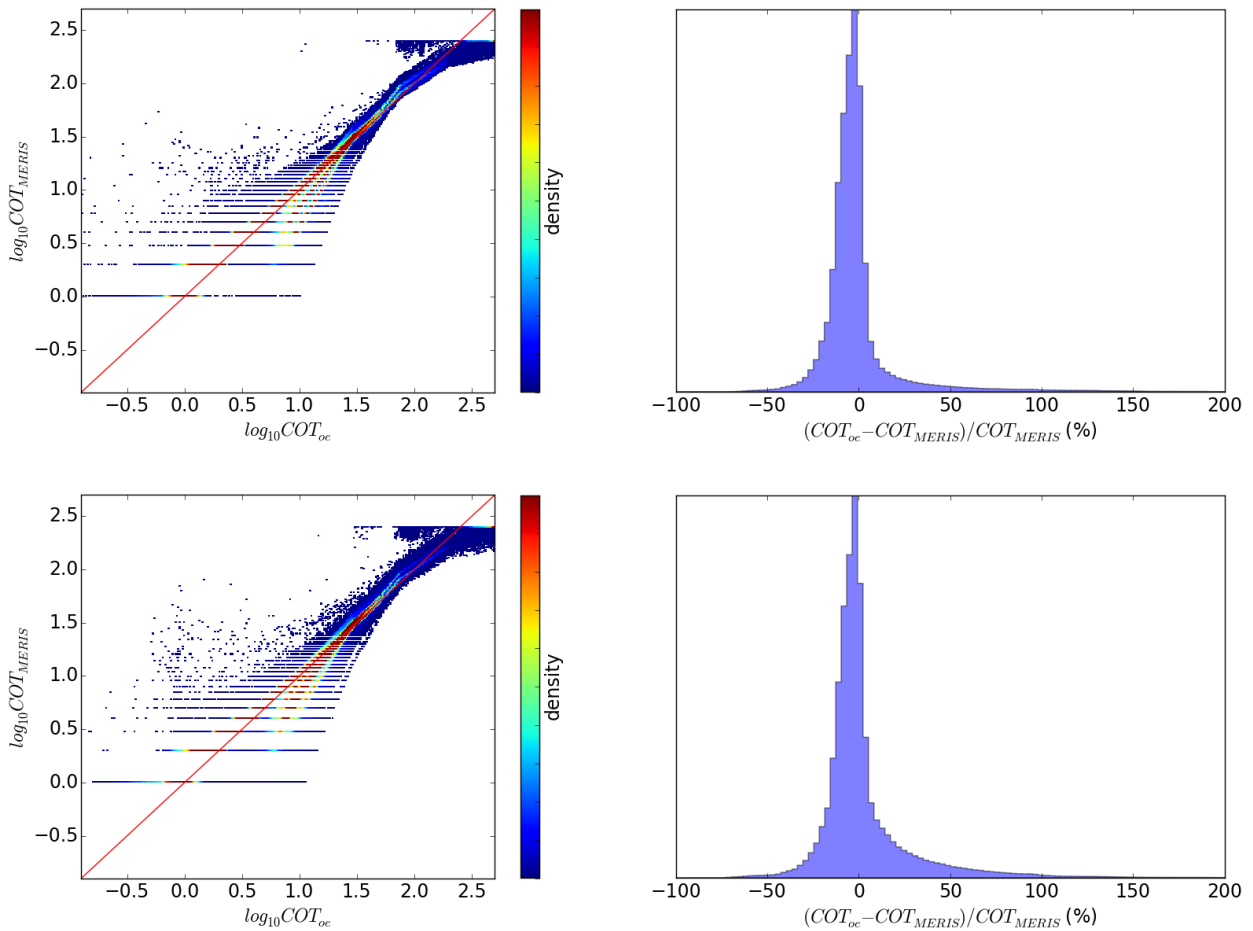


Figure 6.2.2 Scatter plots and relative difference histograms of OE COT versus MERIS l2 COT product for the whole August 2003 orbits. Upper panel is for orbit on 24th and lower panel is for the orbit on the 15th.

In the February orbits (figure 6.2.3), we see points with COT_{MERIS} in the range 3-30 that are retrieved in the range 0.1-1 with our algorithm. These points lie in unmasked glitter direction. The glitter is not account for in MERIS L2. High values of reflectance in glitter's direction are then interpreted as high COT. The same effect is not seen in August orbits because of lower glitter contribution.

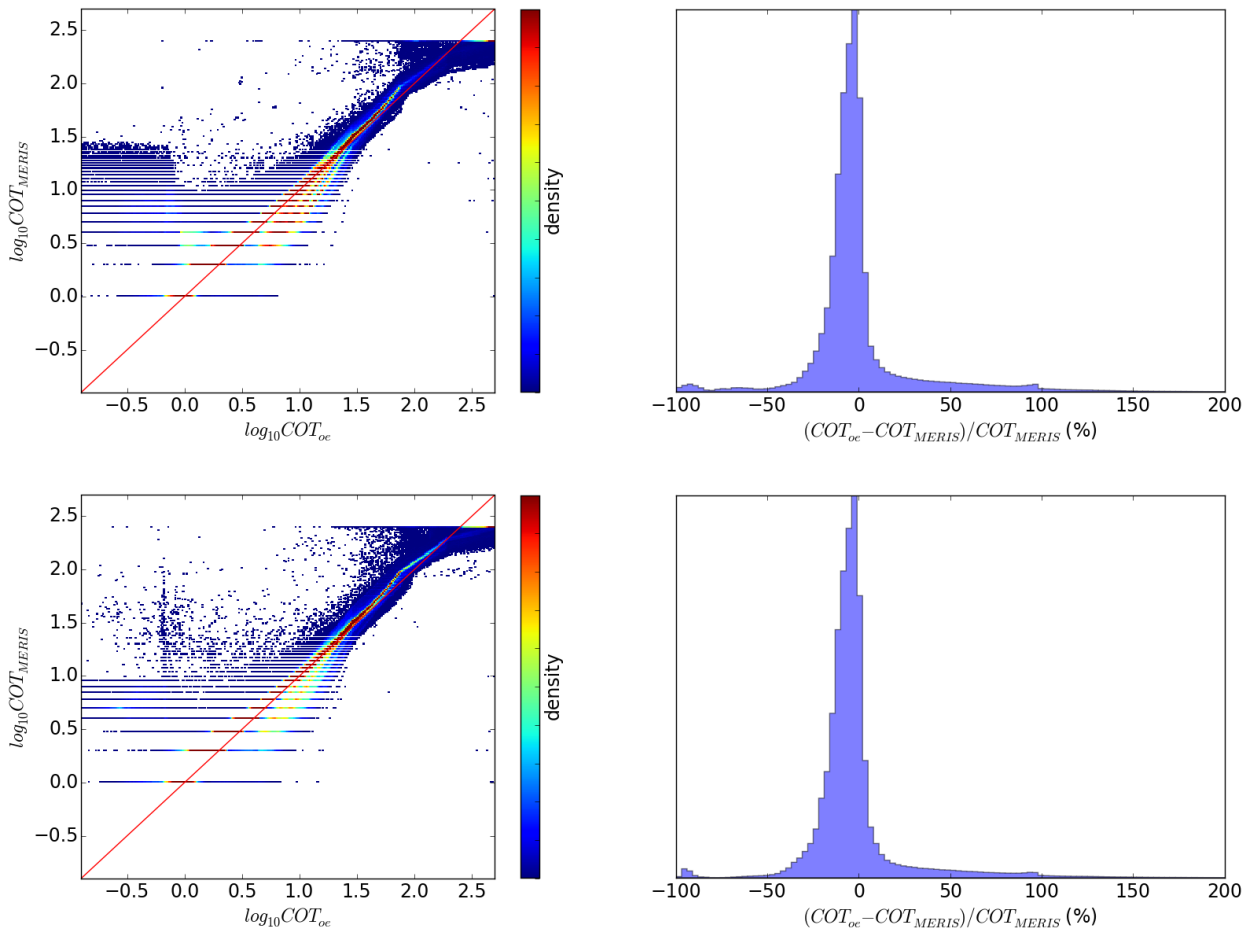


Figure 6.2.3 Scatter plots and relative difference histograms of OE COT versus MERIS L2 COT product for the whole February 2003 orbits. Upper panel is for orbit on 15th and lower panel is for the orbit on the 5th.

Figures 6.2.4 and 6.2.5 show scatter plots of OE CTP versus MERIS L2 CTP for the four orbits. It shows the scatter plots either for all pixels and for pixels that match the MERIS-11 channel central wavelengths used in our LUT building to $\pm 0.01\text{nm}$. We see that to filter the pixels to only have the one with the good wavelength (i.e. account for the smile effect) reduce the dispersion a lot. Our Day-1 algorithm tends to place high level clouds (CTP less than ~ 700 hPa) higher than MERIS L2. This can be explained by the fact that in our algorithm for a given COT the CGT increases as the altitude increase (CTP decrease). The photon path being greater (resulting in a lower $R=761/753\text{nm}$) for a greater CGT, the cloud needs to be placed at higher altitude (lower CTP) to reproduce the same $R=761/753\text{nm}$. On the other hand, our algorithm tends to place clouds with $\text{CTP} > 800\text{hPa}$ at lower altitude regarding MERIS L2.

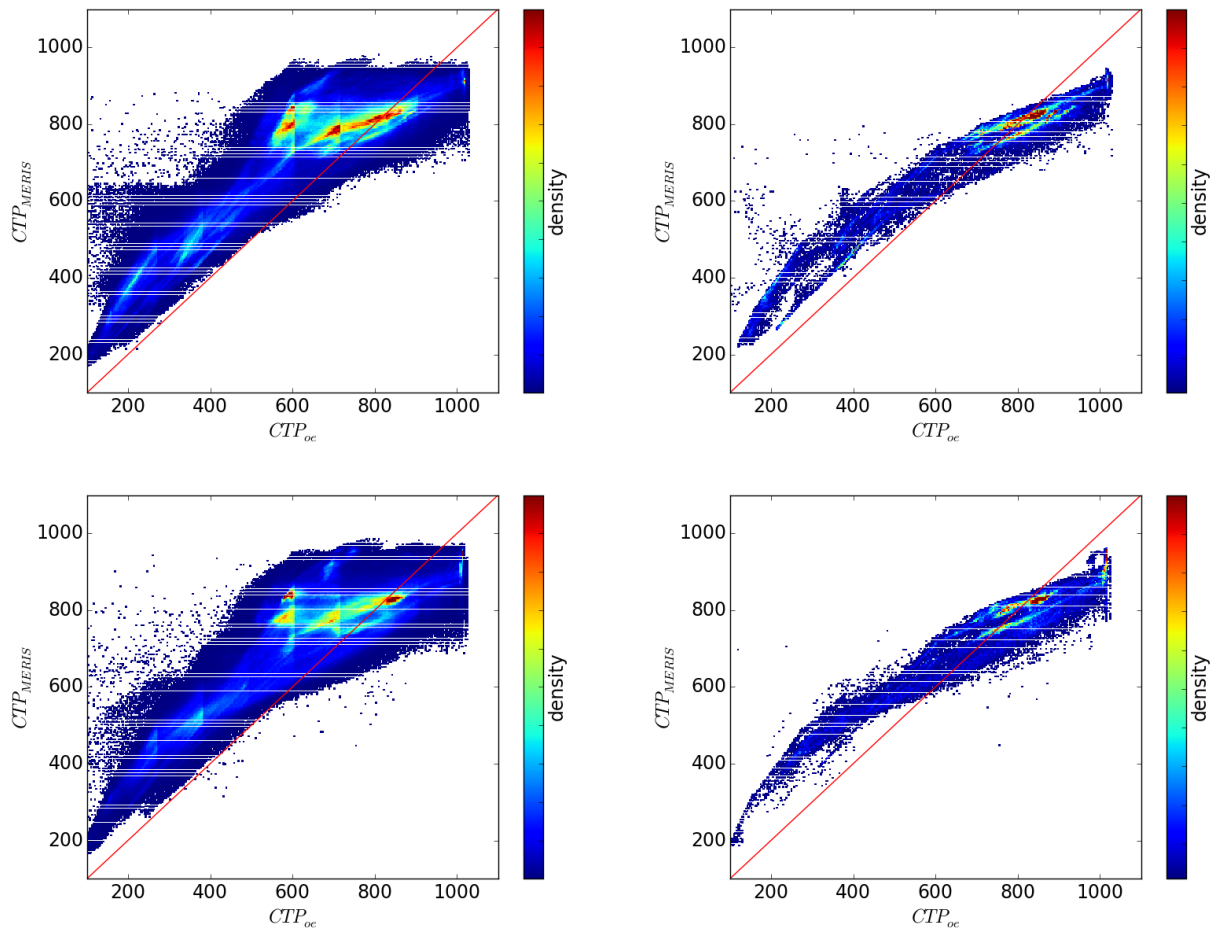


Figure 6.2.4 Scatter plots of OE CTP versus MERIS I2 CTP product for the August 2003 orbits. Upper panels is for orbit on 24th and lower panels is for the orbit on the 15th. The left panels are for the all pixels while the right panels are for pixels that match the MERIS-11 channel central wavelengths used in our LUT building (761.875nm) to ± 0.01 nm.

Again, the discrepancy between the two CTP retrieval is not surprising since the cloud physical model used in those are different. As shown in section 6.1.3.d, the impact of the cloud vertical structure used in the forward model is critical and can bring bias up to ~ 150 hPa.

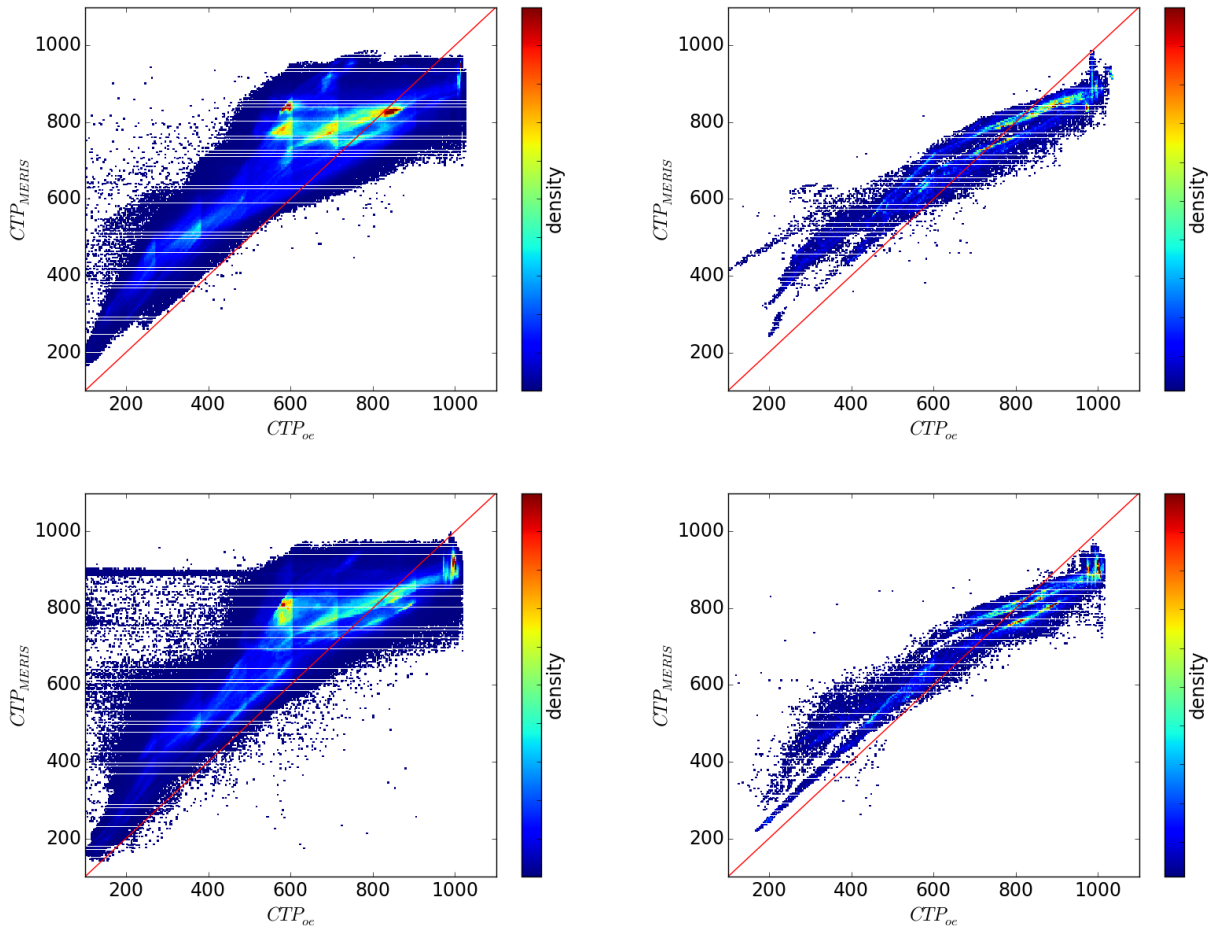


Figure 6.2.5 Scatter plots of OE CTP versus MERIS I2 CTP product for the February 2003 orbits. Upper panels is for orbit on 15th and lower panels is for the orbit on the 5th. The left panels are for the all pixels while the right panels are for pixels that match the MERIS-11 channel central wavelengths used in our LUT building (761.875nm) to ± 0.01 nm.

Figure 6.2.6 shows the cost function, the number of iterations, the residual on reflectance (I) and the residual on signal ratio (R) for pixels of the orbit of February 5th that match the MERIS-11 channel central wavelengths used in our LUT building (761.875nm) to ± 0.01 nm. Most pixels have a cost function < 1 and converge within only 1 iteration. The residuals are also very low. The measurement vector (I, R) is then easily reproduced by our forward model. This is because I fully constrains COT and R the CTP (knowing COT). There is no interplay because (i) CTP does not impact I and (ii) given a COT, there is always a value of CTP that allows to reproduce R. The range of (I, R) can be reproduced even with the simplistic one layer model and the cost function does not raise when the model departs from reality (multi-layer cloud for example). The low number of iteration shows that the first guess obtained by a simple 1D interpolation is already close to the final solution (for the same reason).

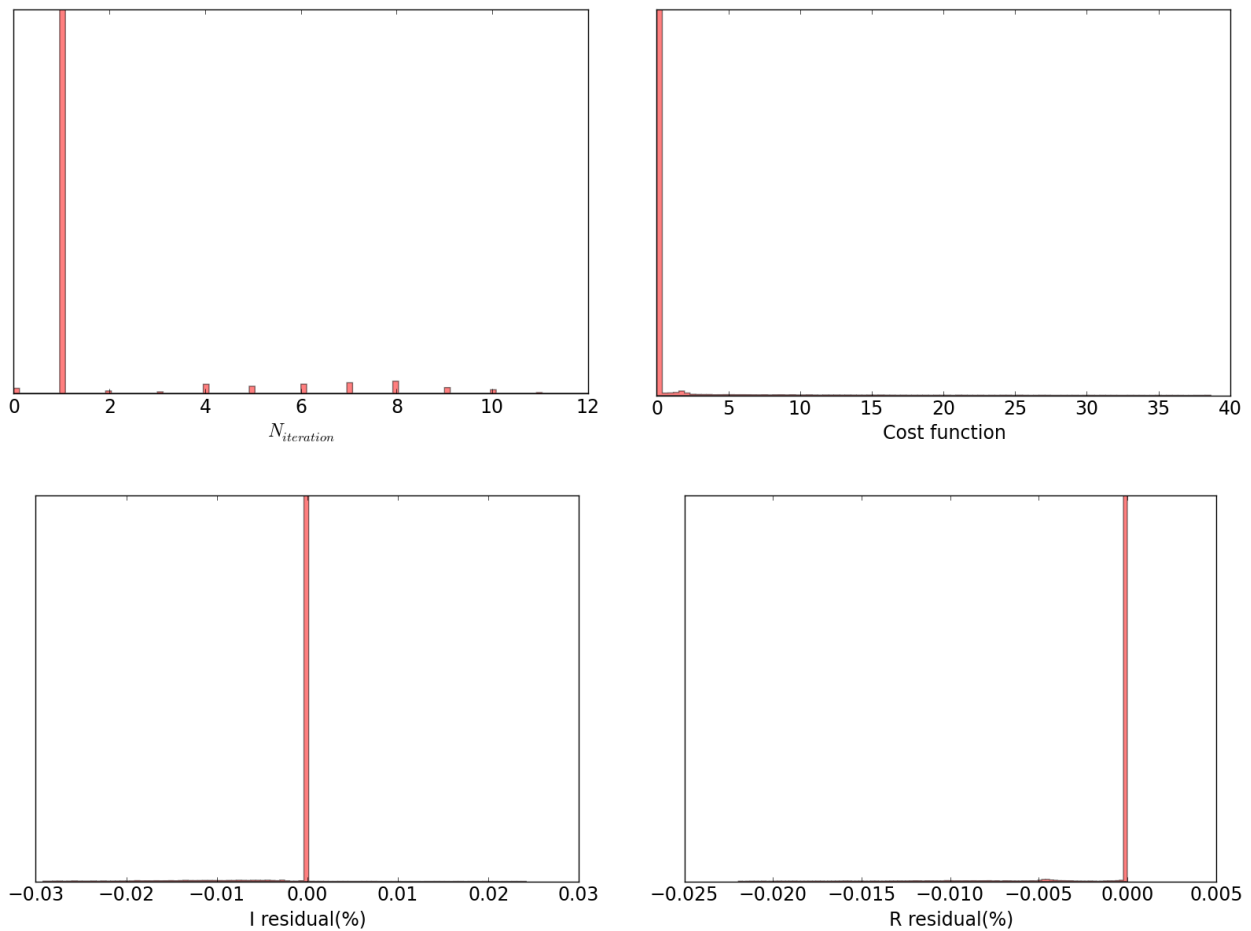


Figure 6.2.6 Number of iterations, a posteriori cost function, residual for the reflectance and residual for the signal ratio for pixels of the orbit of February 5th that match the MERIS-11 channel central wavelengths used in our LUT building (761.875nm) to ± 0.01 nm.

Figures 6.2.7, 6.2.8 and 6.2.9 show COT and CTP maps for selected scenes in the studied orbits. Day-1 algorithm and the MERIS L2 products are shown with common range. We show all pixels although our OE CTP product is clearly affected by the non corrected smile effect. The comparison is still interesting because beyond the smile effect that shows up as vertical stripes, we can compare the small scale structure in CTP maps.

Figure 6.2.7 shows a Stratocumulus scene over the ocean. The CTP is supposed to be rather constant around ~ 800 hPa over the scene as seen on CTP MERIS L2 retrieval. The smile effect is then particularly obvious in OE CTP but the variability in the vertical direction is low as expected. The COT matches quite well. We note that our OE retrieval extend toward lower COT (blue on maps) than the MERIS L2 that does not allow COT lower than 1.0.

Figures 6.2.8 and 6.2.9 show a depression in southern Atlantic and a storm over Africa respectively. For those two scenes, the dynamical range in CTP is large. Beyond the smile stripes, the small scale structure in CTP maps are in rather good agreement. The COT maps are also in good agreement.

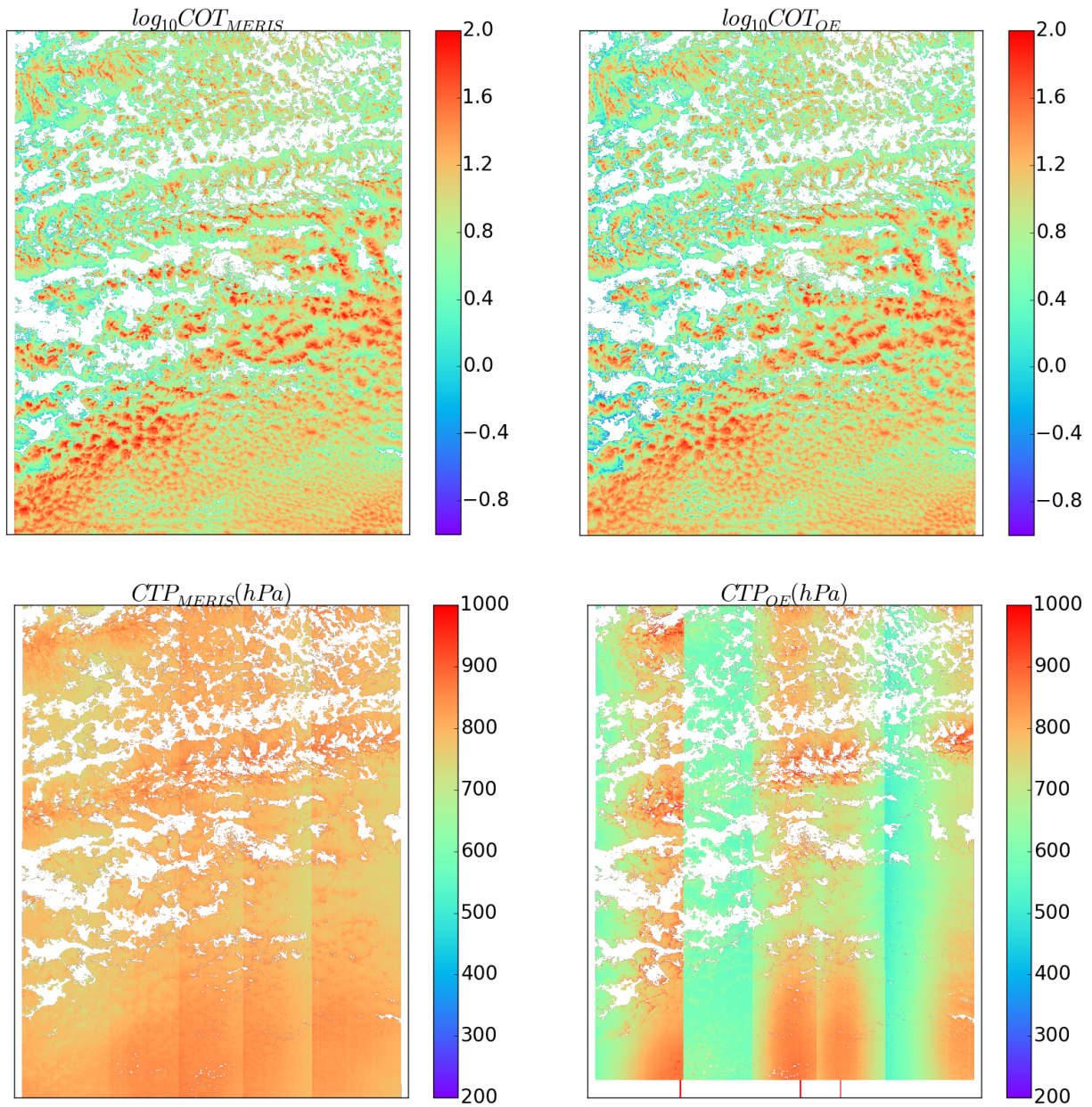


Figure 6.2.7 COT (upper panels) and CTP (lower panels) maps for Stratocumulus in the Southern Atlantic on the orbit of August 24th. Left panels are for MERIS L2 products and right panels are for OE retrieval. On CTP_{OE} , red dashes at the bottom of the image shows the pixel columns corresponding to wavelengths of our LUT building (761.875nm) to ± 0.01 nm.

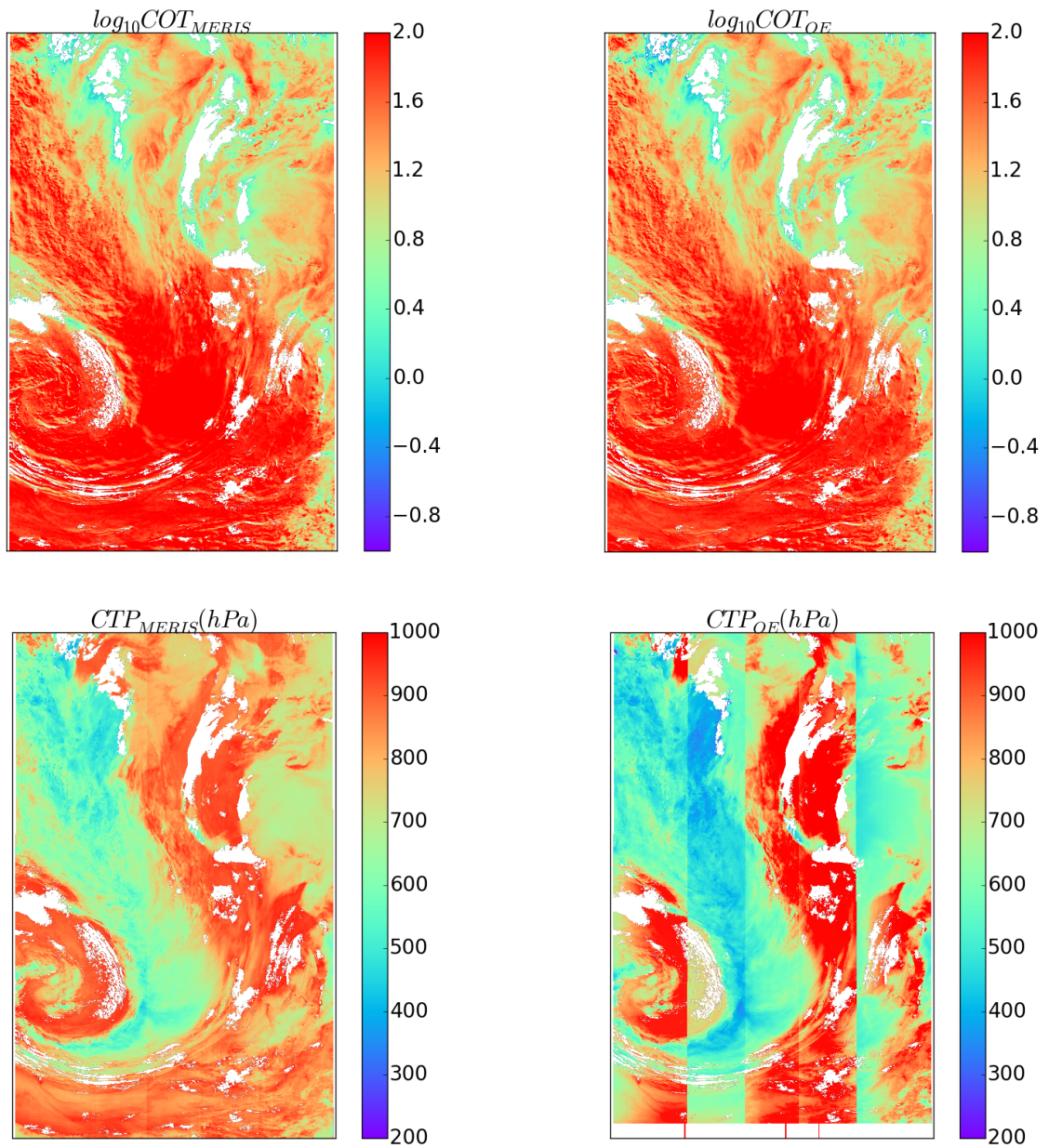


Figure 6.2.8 COT (upper panels) and CTP (lower panels) maps for a depression in southern Atlantic in the orbit of February 5th. Left panels are for MERIS L2 products and right panels are for OE retrieval. On CTP_{OE} , red dashes at the bottom of the image shows the pixel columns corresponding to wavelengths of our LUT building (761.875nm) to ± 0.01 nm.

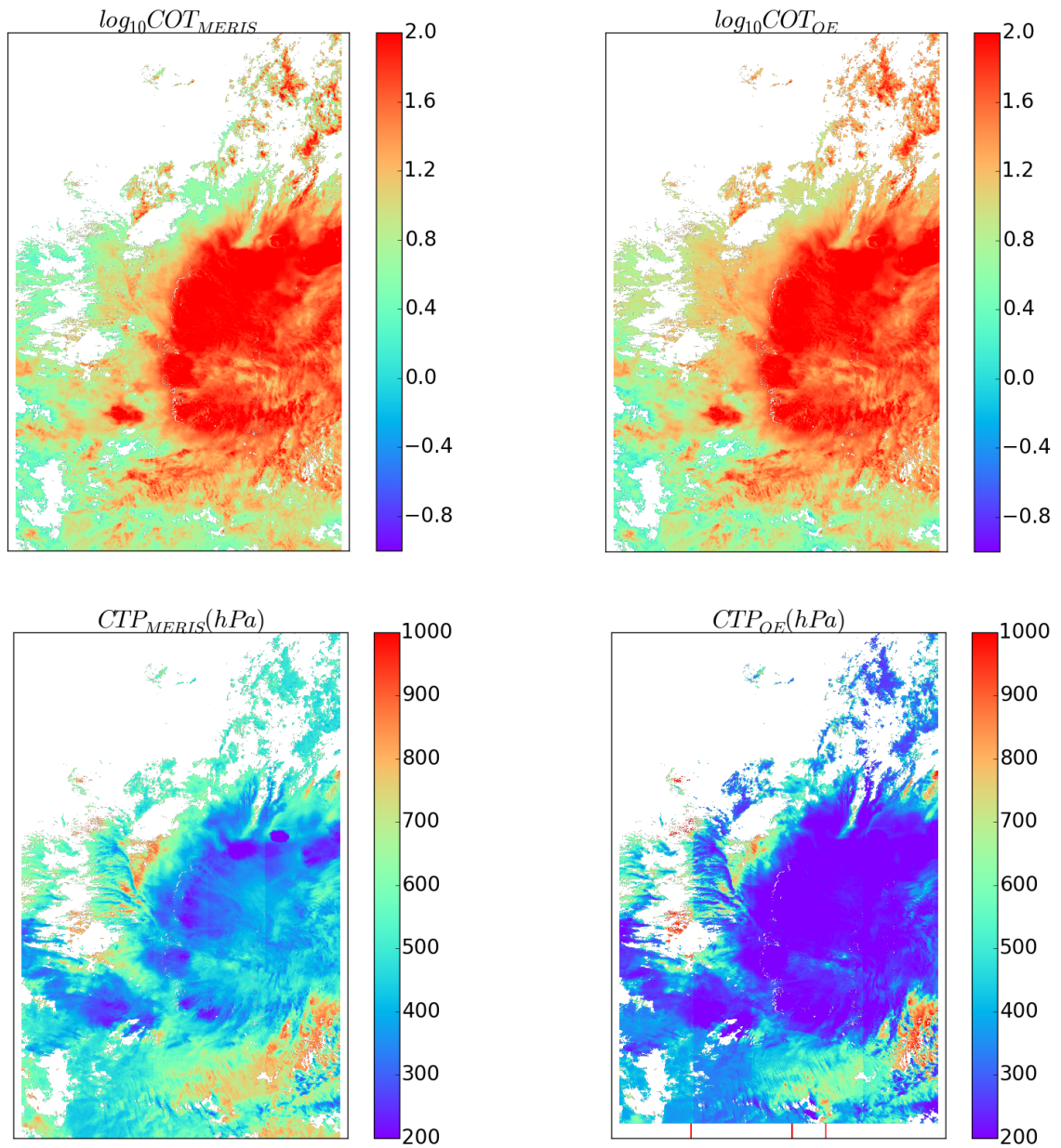


Figure 6.2.9 COT (upper panels) and CTP (lower panels) maps for stormy conditions over Africa in the orbit of August 24th. Left panels are for MERIS L2 products and right panels are for OE retrieval. On CTP_{OE} , red dashes at the bottom of the image shows the pixel columns corresponding to wavelengths of our LUT building (761.875nm) to ± 0.01 nm.

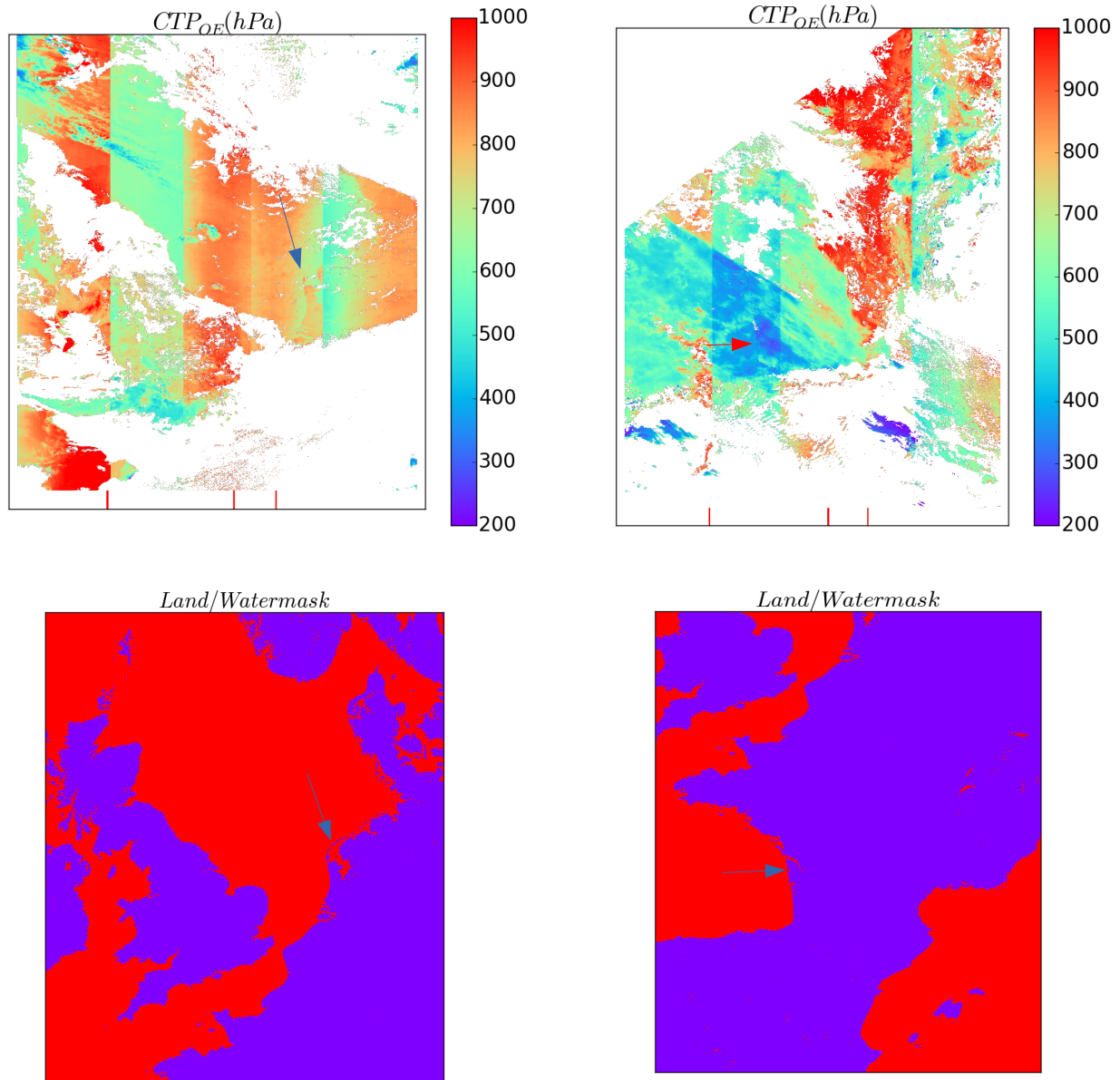


Figure 6.2.10 Land/water mask and CTP_{OE}, for two different scene (part of Aug 24th for left panel and part of Feb 5th for right panel).

Figure 6.2.10 shows land/water mask and CTP_{OE}, for two different scenes. We can see a discontinuity at the water/land transition. Two examples are marked with arrows on the figure. The difference in the modelling of the land and ocean is responsible for that discontinuity. The land being brighter than the sea (at least out of glitter geometries) the retrieval might be less reliable in the former case. Note that such discontinuities can also appear in the MERIS L2 product. In our Day-1 retrieval; this effect should be reduced when using the high resolution LUT rather than the current medium resolution. This can also be due to the WSA ancillary product that we used being a large band product (entire visible range) rather than specifically 753-761 nm range. On the other hand, no discontinuities are seen in COT maps.

The day-1 retrieval could also be compared to the FAME-C [Carbajal Henken et al. 2014] products. The

results should be closer since we used the same vertical profile climatology. However differences are still expected, mostly because we adjust the CGT using an other climatology. This comparison is beyond the scope of the present study.

7 CONCLUSION AND PERSPECTIVES

7.1 Summary/conclusion on the present study

A bibliography study on CTP retrieval from O₂ A-band has been done. It gathers results from pioneer theoretical work as well as from its applications to instruments with characteristics similar to METImage (section 2). This first step allowed us to summarize the key parameters driving the signal ratio (VII-5/VII-4). It also pointed the limits in term of information content that can be collected with the METImage instrument. A short review on radiative transfer models suited for the modelling of O₂ A-band in cloudy atmosphere was given (section 3). We presented in more details the ARTDECO radiative transfer toolbox that was used for the present study.

In section 4, we presented the sensitivity of the signal ratio to parameters whose importance was already pointed in previous study, like the COT or cloud vertical structure, but specifically for the METImage ISRF. The sensitivity is presented in term of CTP bias. We extended the study to new parameters like the surface reflectance directionality (BRDF) or the shape of VII-5 ISRF. Unlike in most previous study, the sensitivity to all parameters is presented for a continuous range of (COT, CTP) and either for liquid and ice clouds. On the other hand, we presented the sensitivity of the reflectance (used to retrieved COT) to various parameters together with the propagation of a resulting COT bias to a CTP bias. This work allowed us to identify critical parameters whose representation in the forward model needed to be as realistic as possible for a reliable CTP estimate.

The Day-1 algorithm and LUT are described in section 5. The Day-1 algorithm aims to retrieve (COT, CTP) state vector from (VII-3, VII-5/VII-4) measurement vector above land surface and (VII-6, VII-5/VII-4) measurement vector above water (ocean) surface. The retrieval is based on optimal estimate method with Levenberg-Marquardt iterations. A prototype version of the algorithm was developed in Python. One version is intended for testing on MERIS data and an other version for testing on METImage synthetic data.

For the forward model to be fast enough for operational context, it has to be sampled in LUT to be interpolated at retrieval time. However it must be as realistic and accurate as possible. A trade off must then be find regarding the number of parameters to be sampled in the LUT, the accuracy related to interpolation and the size of the LUT. Based on the bibliography and sensitivity study, we selected the parameters to be sampled (e.g. surface albedo or wind-speed, surface pressure). Although being of crucial importance for the signal ratio, the cloud vertical extinction profile and cloud geometrical thickness can not be constrained together with CTP with METImage instrument. We proposed to rely on climatologies to vary those two parameters as a function of (COT, CTP) in LUT. The surface reflectance directionality (as a function of the surface kind) and cloud phase are varied by mean of switching between different LUT following a pixel masking provided as an input in the algorithm. A version (so called high resolution) of the LUT was computed for which interpolation error does not exceed the foreseen METImage calibration accuracy while its size is compatible with RAM size for modern computer (~1Go).

The testing of Day-1 algorithm was presented in section 6. The test on METImage synthetic data showed a stable behaviour of the algorithm. The retrieved COT and CTP are compared with values used for the computation of the synthetic data. Since the forward model used in the LUT and synthetic data computation are the same, the error on retrieved COT, CTP is fully related to LUT interpolation error. This error on CTP is not much than ~15hPa. The OE a-posteriori uncertainty estimate is consistent with that error.

The testing of Day-1 algorithm on MERIS data is done for 4 orbits over Europe, Africa, Atlantic in February and August. The algorithm showed a very robust behaviour. It processed all pixels of the 4 orbits without external intervention. We presented a comparison between our retrieval and the MERIS L2 product. One has to keep in mind that the forward models are different in those two retrievals which fix the limit for a quantitative comparison. Our retrieved COT is within 50% of the MERIS L2 product. Our CTP is rather consistent with MERIS L2 product for clouds around ~800hPa. For higher clouds, our retrieval tends to place cloud top at greater altitude than MERIS L2 product. This may be due to the CGT increasing with altitude in our forward model which has the effect of moderating the increase of signal ratio when increasing cloud altitude. The small spatial scale structure in either COT and CTP maps are very similar for our retrieval and the MERIS L2 product.

7.2 Caveats and short term possible evolutions

As mentioned in section 5.6, for the land BRDF modelling in the current LUTs building, we use the normalized volumetric and geometric parameters for each biome as given by Bacour and Bréon [2005] at 670nm either for the modelling of 670 nm and 752/763nm TOA intensities. An interpolation using the values given by Bacour and Bréon [2005] at 865nm could be done in a future version for the 752/763nm. On an other hand, the surface albedo is the same at 752 and 763 nm in LUT since we store the ratio. To vary the surface albedo independently at 752 and 763nm would require to store the I_{752} and I_{763} separately which would nearly double the LUT size.

Also concerning the surface, a dynamical snow/ice cover mask may be required on top of the IGBP type mask. If not available, one can switch to snow/ice surface (BRDF) type if the WSA for the pixel is greater than a threshold value.

In accounting for the vertical structure climatology when building the LUTs, we interpolated the CPR profiles and CGT linearly in COT and CTP. For COT, a linear interpolation in $\log_{10}(\text{COT})$ may be more appropriate.

In order to obtain LUTs in a reasonable amount of time regarding the study time line, we used 8 computational angles (streams) and apply the single scattering correction (TMS) to the TOA reflectance. For a pure scattering liquid cloud of opacity 5.0 (see benchmark from Kokhanovsky et al. [2010]), the obtained TOA radiance is accurate to better than 0.4% out of the rainbow and glory geometries. For the future building of LUT to be used for the operational retrieval, this number of streams can be increased.

The range for LUT sampling may be extended/modified. In particular:

- The WSA could extend to brighter values than ~0.45 for desert
- The WSA could extend to lower values than 0.6 for snow/ice
- The surface pressure should be extended to values smaller than 850hPa to cover pixels at high altitude (850 hPa corresponds to ~1500m for sea level pressure of 1013hPa).
- For the COT, we may restrict to values between ~1 and ~100 keeping the same sampling steps. This would reduce the LUT size by ~35%.

The size for a single (I_{LUT} , R_{LUT}) is currently 1211Mo for high resolution sampling. Several ways to reduce

the memory load are possible:

- An integer coding of the form $\text{FLOAT} = A * \text{INT} + B$, where A and B are floats can be used. Since we currently store LUT as FLOAT32, we would reduce the LUT size by a factor of 2 by coding with INT16 and a factor of 4 by coding with INT8. To use INT16 would result in a maximum relative error due to coding of $\sim 0.001\%$ on the signal ratio (R_{LUT}) and $\sim 0.03\%$ on reflectance I_{LUT} . To use INT8 would result in a maximum relative error due to coding of $\sim 0.25\%$ on the signal ratio (R_{LUT}) and $\sim 8\%$ for reflectance I_{LUT} . INT8 is then acceptable for R_{LUT} since the error due to coding would then be of the order of the interpolation error for high resolution LUT (lower than inter-band bias, see section 6.1.2.a). For I_{LUT} we can code in INT16. For high resolution LUT, we would then reduce the ($R_{\text{LUT}}, I_{\text{LUT}}$) size to (257Mo, 93Mo) instead of (1026Mo, 185Mo).
- We may reduce the number of ($R_{\text{LUT}}, I_{\text{LUT}}$) to be successively loaded by merging sufficiently close surfaces biomes. For example, we may only have one forest surface instead of the needle-leaf and broad-leaf forests. This would be especially obvious if we reduce the COT LUT range to a minimum of 1 instead of 0.1 because the surface directionality would then be of lower impact.
- The number of sampled geometries may be reduced thanks to the computation of the first order of scattering on-the-fly during the retrieval (see section 7.3). The LUT would only contain order of scattering >1 for which the signal varies more smoothly as a function of the geometry.
- The retrieval may be performed on 5 minutes observation granules. Within such a granule, non-retrieved parameters (SZA, wind-speed, ...) vary over a limited range that may be narrower than the one sampled in LUT. The LUT can then be only partially loaded in order to reduce the memory load.

The OE method is of great interest in term of error estimation. For that, the input covariance matrix must be as complete and reliable as possible. Some error sources may be added or modified regarding the current definition :

- Uncertainty due to model assumptions could be added (3D effects, Legendre polynomial expansion, specificity, etc...).
- The standard deviation of the vertical structure climatology may be accounted for.
- The variability of the LUT interpolation error with COT may be accounted for.
- The computation of S_f is time consuming and may be done once for a fixed value of $(b, x)_{Sf}$. A hybrid solution could be to compute this fixed S_f for a high COT for a use if COT_0 (first guess) is high enough (regarding a critical value to be defined) and to compute it on a pixel-by-pixel basis $S_f = f(b, x_0)$ for thinner clouds. Indeed S_f is more sensitive to (b, x) for thinner clouds than for thick clouds. For example, over the glitter the sensitivity of S_f to the geometry or to the wind-speed is greater for a thinner cloud.

7.3 Further evolution of the algorithm and LUTs

The testing of Day-1 algorithm with POLDER/PARASOL data would be of great interest although the ISRF characteristics are slightly different than METImage. It would allow for the comparison of the retrieved CTP against active instrument data (e.g. CPR/CALIOP) through the use of Calxtract. This application extracts some variables issued of different sensors (CALIOP, IIR, MODIS, PARASOL, CLOUDSAT, and more in the future) with pixels in coincidence with the CALIOP measurements either at 333m or 5km horizontal resolution. Any effect related to the observation geometry could also be pointed out tanks to the multi-angle capability of PARASOL/POLDER.

The cloud vertical structure climatology (either CGT and profile) could be refined for given regions (mid-latitude, tropic, etc..) and seasons. Corresponding separated LUT would be build. An aerosol contribution could be added to those LUT whose kind and load may be adapted as function of the season and region. However, aerosol properties would still be fixed across the LUT range. On the other hand, the LUT over water surface is currently created by considering the CGT climatology corresponding to ocean locations. That is fine for all pixels over the ocean. However, for in-land water pixels, an additional LUT with water surface but using the CGT climatology for in-land position should be created.

As seen in section 6 and also outlined by Minnis et al. [1998], an angular interpolation between LUT values can introduce large errors in reflectance. Whereas errors are weak for directions where the cloud phase function is smooth, they can be much too large for particular directions such as the cloudbow and the backscattering direction. As large errors due to interpolation between angle nodes are related to large angular variations in the reflectance part due to the first order of scattering R₁, only the difference R - R₁ should be interpolated. The LUT would then contain R-R₁ while R₁ would be computed on-the-fly at retrieval time. This is possible because R₁ is computed with a simple analytical formulation that is very lightly CPU demanding. This technique was already successfully applied (e.g. Buriez et al. [2005]).

The study has confirmed that the cloud top altitude estimate from O₂-A band is very sensitive to the actual vertical extent of cloud layer and its optical thickness. In particular for high altitude optically thin layers, ambiguous determination of CTOP can occur due to photons having reached surface or a lower thicker cloud layer and been reflected to space, significantly increasing the photons mean path length. In the absence of sufficient information content, the Day-1 algorithm does not only fail to properly retrieve the true CTP in such a situation, it does not even allow to disentangle it from a thicker mono-layer cloud as represented in our forward model. Increasing the information content then appears crucial for the reliability of the CTP product. This can be achieved by bringing in additional spectral channels. For METimage, 3 possibilities can be readily identified that would however have to be further investigated. These are located at both ends of the spectrum compared to the O₂-A band channel and are namely :

- the 443 nm channels : the strong spectral dependence of the Rayleigh scattering can create a significant contrast between the radiances observed at shorter wavelength compared to that observed at 865 nm. Further, the coupling between Rayleigh scattering and cloud scattering within cloud layer is expected to be sensitive to the actual cloud extinction profile and might therefore provide additional information content in terms of cloud vertical extent / optical thickness constraint. It remains to be established quantitatively how much information can be gained through this and whether the spectral variation of surface albedo over land can be constrained sufficiently to maintain this additional information content.
- the absorbing water vapour channel (at 910 nm or 1.37 microns) : the use of channel impacted by water vapour absorption is expected to be challenging due to the limited knowledge about water vapour profile in the atmosphere. However, on a qualitative basis, the simple detection of elevated layers by means of these channels (especially the strongly absorbing 1.37 microns channel) can provide enough information to constrain the value of cloud top to remain closer to elevated layer and can partly solve the ambiguity observed in case of thin semitransparent layers (which tend to be located too low in the atmosphere when only O₂-A band channels are used).
- thermal infrared channels : similarly to the previous water vapour channel, the infrared channels of VII could be used to estimate the cloud emissivity and better constrain the cloud altitude thanks to their high sensitivity to thin elevated layers. (following Heidinger and Pavolonis [2009]).

Whether these three sources of information should enter the measurement vector or be used to set a prior estimate should be investigate. On the other hand, these investigations should probably be done in regards of the more extended retrieval foreseen with the MOCA algorithm.

8 ANNEX

8.1 Sensitivity normalized by instrument noise

8.1.1 Sensitivity of the signal ratio

In section 4.2, to assess the sensitivity of $R = I_{763}/I_{752}$ to a given parameter, we varied the parameter and measured the impact ΔR as a function of COT and CTP. For any (COT, CTP) couple, ΔR was converted into an equivalent variation of CTP. ΔCTP is the CTP variation that would produce the same variation of R as the parameter change. In the present section we show plots of those ΔCTP , normalized by ΔCTP_{noise} , the variation of CTP equivalent to ΔR related to the instrument noise (see section 4.2.1). ΔCTP_{noise} corresponds to the limit of detection given by the instrument noise.

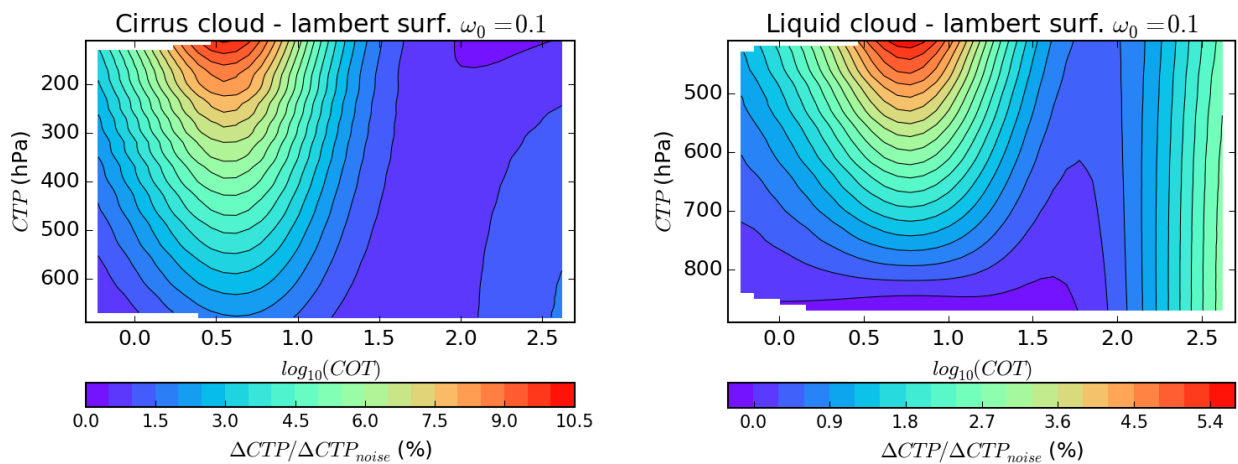


Figure 8.1.1 Variation of CTP equivalent to a change of COT by $\pm 10\%$ for the ratio 752/763nm normalized by the limit of detection.

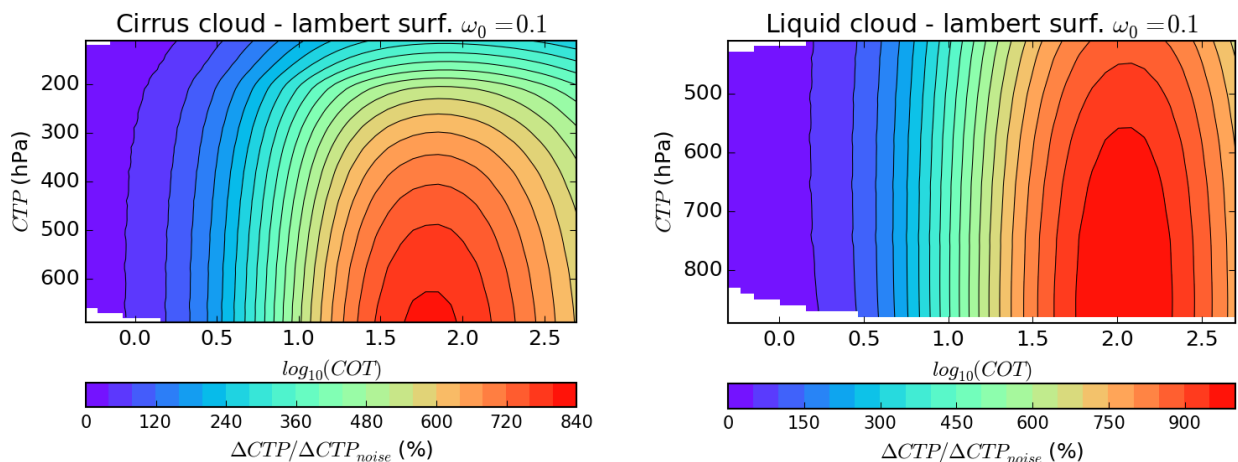


Figure 8.1.2 Variation of CTP equivalent to a change of CGT by $\pm 10\%$ for the ratio 752/763nm normalized by the limit of detection.

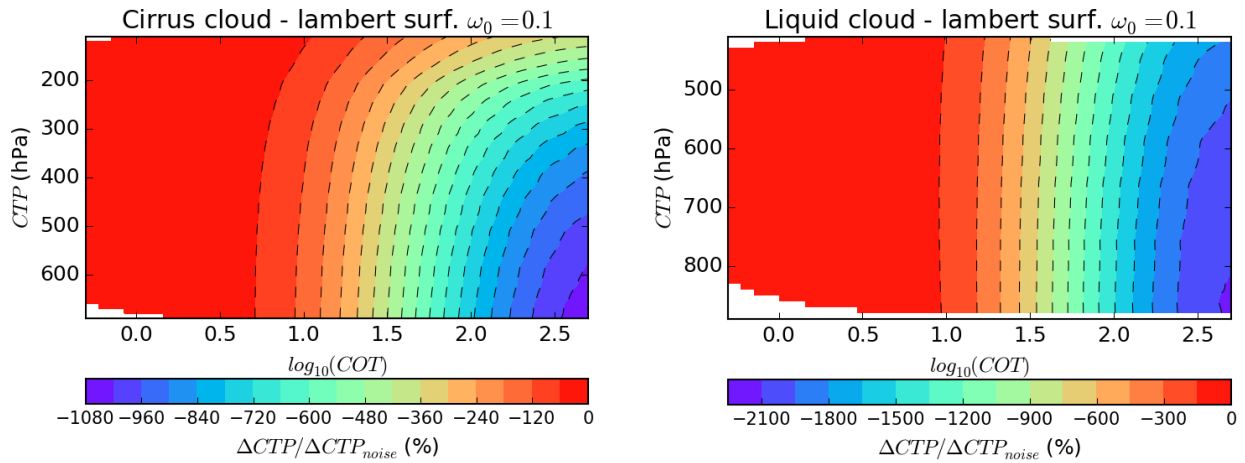


Figure 8.1.3 Variation of CTP equivalent to a change between a CPR profile (Cirrostratus and Stratocumulus) to a homogeneous profile for the ratio 752/763nm normalized by the limit of detection.

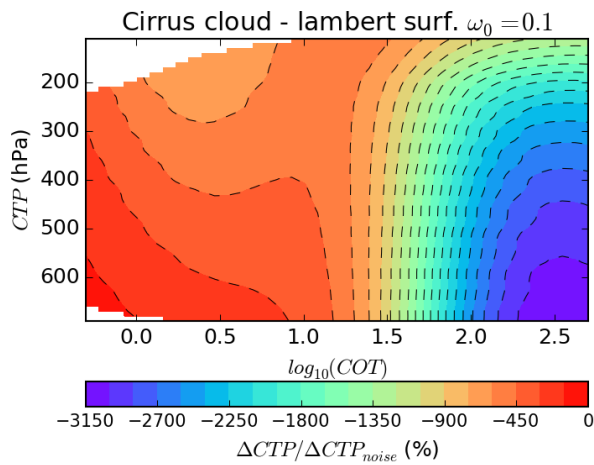


Figure 8.1.4 Variation of CTP equivalent to a change of ice particle model (see figure 4.2.5) for the ratio 752/763nm normalized by the limit of detection.

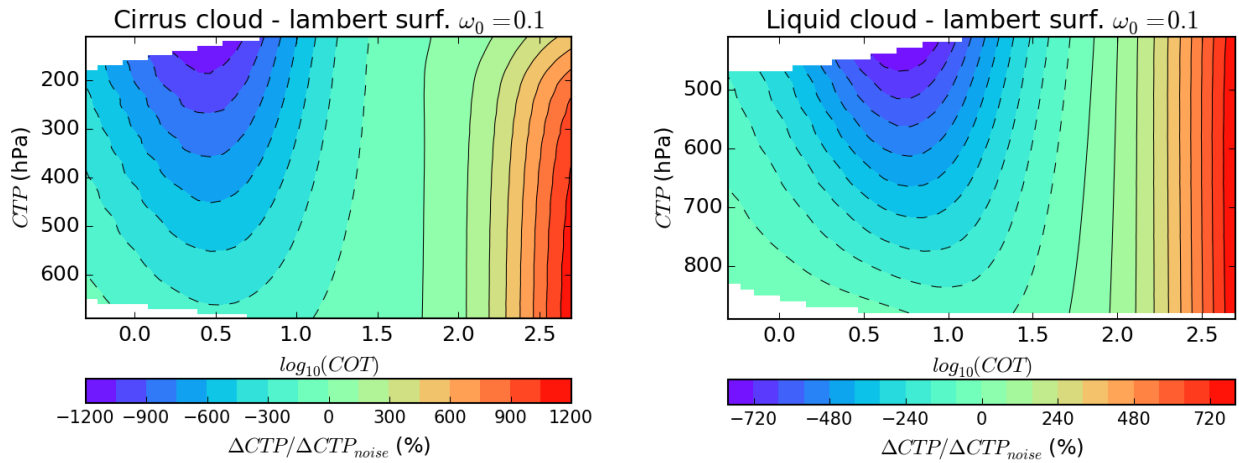


Figure 8.1.5 Variation of CTP equivalent to a change of particle effective radius between 5 and 30 (60) microns for Liquid (ice) cloud for the ratio 752/763nm normalized by the limit of detection.

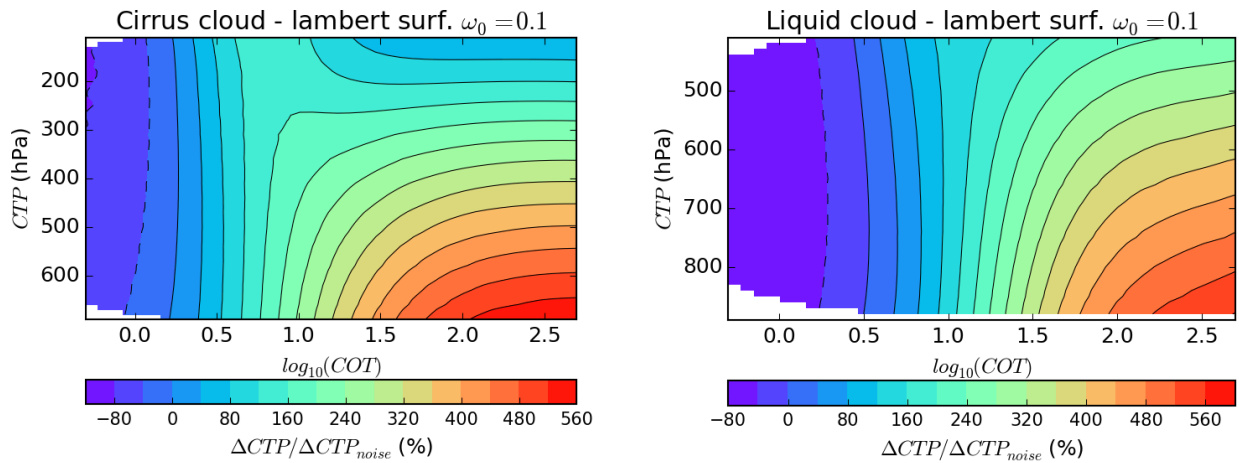


Figure 8.1.6 Variation of CTP equivalent to the presence of a continental average aerosol ($H=8\text{km}$, $\tau=0.1$) for the ratio 752/763nm normalized by the limit of detection.

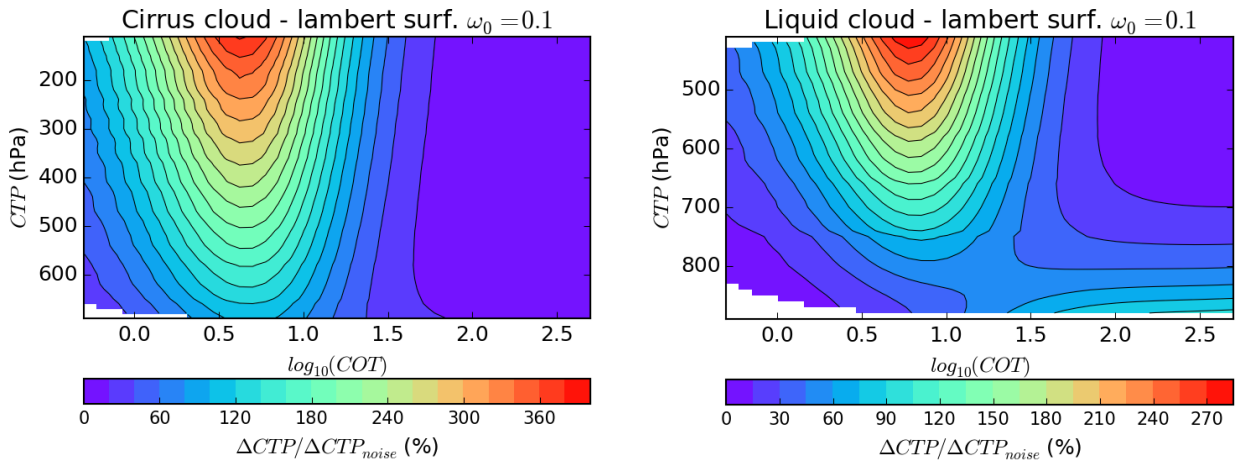


Figure 8.1.7 Variation of CTP equivalent to the presence of a maritime clean aerosol ($H=1\text{km}$, $\tau=0.1$) for the ratio 752/763nm normalized by the limit of detection.

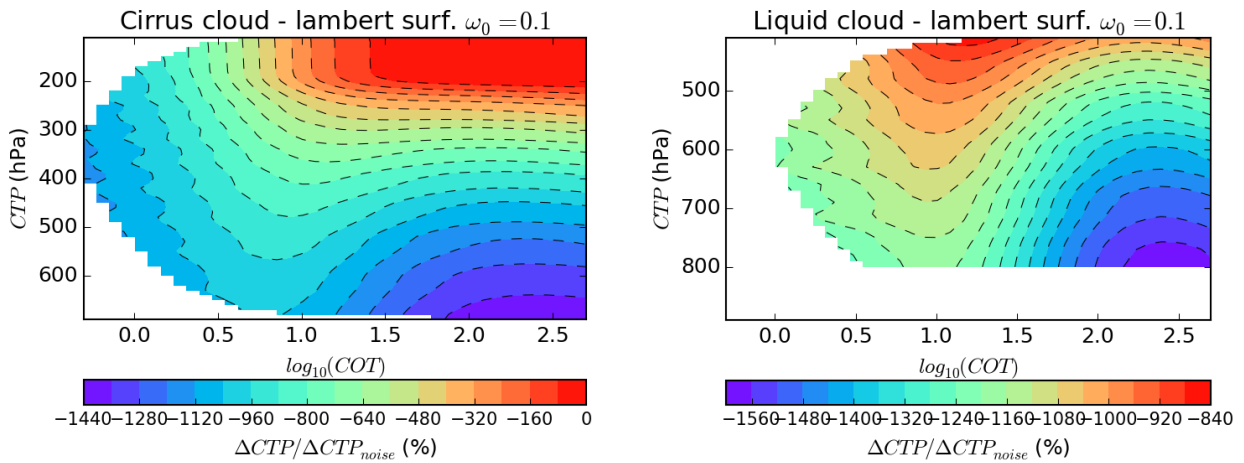


Figure 8.1.8 Variation of CTP equivalent to a change of $\pm 10\%$ of the surface pressure for the ratio 752/763nm normalized by the limit of detection.

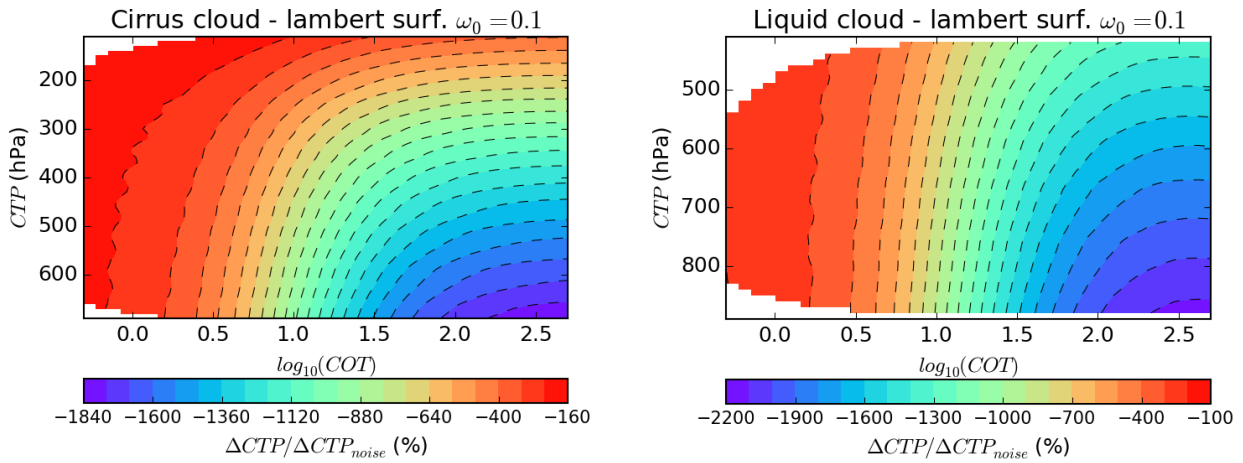


Figure 8.1.9 Variation of CTP equivalent to a variation of energy in the 763 nm ISRF wings from 1% to 5% for the ratio 752/763nm normalized by the limit of detection.

8.1.2 Sensitivity of window channel reflectance

In section 4.3, we studied the sensitivity of the reflectance (either 670nm or 865nm) used to constrain COT, to various parameters. After varying those parameters, we measured the resulting ΔI as a function of COT. The ΔI was converted to an equivalent variation of COT. ΔCOT is the COT variation that would produce the same variation of reflectance as the parameter change. This corresponds to a bias that will occur if fixing or having an uncertainty on the given parameter for the retrieval. Likewise in section 4.2, $\Delta COT = f(COT)$ is propagate to an equivalent ΔCTP regarding its impact on the signal ratio. Finally, in the present section we show plots of those ΔCTP , normalized by ΔCTP_{noise} , the variation of CTP equivalent to ΔR related to the instrument noise (see section 4.2.1). ΔCTP_{noise} corresponds to the limit of detection given by the instrument noise.

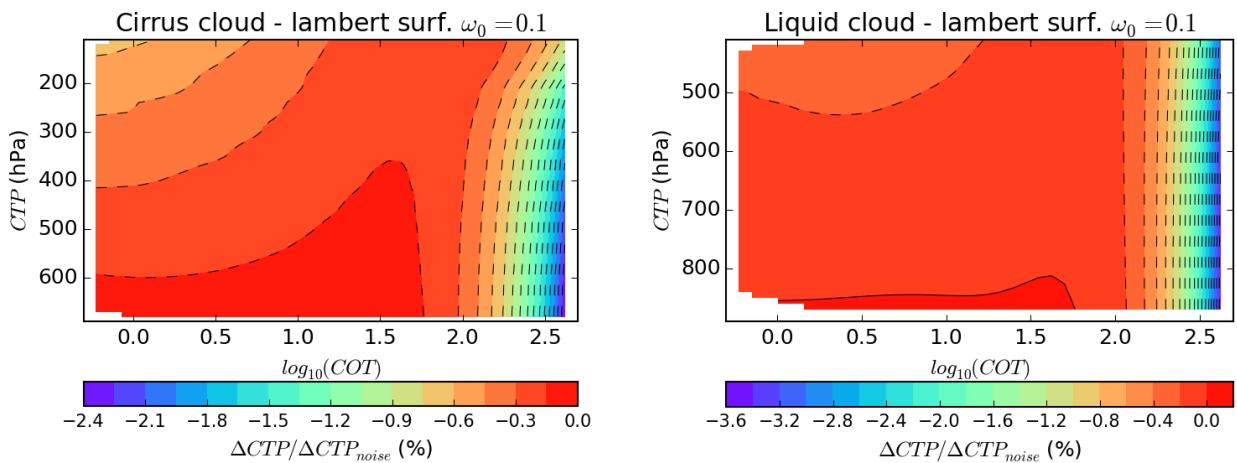


Figure 8.1.10 ΔCTP equivalent to ΔCOT due to a variation of the Ozone column by $\pm 10\%$ normalized

by the limit of detection.

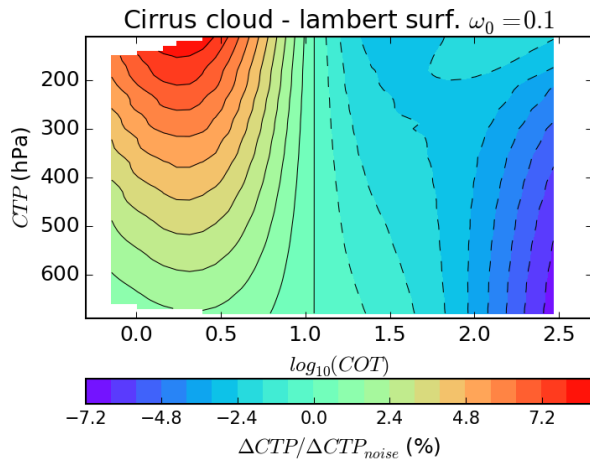


Figure 8.1.11 ΔCTP equivalent to ΔCOI due to a change of ice particle model (see figure 4.2.5) normalized by the limit of detection.

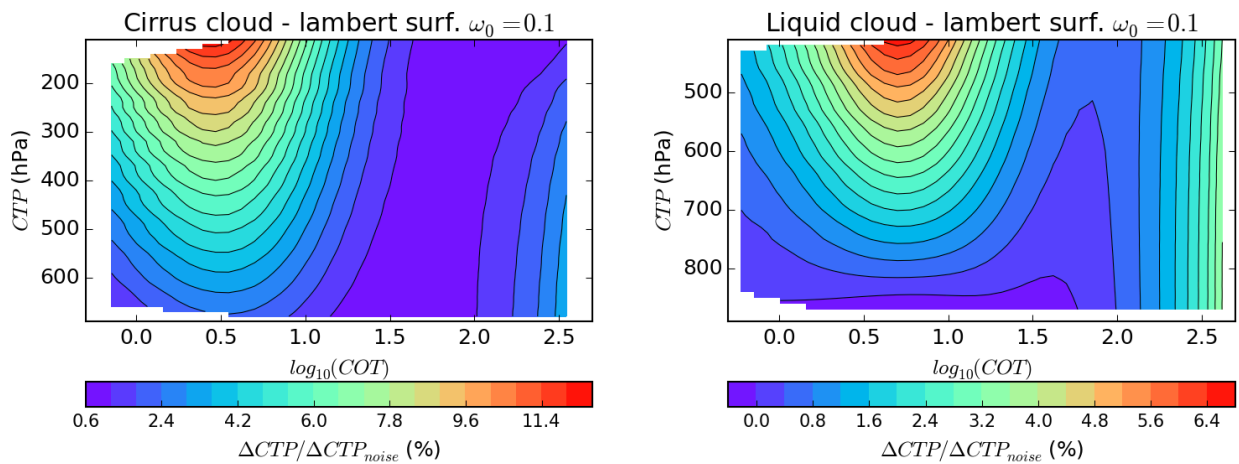


Figure 8.1.12 ΔCTP equivalent to ΔCOI due to a change of particle effective radius between 5 and 30 (60) microns for Liquid (ice) cloud normalized by the limit of detection.

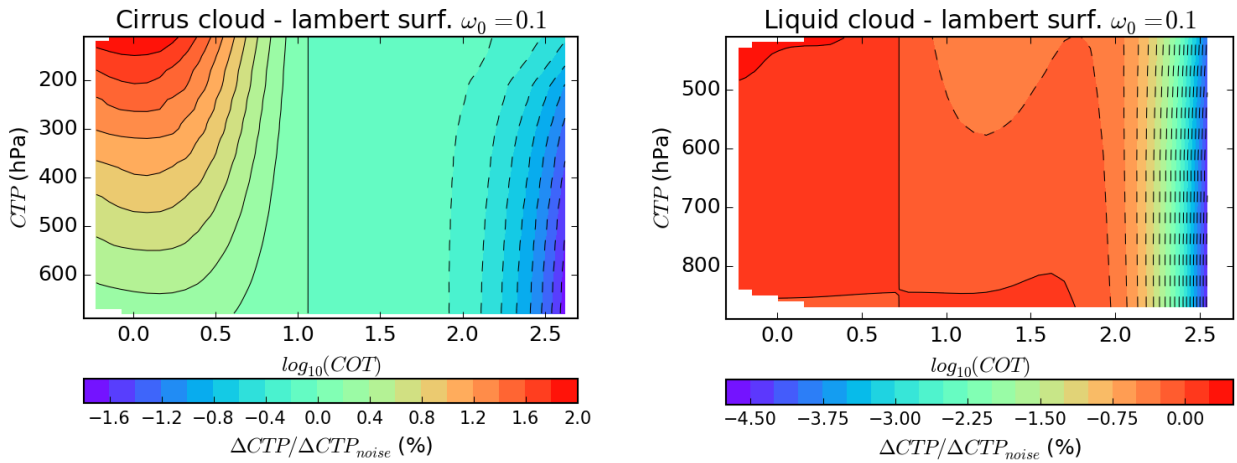


Figure 8.1.13 ΔCTP equivalent to ΔCOI due to the presence of a continental average aerosol ($H=8\text{km}$, $\tau=0.1$) normalized by the limit of detection.

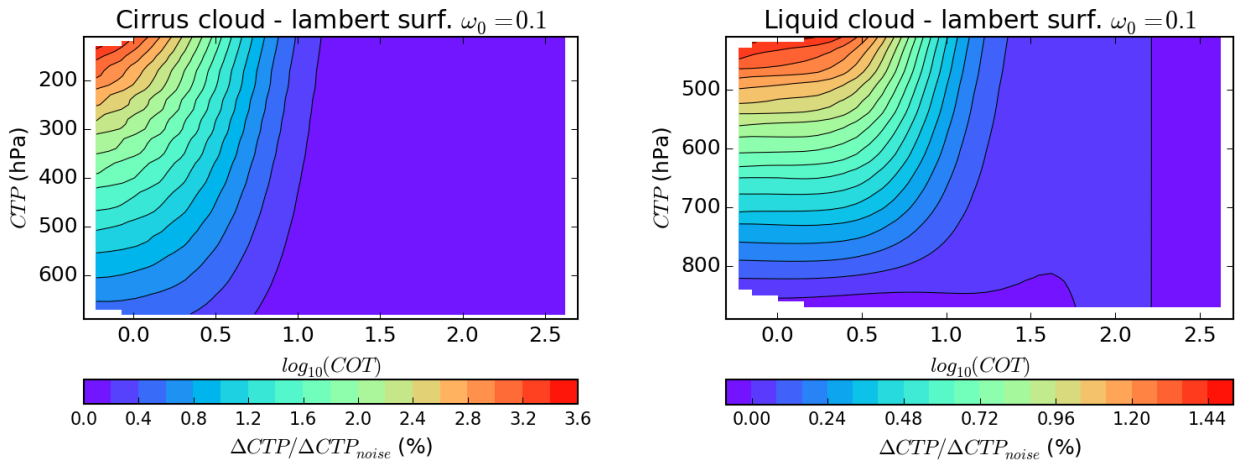


Figure 8.1.14 ΔCTP equivalent to ΔCOI due to the presence of a maritime clean aerosol ($H=1\text{km}$, $\tau=0.1$) normalized by the limit of detection.

8.2 References

- Anderson, G.; Clough, S.; Kneizys, F.; Chetwynd, J. and Shettle, E. (1986). *AFGL atmospheric constituent profiles (0–120km)*, .
- Bacour, C. and Bréon, F.-M. (2005). *Variability of biome reflectance directional signatures as seen by POLDER*, *Remote Sensing of Environment* 98 : 80 - 95.
- Baum, B. A.; Yang, P.; Heymsfield, A. J.; Bansemmer, A.; Cole, B. H.; Merrelli, A.; Schmitt, C. and Wang, C. (2014). *Ice cloud single-scattering property models with the full phase matrix at wavelengths from 0.2 to 100 μ m*, *JQSRT* 146 : 123-139.
- Bennartz, R. and Fischer, J. (2000). *A modified k-distribution approach applied to narrow band water vapour and oxygen absorption estimates in the near infrared*, *JQSRT* 66 : 539-553.
- Bréon, F. and Parasol team (2006). *Parasol level-1 product data format and user manual*, .
- Buriez, J. C.; Vanbauce, C. and Parol, F. (1997). *Cloud detection and derivation of cloud properties from POLDER*, *International Journal of Remote Sensing* 18 : 2785-2813.
- Buriez, J.-C.; Parol, F.; Cornet, C. and Doutriaux-Boucher, M. (2005). *An improved derivation of the top-of-atmosphere albedo from POLDER/ADEOS-2: Narrowband albedos*, *Journal of Geophysical Research (Atmospheres)* 110 : 5202.
- Carbajal Henken, C. K.; Doppler, L.; Lindstrot, R.; Preusker, R. and Fischer, J. (2015). *Exploiting the sensitivity of two satellite cloud height retrievals to cloud vertical distribution*, *Atmospheric Measurement Techniques Discussions* 8 : 2623-2655.
- Carbajal Henken, C. K.; Lindstrot, R.; Preusker, R. and Fischer, J. (2014). *FAME-C: cloud property retrieval using synergistic AATSR and MERIS observations*, *Atmospheric Measurement Techniques* 7 : 3873-3890.
- Carbajal-Henken, C.; Lindstrot, R.; Filipitsch, F.; Walther, A.; Preusker, R. and Fischer, J. (2013). *FAME-C: Retrieval of cloud top pressure with vertically inhomogeneous cloud profiles*, *AIP Conference Proceedings* 1531 : 412-415.
- Clough, S.; Kneizys, F. and Davies, R. (1989). *Line shape and the water vapor continuum*, *Atmospheric Research* 23 : 229 - 241.
- Compiegne, M.; C.-Labonnote, L. and Dubuisson, P. (2013). *The phase matrix truncation impact on polarized radiance*, .
- Cox, C. and Munk, W. (1954). *Measurement of the roughness of the sea surface from photographs of the sun's glitter*, *Journal of the Optical Society of America* (1917-1983) 44 : 838.
- de Haan, J. F.; Bosma, P. B. and Hovenier, J. W. (1987). *The adding method for multiple scattering calculations of polarized light*, *A&A* 183 : 371-391.
- Delwart, S.; Preusker, R.; Bourg, L.; Santer, R.; Ramon, D. and Fischer, J. (2007). *MERIS in-flight spectral calibration*, *International Journal of Remote Sensing* 28 : 479-496.
- Deschamps, P.-Y.; Breon, F.-M.; Leroy, M.; Podaire, A.; Bricaud, A.; Buriez, J.-C. and Seze, G. (1994). *The POLDER mission: instrument characteristics and scientific objectives*, *IEEE Transactions on Geoscience and Remote Sensing* 32 : 598-615.
- Desmons, M. (2014). *Apport des mesures multiangulaires de POLDER/PARASOL dans la bande A de l'oxygène pour la caractérisation verticale des structures nuageuses*, Université Lille I.
- Desmons, M.; Ferlay, N.; Parol, F.; Mcharek, L. and Vanbauce, C. (2013). *Improved information about the vertical location and extent of monolayer clouds from POLDER3 measurements in the oxygen A-band*, *Atmospheric Measurement Techniques* 6 : 2221-2238.

- Doppler, L.; Preusker, R.; Bennartz, R. and Fischer, J. (2014).** *k-bin and k-IR: k-distribution methods without correlation approximation for non-fixed instrument response function and extension to the thermal infrared* Applications to satellite remote sensing, *jqsr* 133 : 382-395.
- Dubuisson, P.; Borde, R.; Schmechtig, C. and Santer, R. (2001).** *Surface pressure estimates from satellite data in the oxygen A-band: Applications to the MOS sensor over land*, *jgr* 106 : 27277.
- Dubuisson, P.; Buriez, J. C. and Fouquart, Y. (1996).** *High spectral resolution solar radiative transfer in absorbing and scattering media: application to the satellite simulation.*, *jqsr* 55 : 103-126.
- Dubuisson, P.; Dessailly, D.; Vesperini, M. and Frouin, R. (2004).** *Water vapor retrieval over ocean using near-infrared radiometry*, *Journal of Geophysical Research (Atmospheres)* 109 : 19106.
- Dubuisson, P.; Frouin, R.; Dessailly, D.; Duforêt, L.; Léon, J.-F.; Voss, K. and Antoine, D. (2009).** *Estimating the altitude of aerosol plumes over the ocean from reflectance ratio measurements in the O₂ A-band*, *Remote Sensing of Environment* 113 : 1899 - 1911.
- Dubuisson, P.; Giraud, V.; Chomette, O.; Chepfer, H. and Pelon, J. (2005).** *Fast radiative transfer modeling for infrared imaging radiometry*, *jqsr* 95 : 201-220.
- Emde, C.; Büll, R.; Buras, R.; Faure, F.; Hamann, U.; Kylling, A.; Mayer, B. and Meerkötter, R. (2008).** *Towards a Generic Radiative Transfer Model for the Earth's Surface-Atmosphere System (ESAS-Light) : WP1100 - Literature survey Radiative transfer tools*, .
- EUMETSAT (2011).** *MTG-FCI: ATBD for Optimal Cloud Analysis Product*, .
- EUMETSAT (2013).** *EPS-SG System Requirements Document*, .
- Fell, F. and Fischer, J. (2001).** *Numerical simulation of the light field in the atmosphere-ocean system using the matrix-operator method*, *jqsr* 69 : 351-388.
- Ferlay, N.; Thieuleux, F.; Cornet, C.; Davis, A. B.; Dubuisson, P.; Ducos, F.; Parol, F.; Riédi, J. and Vanbauce, C. (2010).** *Toward New Inferences about Cloud Structures from Multidirectional Measurements in the Oxygen A Band: Middle-of-Cloud Pressure and Cloud Geometrical Thickness from POLDER-3/PARASOL*, *Journal of Applied Meteorology and Climatology* 49 : 2492-2507.
- Fischer; Preusker and Rathke (2003).** *Cloud Top Pressure from Geo-stationary Satellite Observations in the Oxygen A-Band*, .
- Fischer, J.; Cordes, W.; Schmitz-Peiffer, A.; Renger, W. and Mörl, P. (1991).** *Detection of Cloud-Top Height from Backscattered Radiances within the Oxygen A Band. Part 2: Measurements.*, *Journal of Applied Meteorology* 30 : 1260-1267.
- Fischer, J. and Grassl, H. (1984).** *Radiative transfer in an atmosphere-ocean system: an azimuthally dependent matrix-operator approach*, *ao* 23 : 1032-1039.
- Fischer, J. and Grassl, H. (1991).** *Detection of Cloud-Top Height from Backscattered Radiances within the Oxygen A Band. Part 1: Theoretical Study.*, *Journal of Applied Meteorology* 30 : 1245-1259.
- Hanel, R. A. (1961).** *Determination of Cloud Altitude from a Satellite*, *jgr* 66 : 1300-1300.
- Hansen, J. E. and Travis, L. D. (1974).** *Light scattering in planetary atmospheres*, *Space Science Reviews* 16 : 527-610.
- Heidinger, A. K. and Pavolonis, M. J. (2009).** *Gazing at Cirrus Clouds for 25 Years through a Split Window. Part I: Methodology*, *Journal of Applied Meteorology and Climatology* 48 : 1100.
- Hess, M.; Koepke, P. and Schult, I. (1998).** *Optical Properties of Aerosols and Clouds: The Software Package OPAC.*, *Bulletin of the American Meteorological Society* 79 : 831-844.
- Hollstein, A. and Fischer, J. (2012).** *Radiative transfer solutions for coupled atmosphere ocean systems using the matrix operator technique*, *Journal of Quantitative Spectroscopy and Radiative Transfer* 113 : 536

- 548.

Hu, Y. X.; Wielicki, B.; Lin, B.; Gibson, G.; Tsay, S. C.; Stamnes, K. and Wong, T. (2000). *delta-fit: a fast and accurate treatment of particle scattering phase functions with weighted singular-value decomposition least squares fitting*, *jqsr* 65 : 681-690.

Kato, S.; Ackerman, T. P.; Mather, J. H. and Clothiaux, E. E. (1999). *The k-distribution method and correlated-k approximation for a shortwave radiative transfer model.*, *jqsr* 62 : 109-121.

Key, J. R. and Schweiger, A. J. (1998). *Tools for atmospheric radiative transfer: Streamer and FluxNet*, *Computers & Geosciences* 24 : 443 - 451.

King, M. D.; Platnick, S.; Menzel, W. P.; Ackerman, S. A. and Hubanks, P. A. (2013). *Spatial and Temporal Distribution of Clouds Observed by MODIS Onboard the Terra and Aqua Satellites*, *IEEE Transactions on Geoscience and Remote Sensing* 51 : 3826-3852.

Knibbe, W. J. J.; de Haan, J. F.; Hovenier, J. W.; Stam, D. M.; Koelemeijer, R. B. and Stamnes, P. (2000). *Deriving terrestrial cloud top pressure from photopolarimetry of reflected light*, *Journal of Quantitative Spectroscopy and Radiative Transfer* 64 : 173 - 199.

Kokhanovsky, A. A. and Breon, F.-M. (2012). *Validation of an Analytical Snow BRDF Model Using PARASOL Multi-Angular and Multispectral Observations*, *IEEE Geoscience and Remote Sensing Letters* 9 : 928-932.

Kokhanovsky, A. A.; Budak, V. P.; Cornet, C.; Duan, M.; Emde, C.; Katsev, I. L.; Klyukov, D. A.; Korkin, S. V.; C-Labonnote, L. and Mayer, B. (2010). *Benchmark results in vector atmospheric radiative transfer*, *Journal of Quantitative Spectroscopy and Radiative Transfer* 111 : 1931-1946.

Kokhanovsky, A. A.; Rozanov, V. V.; Nauss, T.; Reudenbach, C.; Daniel, J. S.; Miller, H. L. and Burrows, J. P. (2006a). *The semianalytical cloud retrieval algorithm for SCIAMACHY I. The validation*, *Atmospheric Chemistry & Physics* 6 : 1905-1911.

Kokhanovsky, A. A.; von Hoyningen-Huene, W.; Rozanov, V. V.; Noël, S.; Gerilowski, K.; Bovensmann, H.; Bramstedt, K.; Buchwitz, M. and Burrows, J. P. (2006b). *The semianalytical cloud retrieval algorithm for SCIAMACHY II. The application to MERIS and SCIAMACHY data*, *Atmospheric Chemistry & Physics* 6 : 4129-4136.

Kotchenova, S. Y. and Vermote, E. F. (2007). *Validation of a vector version of the 6S radiative transfer code for atmospheric correction of satellite data. Part II. Homogeneous Lambertian and anisotropic surfaces*, *ao* 46 : 4455-4464.

Kotchenova, S. Y.; Vermote, E. F.; Matarrese, R. and Klemm Jr., F. J. (2006). *Validation of a vector version of the 6S radiative transfer code for atmospheric correction of satellite data. Part I: Path radiance*, *ao* 45 : 6762-6774.

Kuze, A. and Chance, K. V. (1994). *Analysis of cloud top height and cloud coverage from satellites using the O₂ A and B bands*, *jgr* 99 : 14481.

Lacis, A. A. and Oinas, V. (1991). *A description of the correlated-k distribution method for modelling nongray gaseous absorption, thermal emission, and multiple scattering in vertically inhomogeneous atmospheres*, *jgr* 96 : 9027-9064.

Lenoble, J.; Herman, M.; Deuzé, J. L.; Lafrance, B.; Santer, R. and Tanré, D. (2007). *A successive order of scattering code for solving the vector equation of transfer in the earth's atmosphere with aerosols*, *jqsr* 107 : 479-507.

Lichtenberg (2015). *SCIAMACHY Offline Processor Level1b-2 ATBD*, .

Lindstrot, R. (2009). *Exploitation of the MERIS oxygen A band channel for the retrieval of cloud-top pressure and the correction of instrumental stray light*, Freien Universität Berlin.

- Lindstrot, R.; Preusker, R. and Fischer, J. (2010).** *Empirical Correction of Stray Light within the MERIS Oxygen A-Band Channel*, Journal of Atmospheric and Oceanic Technology 27 : 1185-1194.
- Lindstrot, R.; Preusker, R.; Ruhtz, T.; Heese, B.; Wiegner, M.; Lindemann, C. and Fischer, J. (2006).** *Validation of MERIS Cloud-Top Pressure Using Airborne Lidar Measurements*, Journal of Applied Meteorology and Climatology 45 : 1612.
- Maignan, F.; Breon, F.-M.; Fedele, E. and Bouvier, M. (2009).** *Polarized reflectances of natural surfaces: Spaceborne measurements and analytical modeling*, Remote Sensing of Environment 113 : 2642 - 2650.
- Maignan, F.; Bréon, F.-M. and Lacaze, R. (2004).** *Bidirectional reflectance of Earth targets: Evaluation of analytical models using a large set of spaceborne measurements with emphasis on the Hot Spot*, Remote Sensing of Environment 90 : 210-220.
- Mayer, B. and Kylling, A. (2005).** *Technical note: The libRadtran software package for radiative transfer calculations - description and examples of use*, Atmospheric Chemistry and Physics 5 : 1855-1877.
- McClatchey, R. A.; Fenn, R. W.; Selby, J. E. A.; Volz, F. E. and Garing, J. S. (1972).** *Optical properties of the atmosphere*, .
- McCleese, D. J. and Wilson, L. S. (1976).** *Cloud top heights from temperature sounding instruments*, Quarterly Journal of the Royal Meteorological Society 102 : 781-790.
- Menzel, W. P.; Frey, R. A.; Zhang, H.; Wylie, D. P.; Moeller, C. C.; Holz, R. E.; Maddux, B.; Baum, B. A.; Strabala, K. I. and Gumley, L. E. (2008).** *MODIS Global Cloud-Top Pressure and Amount Estimation: Algorithm Description and Results*, Journal of Applied Meteorology and Climatology 47 : 1175.
- Miller, S. D.; Forsythe, J. M.; Partain, P. T.; Haynes, J. M.; Bankert, R. L.; Sengupta, M.; Mitrescu, C.; Hawkins, J. D. and Vonder Haar, T. H. (2014).** *Estimating Three-Dimensional Cloud Structure via Statistically Blended Satellite Observations*, Journal of Applied Meteorology and Climatology 53 : 437-455.
- Minnis, P.; Garber, D. P.; Young, D. F.; Arduini, R. F. and Takano, Y. (1998).** *Parameterizations of Reflectance and Effective Emittance for Satellite Remote Sensing of Cloud Properties.*, Journal of Atmospheric Sciences 55 : 3313-3339.
- Mishchenko, M. I. and Travis, L. D. (1997).** *Satellite retrieval of aerosol properties over the ocean using polarization as well as intensity of reflected sunlight*, jgr 102 : 16989-17014.
- Mitchell, R. M. and O'Brien, D. M. (1987).** *Error Estimates for Passive Satellite Measurement of Surface Pressure Using Absorption in the A Band of Oxygen.*, Journal of Atmospheric Sciences 44 : 1981-1990.
- Moroney, C.; Davies, R. and Muller, J.-P. (2002).** *Operational retrieval of cloud-top heights using MISR data*, Geoscience and Remote Sensing, IEEE Transactions on 40 : 1532-1540.
- Nakajima, T. and Tanaka, M. (1988).** *Algorithms for radiative intensity calculations in moderately thick atmospheres using a truncation approximation*, jqsrt 40 : 51-69.
- O'Brien, D. M. and Mitchell, R. M. (1992).** *Error Estimates for Retrieval of Cloud-Top Pressure Using Absorption in the A Band of Oxygen.*, Journal of Applied Meteorology 31 : 1179-1192.
- Potter, J. F. (1970).** *The Delta Function Approximation in Radiative Transfer Theory.*, Journal of Atmospheric Sciences 27 : 943-949.
- Preusker; Lindstrot and Fischer (2010).** *MERIS Cloud-Top Pressure ATBD 2.3*, .
- Preusker, R.; Fischer, J.; Albert, P.; Bennartz, R. and Schüller, L. (2007).** *Cloud-top pressure retrieval using the oxygen A-band in the IRS-3 MOS instrument*, International Journal of Remote Sensing 28 : 1957-1967.
- Preusker, R. and Lindstrot, R. (2009).** *Remote Sensing of Cloud-Top Pressure Using Moderately Resolved Measurements within the Oxygen A BandmdashA Sensitivity Study*, Journal of Applied Meteorology and

Climatology 48 : 1562.

Rahman, H.; Pinty, B. and Verstraete, M. M. (1993). *Coupled surface-atmosphere reflectance (CSAR) model: 2. Semiempirical surface model usable with NOAA advanced very high resolution radiometer data*, Journal of Geophysical Research: Atmospheres 98 : 20791-20801.

Ramon, D.; Santer, R. and Dubuisson, P. (2002). *MERIS SURFACE PRESSURE AND CLOUD FLAG: PRESENT STATUS AND IMPROVEMENTS*, .

Rast, M.; Bezy, J. L. and Bruzzi, S. (1999). *The ESA Medium Resolution Imaging Spectrometer MERIS a review of the instrument and its mission*, International Journal of Remote Sensing 20 : 1681-1702.

Rodgers, C., 2000. *Inverse methods for atmospheric sounding: Theory and practice*. World Scientific, .

Rothman, L. S.; Gordon, I. E.; Barbe, A.; Benner, D. C.; Bernath, P. F.; Birk, M.; Boudon, V.; Brown, L. R.; Campargue, A.; Champion, J.-P.; Chance, K.; Coudert, L. H.; Dana, V.; Devi, V. M.; Fally, S.; Flaud, J.-M.; Gamache, R. R.; Goldman, A.; Jacquemart, D.; Kleiner, I.; Lacome, N.; Lafferty, W. J.; Mandin, J.-Y.; Massie, S. T.; Mikhailenko, S. N.; Miller, C. E.; Moazzen-Ahmadi, N.; Naumenko, O. V.; Nikitin, A. V.; Orphal, J.; Perevalov, V. I.; Perrin, A.; Predoi-Cross, A.; Rinsland, C. P.; Rotger, M.; Simevcková, M.; Smith, M. A. H.; Sung, K.; Tashkun, S. A.; Tennyson, J.; Toth, R. A.; Vandaele, A. C. and Vander Auwera, J. (2009). *The HITRAN 2008 molecular spectroscopic database*, jqsrt 110 : 533-572.

Rothman, L. S.; Jacquemart, D.; Barbe, A.; Chris Benner, D.; Birk, M.; Brown, L. R.; Carleer, M. R.; Chackerian, C.; Chance, K.; Coudert, L. H.; Dana, V.; Devi, V. M.; Flaud, J.-M.; Gamache, R. R.; Goldman, A.; Hartmann, J.-M.; Jucks, K. W.; Maki, A. G.; Mandin, J.-Y.; Massie, S. T.; Orphal, J.; Perrin, A.; Rinsland, C. P.; Smith, M. A. H.; Tennyson, J.; Tolchenov, R. N.; Toth, R. A.; Vander Auwera, J.; Varanasi, P. and Wagner, G. (2005). *The HITRAN 2004 molecular spectroscopic database*, jqsrt 96 : 139-204.

Rozanov, A.; Rozanov, V.; Buchwitz, M.; Kokhanovsky, A. and Burrows, J. P. (2005). *SCIATRAN 2.0 A new radiative transfer model for geophysical applications in the 175 2400 nm spectral region*, Advances in Space Research 36 : 1015-1019.

Saiedy, F.; Hilleaery, D. T. and Morgan, W. A. (1965). *Cloud-top altitude measurements from satellites*, ao 4 : 495.

Spurr, R. J. D. (2006). *VLIDORT: A linearized pseudo-spherical vector discrete ordinate radiative transfer code for forward model and retrieval studies in multilayer multiple scattering media*, jqsrt 102 : 316-342.

Stamnes, K.; Tsay, S. C.; Jayaweera, K. and Wiscombe, W. (1988). *Numerically stable algorithm for discrete-ordinate-method radiative transfer in multiple scattering and emitting layered media*, Appl. Opt. 27 : 2502-2509.

van de Hulst, H. C., 1980. *Multiple light scattering. Tables, formulas and applications*. , .

Vanbauce, C.; Buriez, J. C.; Parol, F.; Bonnel, B.; Sèze, G. and Couvert, P. (1998). *Apparent pressure derived from ADEOS-POLDER observations in the oxygen A-band over ocean*, grl 25 : 3159-3162.

Vanbauce, C.; Cadet, B. and Marchand, R. T. (2003). *Comparison of POLDER apparent and corrected oxygen pressure to ARM/MMCR cloud boundary pressures*, grl 30 : 1212.

Vermote, E.; Tanre, D.; Deuze, J.; Herman, M. and Morcette, J.-J. (1997). *Second Simulation of the Satellite Signal in the Solar Spectrum, 6S: an overview*, Geoscience and Remote Sensing, IEEE Transactions on 35 : 675-686.

Walther, A. and Heidinger, A. K. (2012). *Implementation of the Daytime Cloud Optical and Microphysical Properties Algorithm (DCOMP) in PATMOS-x*, Journal of Applied Meteorology and Climatology 51 : 1371-1390.

- Wang, P.; Stammes, P.; van der A, R.; Pinardi, G. and van Roozendaal, M. (2008).** *FRESCO+: an improved O₂ A-band cloud retrieval algorithm for tropospheric trace gas retrievals*, Atmospheric Chemistry & Physics 8 : 6565-6576.
- Wielicki, B. A. and Coakley Jr., J. A. (1981).** *Cloud Retrieval Using Infrared Sounder Data: Error Analysis.*, Journal of Applied Meteorology 20 : 157-169.
- Winker, D. M.; Hunt, W. H. and McGill, M. J. (2007).** *Initial performance assessment of CALIOP*, Geophysical Research Letters 34 : n/a-n/a.
- Wiscombe, W. J. (1977).** *The Delta-M Method: Rapid Yet Accurate Radiative Flux Calculations for Strongly Asymmetric Phase Functions.*, Journal of Atmospheric Sciences 34 : 1408-1422.
- Wu, M.-L. C. (1985).** *Remote Sensing of Cloud-Top Pressure Using Reflected Solar Radiation in the Oxygen A-Band.*, Journal of Applied Meteorology 24 : 539-546.
- Yamamoto, G. and Wark, D. Q. (1961).** *Discussion of the Letter by R. A. Hanel, 'Determination of Cloud Altitude from a Satellite'*, jgr 66 : 3596-3596.
- Young, A. T. (1980).** *Revised depolarization corrections for atmospheric extinction*, ao 19 : 3427.
- Zeng, S.; Cornet, C.; Parol, F.; Riedi, J. and Thieuleux, F. (2012).** *A better understanding of cloud optical thickness derived from the passive sensors MODIS/AQUA and POLDER/PARASOL in the A-Train constellation*, Atmospheric Chemistry & Physics 12 : 11245-11259.